

For New Technology Network

NTN®

TECHNICAL REVIEW

No.

81

Special Issue;
**Automotive Products and
Technologies**

November 2013



NTN to verify practicality of in-wheel motor driven vehicles through the demonstration project of microcompact mobility commuter EVs

For New Technology Network

NTN has started a demonstration project aiming for early expansion of electric vehicles that adopt an in-wheel motor system, by creating prototype in-wheel motor driven microcompact mobility commuters.*

In Ise-City, Mie Prefecture, NTN is participating in the "Ise Municipal Council for the Creation of a Low-Carbon Society Using Electric Vehicles, Etc." and our EVs will be used as official cars of Ise-City, as well as business vehicles for the Council members such as Ise Chamber of Commerce and Industry, Ise City Tourist Association, etc. They are also used in the tourism business partnering with the council members to verify their usefulness and impact on the environment.

In addition, NTN participated in the "EV Festa" which took place at Mount Fuji, which was recently listed as a World Heritage site, as well as proceeded with the demonstration project on the public roads partnering with Iwata-City, Shizuoka Prefecture. Overseas, NTN is partnering with Annecy, France to conduct demonstration projects by creating vehicles that comply with the European microcompact mobility vehicle standards together with the small to medium companies in the region.

Through these projects, NTN aims to expand the use of environmentally-friendly electric vehicles and verifying performance of in-wheel motor driven vehicles characterized by their high degree of freedom for the space design and their use in real life.

*One- or two-passenger vehicles, with smaller scale and higher maneuverability than the "light cars," for neighborhood commuting with high environmental performance



▲ Ceremony of lending vehicles at Ise-City (September 30, 2013)
(Center: Ise-City Mayor Suzuki
Right: Council Chairman Paku
Left: NTN Chairman Suzuki)



▲ Mt. Fuji EV Festa (August 1, 2013)
(Right: Shizuoka Prefecture Governor Kawakatsu
Left: Association for the Promotion of Electric Vehicles, Chief Commissioner Tajima)



At the opening event of
Annecy International Animated Film Festival
(June 10, 2013)





TECHNICAL REVIEW

No.81

Special Issue:

Automotive Products and Technologies

NTN TECHNICAL REVIEW No.81

CONTENTS

Preface	Yukiyoshi HAGIMOTO	1
Contribution	Trends of Intelligent Vehicle Dynamics Controls and Their Future Masato ABE Professor, Department of Vehicle System Engineering, Kanagawa Institute of Technology	2
Perspective	NTN Module Technology Contributes to Energy Efficiency and CO₂ Reduction in Automobiles Takehiko UMEMOTO	12
● Special Issue for EV/HEV Products		
	Recent Technology Trends of In-Wheel Motor System for Automotive Tomoaki MAKINO, Aiko ISHIKAWA, Chinami ITOU and Kayo SAKAI	22
	Electro-mechanical Brake Unit with Parking Brake Tatsuya YAMASAKI, Makoto MURAMATSU and Yui MASUDA	30
	Ball Screw Drive Module for Electric Hydraulic Brake Hayato KAWAGUCHI and Keisuke KAZUNO	36
	Low Torque Deep Groove Ball Bearings for EV and HEV Tsuyoshi KODA, Takahiro WAKUDA and Tomohisa UOZUMI	40
	The Reactor Core for HEV Boost Converter Takayuki ODA, Shinji MIYAZAKI and Eiichirou SHIMAZU	46
● Special Issue for Advanced Function and Fuel-efficient Products		
	Hub Bearing with an Integrated High-Resolution Rotation Sensor Kentaro NISHIKAWA, Toru TAKAHASHI and Christophe DURET	52
	Press Connect Spline Hub Joint Takayuki NORIMATSU and Tsutomu NAGATA	58
	Next-generation High Efficiency Fixed Type Constant Velocity Joint "CFJ" Teruaki FUJIO	64
	Development of Low Torque Seal Ring for Automotive Transmission Kouzou KAKEHI, Takumi KONDOU, Takuya ISHII and Masato YOSHINO	68
	The Introduction of Sintered New Products for Automobile Tomonori YAMASHITA, Tomokazu SONOZAKI	74
● Technical Papers		
	Rolling Contact Fatigue Life of Highly-carbonitrided JIS-SUJ2 Daisuke SATO and Chikara OHKI	78
	Effect of Naturally Derived Antioxidants as Surface Treatment Yosuke TAGUCHI, Eriko ITAHASHI and Hidenobu MIKAMI	85
	Grease Leakage Prevention for Double-Row Angular Ball Bearings Mitsuo KAWAMURA, Norihide SATO, Tomoya SAKAGUCHI and Mariko IZUMI	92
	A Creep Mechanism of Rolling Bearings Tsuyoshi NIWA	100
● Our Line of Award Winning Products		
	The Japanese Society of Tribologists "2012 Technology Award" Prevention of Grease Leakage from Ball Bearings Due to Cage Shape Improvement Norihide SATO, Mitsuo KAWAMURA and Tomoya SAKAGUCHI	104
	European Mechatronics Meeting (EMM) 2012 "Grand Prix of Mechatronics Award" Intelligent In-wheel Motor System Herve LENON, Eiichi ASANO, Tomomi GOTOU, and Kaori TOMODA	105
	Automechanika 2012 "Innovation Award" In-wheel Motor System Herve LENON and Eiichi ASANO,	106
	The Japan Society of Precision Engineering of the 2013 Spring Semestrial Meeting "Best Presentation Award" Parallel Link High Speed Angle Control Equipment Hiroshi ISOBE, Yukihiro NISHIO, Keisuke SONE, Hiroyuki YAMADA and Yoshio FUJIKAWA	107
Our Line of New Products ————— 108		

*A message for the special issue on
automotive products and technologies*



Yuki Yoshi Hagimoto
Managing Executive Officer

As the motorization in developing countries is fully in progress, the automobile industry is facing the critical challenge of low-fuel consumption requirements for reduction of greenhouse gas emission and the use of fossil fuels such as oil. Therefore, an aggressive development of engines for lower fuel consumption, hybrid vehicles and electric vehicles is underway. Also, development of fuel cell vehicles is becoming active with the target of commercial introduction in 2015.

In view of these circumstances, **NTN** reorganized our engineering functions within the Automotive Business HQ to accelerate the development of unit and module products to support energy conservation of automobiles, and established a new EV Module Business HQ in April, 2013 to promote development of parts, modules and systems related to the driving, steering and controlling of electric vehicles.

We have worked to publish this issue of the **NTN** Technical Review No. 81 featuring the state-of-art automotive products and technologies in time with many exhibits of new products from **NTN** at the 43rd Tokyo Motor Show 2013, which was held during the period from November 22 to December 1, 2013 with the theme of "Compete! And shape a new future." In this Technical Review, we were able to publish a contribution "Trends of Intelligent Vehicle Dynamics Controls and Their Future" from Professor Masato Abe of Department of Vehicle System Engineering, Kanagawa Institute of Technology, who is an expert in vehicle dynamics control. In the "Special Issue for EV/HEV Products," we introduce **NTN's** driving module, control system, etc. which lead to automatic driving including an in-wheel motor system for electric vehicles. In the "Special Issue for Advanced Function and Fuel-efficient Products," we introduce hub bearings and constant velocity joints which **NTN** has been globally distributing and new products contributing to higher functionality and lower-fuel economy, as well as composite material products consisting of mainly resin and sintered material.

At **NTN**, we will celebrate our 100th anniversary in fiscal 2017. Following our theme, "For New Technology Network: We shall contribute to international society through creating new technologies and developing new products," we are striving to contribute to sustainable development of the society by further developing environmentally-friendly products.

For New Technology Network

Trends of Intelligent Vehicle Dynamics Controls and Their Future



Masato ABE

Doctor of Engineering, Professor, Department of Vehicle System Engineering, Kanagawa Institute of Technology

Following to a survey of recent trends of active motion control of the vehicles, a possibility of the vehicle active motion control of electric powered vehicles is discussed and the experimental substantiation of the possibility by using the experimental vehicle is introduced. It is found that the vehicle motion controls which are not available for the ordinary vehicles so far will become available by an ultimate intelligent active motion control of electric powered vehicles. A vehicle limit performance is dramatically extended and the tire wear of the vehicle during controlled vehicle motion is significantly reduced by the controls.

1. Introduction

Along with the adoption of the electric motor as one of the pillars of the next-generation vehicles to cope with environmental concerns and energy issues, another significant technology area supporting next generation vehicles is the so-called intelligent/intellectual vehicles. Fig. 1 shows a representation of technology areas supporting next-generation vehicles in one of the views. In the broad "Environment and Transportation System," the next-generation vehicle can be defined as electric "power" mounted on the "structure" for "motion" and it seems like one of the key technologies in this picture is the "intelligence" for vehicles. The specific technology elements in this area include car electronics, information, communication, control, etc.

Intelligence for vehicles is the technology that should be related to almost all automotive technologies, however, especially in the active control area aiming at prevention and safety, it is not only an indispensable technology for motion control of individual vehicles but also for mutual motion control of several vehicles in the transportation space. Several active motion control technologies are already

equipped in commercial vehicles that are greatly improving their safety and mobility performance. It is expected that active motion control based on intelligent technology will increase among others, since the motion control which has been impractical before now becomes more realistic as electric powered vehicles expand.

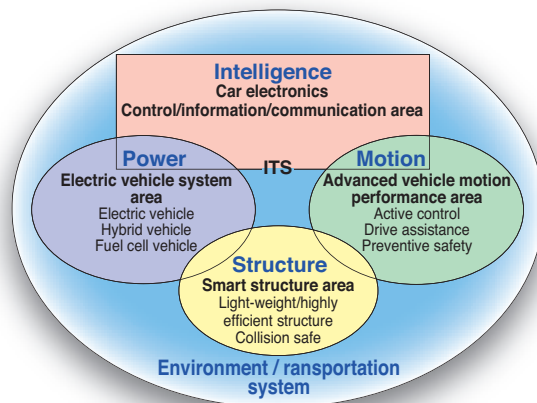


Fig.1 Technologies supporting a vehicle for new era

In this article, I will give an overview of the active motion control that has been proposed and incorporated so far within the horizontal plane which a driver is directly involved in the control and is largely related to the preventive safety from the view point of the motion dynamics property of controlled vehicles, as well as some specifics on the trends and possibilities of active motion controls in a new era of increased use of electric power in vehicles. I will also describe some results from our ongoing joint research with NTN.

2. Past active motion control technologies

2.1 Rear-wheel active steering

In the 1980s, a breakthrough technology of rear-wheel active steering control made its debut in the impasse of vehicle motion performance. It had some precedence before; however, this is a period when motion control by rear-wheel active steering was viewed as an improved motion control in a relatively high-speed range. Initially, rear-wheel steering relative to steering angle and force was proposed to improve motion property, for example, eliminating or reducing the side slip to the maximum extent. Then, more intelligent model-following control systems were proposed such as the feed-forward control in which the yaw motion of a vehicle follows the model response and addition of feedback control following the detection of the yaw rate. With these technological results in the background, commercial vehicles with rear-wheel active steering control were introduced in the market.

The rear-wheel steering control depends on the cornering force of the tires generated by the side-kick angle from steering. For example, the control law driven from the linear model with the two-degrees-of-freedom model is effective in the range where the side-slip angle is small exhibiting a linear tire property. However, in the non-linear range of lateral force of the tire, the aimed control ability is drastically reduced. In addition, since the lateral force of the tire is greatly affected by the load and longitudinal force the accuracy of motion control can be lost when the lateral acceleration is large and furthermore, the motion involving acceleration and deceleration can become a disturbance.

2.2 DYC

The technology that emerged next was the direct yaw-moment control (DYC). DYC is a global name for the motion control taking advantage of the moment produced by the longitudinal force on the individual tires. The longitudinal force for this technology can be

obtained from the distribution of driving force on the right and left sides, distribution of braking force or brake on only one side, etc. This type of motion control by yaw-moment may be seen as existing for a long time like the passive control by differential gears, however, it was only since the 1990s that many research and development activities for active motion control by actively producing yaw-moment were observed.

The lateral force generated by the side slip is greatly affected by the lateral motion, load, and longitudinal force of the vehicle to be controlled. In contrast, the longitudinal force is not fundamentally affected by the lateral motion of a vehicle. Some may argue that the longitudinal force should also be affected by the load and lateral force or lateral motion. However, the command of longitudinal force necessary for control is the braking torque applied by braking pressure and driving torque given to the tire rotating motion. The tire rotation motion itself is independent from the lateral motion of a vehicle and the tires follow the command torque providing rotation motion. The longitudinal slip produced by this motion generates the longitudinal force that balances with the command torque. Therefore, the longitudinal force is not directly affected by the lateral motion and can control the lateral motion with the required force. That is of course limited to the cases when there is sufficient tire load to produce a longitudinal force large enough for the corresponding command. This appears to be the technical characteristic at the base of the fact that the electric stability control (ESC), one type of DYC, is about to be standardized and required, in addition to the fact that deceleration is effective in order to stabilize the motion.

The vehicle motion on the horizontal plane against steering and external yaw moments can be expressed essentially by the two-variable motion equation of lateral slip and yaw. By looking at this equation, it is easily understood that when a driver steers the front wheels the active motion control that exhibits the same motion as that following the steering can be fundamentally achieved whether it is by the rear-wheel active steering or by DYC. Fig. 2 shows the comparison of the results from the rear-wheel active control and DYC when the yaw rate is controlled to be the response to the primary delay of steering¹⁾. This shows the motion in terms of side slip and yaw rate locus from one cycle of the sine wave steering input. From the graph we can compare the magnitude of the side slip produced during the sine wave yaw motion.

The graph shows the impact of disturbance of longitudinal acceleration and deceleration during the

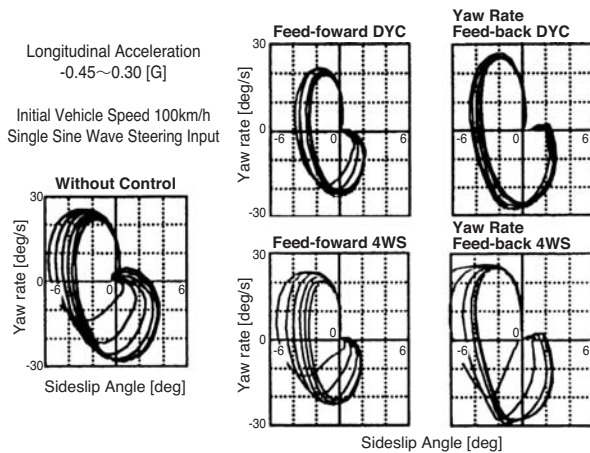


Fig.2 Effects of rear wheel active steer and DYC

motion indicating that the control by DYC is more robust against the disturbance with more stable motion even in the non-linear range of large side slip of tires. However, in case of rear-wheel active steering, it is revealed that an adverse effect was produced due to the limitation of the tire against lateral force, even with the yaw rate feedback trying to force it to follow the model response.

Therefore, DYC is more superior to the rear-wheel active steering in many respects. Although DYC is suitable for directly controlling yaw motion, it is not necessarily suitable for controlling the side slip angle and lateral acceleration since it does not directly produce lateral force ²⁾.

2.3 Front-wheel active control and steering control

A motion control with further active steering control over a driver's steering of the front wheels is also being proposed and realized. It appears to have the same problem as the rear-wheel active steering as it depends on the lateral force from the steering angle, however, the mechanism for realizing this method can be simpler than reaching out to the rear wheels for steering. In addition, it is possible to obtain theoretical advantages and disadvantages of the respective active control methods from the motion equation or transfer function of the side slip in the horizontal plane and the response of the yaw motion to the front-wheel or rear-wheel steering. The front-wheel active control eliminating the mechanical link between front wheels and steering wheel is a complete steer-by-wire (SBW) system. It appears that this system will be achieved in the near future. This system increases the degree of freedom for control and steering reaction force, among others, and can be set at any value.

On the other hand, most of the current power

steering is becoming electric power steering (EPS), making it easy to control the steering reaction force. It has been determined that 50% of the sensory evaluation of a driver regarding the steering response can be controlled by adjusting the steering reaction force without changing any vehicle motion performance. Thus, setting of the steering reaction force is important, even if it does not directly contribute to the active motion control; not to be ignored in the overall scheme of motion control of intelligent vehicles, and therefore, attracting much attention.

2.4 Other control

Active suspension, which is motion control of a vehicle with respect to comfort, is outside the scope of this article; however, the active stabilizer in that technology is used for controlling the lateral motion of a vehicle. This technology does not directly use the lateral force; however, it controls the load on the right and left tires which affect the lateral force and as a result controls the lateral motion.

Other important controls worth mentioning, although they do not directly control the motion of a vehicle itself, are ABS and TCS. They control components which control the functions of tires that support vehicle motion and as a result greatly contribute to the improvement of the vehicle motion performance.

2.5 Integrated control

Even with acceleration and deceleration, if the longitudinal speed is constant or given as a parameter that changes during its period, the vehicle motion in the horizontal plane against steering can be basically expressed with two-degrees of freedom of side slip and yaw. By using any two of the aforementioned controls, namely, front-wheel active steering, rear-wheel active steering or DYC, a vehicle that provides any side slip and yaw motion against steering can be realized theoretically. One idea of the integrated control is to obtain desirable motion properties by using two (or more) active controls simultaneously based on this perspective.

Each active control seems to have its own limitation if used individually, as mentioned before. The limitation perhaps comes from the non-linearity of tire properties, as some extreme load may be placed on tires during the control. When two or more controls are used, this can be offset by a synergy effect that compensates the limitations with each other. The integrated control can now be described as using two or more controls simultaneously and improving the vehicle motion properties and their limitations by using 4-tire forces reasonably ^{3), 4), 5)}.

Fig. 3 is a comparison of the effects of the rear-wheel active control, roll-moment distribution control (RDC) using a longitudinal stabilizer and their integrated control with side slip, and yaw rate locus against a sine wave steering input ⁶⁾. Rear-wheel active steering is a front-wheel steering angle proportional control to eliminate the steady side slip and RDC is a control for the stabilizer rigidity of the front and rear wheels maintaining the total roll rigidity so that side slip of front and rear wheels match the driver's intention. The motion is stable if a constant yaw motion is produced from a small side slip. With only the rear-wheel active steering, the motion is not stabilized when the burden on the rear wheels becomes large at high speeds and the side slip becomes larger than without control. In contrast, when it is used with RDC, the excessive transition of load between the left and right rear wheels is suppressed resulting in improvement of lateral force limitations realizing the motion aimed by the rear-wheel active steering up to the high speed range. This effect is larger than what can be obtained with RDC only.

There are already some examples of commercially available vehicles with integrated control. If the capabilities of four tires are more reasonably used, it appears that the vehicle motion properties and limitation performance can be further improved. From this standpoint, the integrated control is likely to remain as one of the most important key words in vehicle motion control.

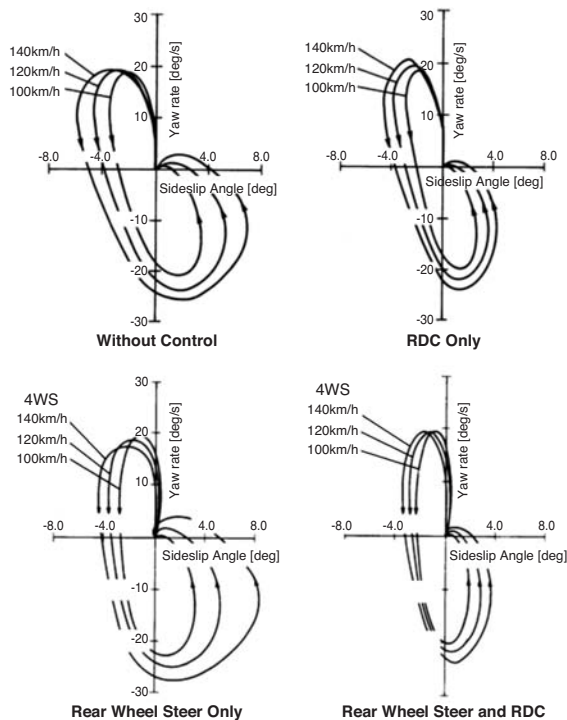


Fig.3 Integrated control of rear wheel active steer and RDC

3. Electric power and intelligent motion control

3.1 Eight-variable control

Recently, there has been an emergence of electric-powered vehicles. The first motivation for this trend, of course, is to improve environmental/energy concerns. However, if those electric-powered vehicles are equipped with four in-wheel motors, the longitudinal force of these four tires can be freely and independently determined. Also, since there will be no drive shaft, these four wheels can be easily steered independently and the lateral force can be also freely and independently determined. This means that eight forces that determine the motion of a vehicle can be independently determined. Of course, these vehicles are equipped with "full drive by wire." From the standpoint of the dynamics of a vehicle, this presents a tremendous possibility.

Although they can be freely and independently determined, in order for a vehicle to respond in a predetermined way to the steering in a plane certain lateral force and yaw moments need to be applied at each instance to the vehicle. These forces can be obtained reversely if the target response is given. In order to provide motion corresponding to the driver's acceleration or braking operation, longitudinal force is needed based on those commands. The grand sum of the lateral and longitudinal forces from those 8 forces and the sum of the yaw moments produced by those 8 forces need to be always maintained at varying values, determined by the target response of the vehicle at each instance. This constitutes three constrained conditions for 8 freely determinable variables.

On the other hand, since the forces can be determined in this manner, any motion can be basically achieved in response to the steering. When only desirable response of the side slip and yaw rate to the steering is determined, active motion control that delivers desirable targeted vehicle motion can be achieved.

3.2 Distribution control and norm

Since there are three constrained conditions to eight variables, the redundancy of degrees-of-freedom is still 5. Therefore, all eight variables cannot be determined without some norm for determining them, which is the norm for how to use these eight tire forces. Any norm will work; however, one that can be easily assumed is the norm (1) to use the tires so that the load on each tire is minimized as a whole. This way it is expected that the burden on each tire can be evenly distributed and the motion limit performance can be improved.

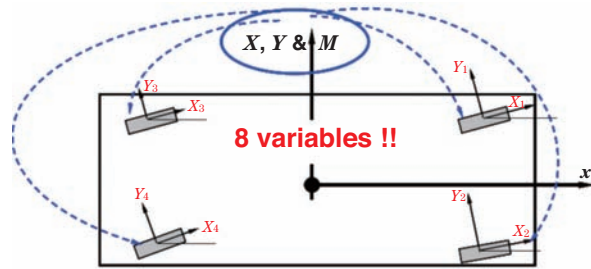
Another possible norm is (2) to control the motion using the tire force so that the energy dissipation due to the tire slip during motion is minimized on the whole. As a result, it is expected to realize even distribution of tire wear due to the tire slip and motion control with minimal energy dissipation due to the tire slip. This will minimize wear of tires.

If the evaluation function of the norm (1) is a square sum of the resultant force from all the tires in the horizontal plane divided by the tire load, it can be expressed by the quadratic form of the distributed longitudinal and lateral force of each tire. Similarly, if the evaluation function of the norm (2) is a square sum of the energy dissipation rate due to slippage of each tire, it can be expressed as the square sum of the distributed longitudinal and lateral force of each tire. However, each factor in these equations has to be estimated in real time from the slip force and slip velocity of each tire in motion using the tire model.

In either norm case (1) or (2), the evaluation function can be given with the quadratic form of the force applied to each tire with 8 variables; therefore, the condition to minimize this under the three constrained conditions is given with a linear algebraic function of $8-3=5$ variables which can be solved quite easily. In this way, these eight variables are finally determined and commands for driving or braking and steering can be issued to each tire so that each tire can produce these forces. This is the distribution control of eight forces. Fig. 4 is a graphical representation of this distribution.

Given above, three constrained conditions were minimally required and were applied against eight variables that realize the targeted motion. Since it still has 5-degrees of freedom of redundancy, there is room for additional constrained conditions to realize some desirable motion. It is well known that the longitudinal force working on tires can produce vertical force to a vehicle depending on the suspension setting. Therefore, a condition to produce rolling moment to suppress vehicle rolling from this vertical force can be set in the equation. If this is given as the fourth constrained condition, the previous condition to minimize the evaluation function given in quadratic form can be reduced to the linear equation of 4 variables which can be solved even more easily. As such, new constrained conditions can be added to determine the distribution of eight forces to realize a more desirable motion. By taking advantage of the redundancy of the variables, motion can be controlled by adding motion constrained conditions in the realistic range.

Sharing X, Y & M with eight variables of four wheels to minimize the cost function J



then, T_i and δ_i to steering input δ_h are determined.

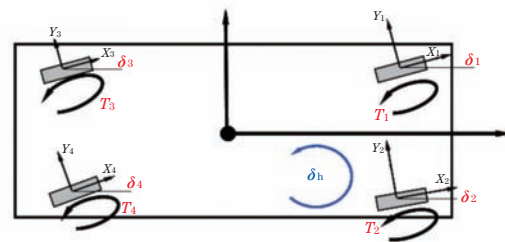


Fig.4 Concept of 8 tire force distribution

3. 3 Estimation of tire energy dissipation

When an appropriate tire model is used, not only the longitudinal and lateral forces on the tires can be estimated real-time and online but also slip force and slip velocity. The energy dissipation rate due to slippage can be estimated from the slip velocity and slip force and its integration gives the tire energy dissipation due to slippage.

For example, by using the brush tire model, which is often used as a physical model, longitudinal force and lateral force in the adhesion region and slip region of the contact area can be given by an analytical equation when longitudinal slip rate, lateral slip angle, traveling speed, and load are input. Similarly, longitudinal and lateral slip velocity can also be given. Therefore, a good estimate of tire forces can now be obtained if the parameters of that physical model are adjusted to the actual measurement.

This online estimation based on the model can be used for distribution control of the norm (2) and also for the evaluation of energy dissipation due to tire slip in motion.

3. 4 Ultimate intelligent motion control and its effect

Fig. 5 shows the block diagram of active motion control using the distribution of eight forces to each tire based on the aforementioned approach. Research and development of intelligent motion control taking advantage of the properties of electric vehicles by controlling these eight forces has been started in different parts of the world (7), (8), (9). It appears that the active motion control of electric vehicles by "full drive by wire" will lead to the ultimate integrated active motion controlled intelligent vehicles.

We also verified that this is realizable by using an actual vehicle in the joint research conducted with NTN, to demonstrate that this is not merely a desk plan (10), (11), (12). Fig. 6 shows the experimental vehicle for this demonstration with an in-wheel motor equipped at each of four wheels and steering system to independently control all four wheels. In addition, a micro-auto box in which the intelligent active motion control system depicted in Fig. 5 is installed is mounted along with the vehicle motion measurement system in the vehicle.

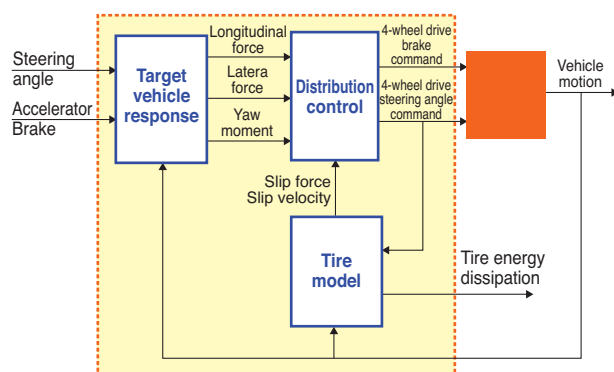


Fig.5 Tire force distribution control



Fig.6 Experimental vehicle

(1) Effect of distribution control minimizing tire workload

As mentioned earlier, any response to the steering is basically possible in this vehicle motion control; however, in order to compare the effect of the control with the regular vehicle without control, the response to be realized is set to regular vehicle response which can be obtained from a two-degrees of freedom model of lateral slip and yaw on a plane. A braking lane change experiment of -0.4G of longitudinal acceleration was conducted on the course shown in Fig. 7 in order to confirm the effect of distribution control of the norm (1) mentioned above under this setting.

The result is shown in Fig. 8. When no control is applied, particularly in the latter half of the lane change when counter steering is made, the motion became unstable, possibly because the workload on a certain rear tire was extremely large exceeding the limit. In contrast, when control is applied, the motion was stable in all the cases of lane changes possibly due to the load to the tires in motion was evenly distributed without any specific tire bearing extreme burden.

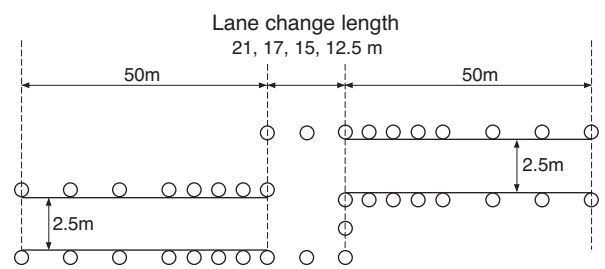


Fig.7 Lane change course

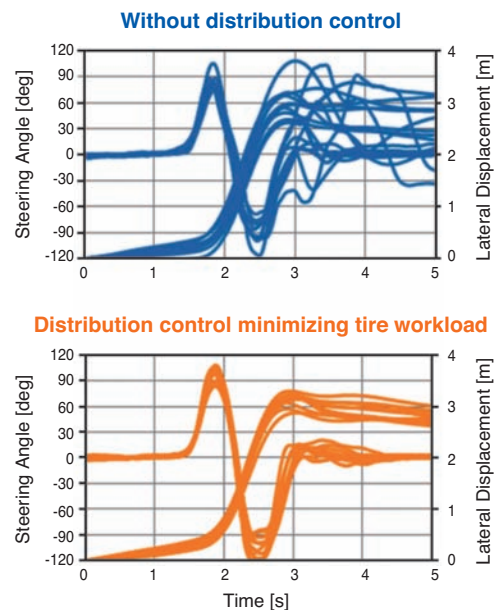


Fig.8 Effects of distribution control minimizing tire workload

The effect of control for even distribution of tire load is significant. Attempting to control the vehicle rolling by applying lateral and longitudinal forces in the reverse direction and of the same magnitude, the motion may become unstable due to imbalance of tire loads even if the rolling may be controlled. The norm of distribution control for load equalization should become effective, particularly in this case.

To confirm this assumption, a braking lane change simulation of -0.4G from 120 km/h in a small passenger car with a man-vehicle system was made using an appropriate driver model. The result is shown in Fig. 9. As anticipated, stable vehicle motion with small rolling was obtained only with "load equalization distribution control + rolling control" where constrained condition of rolling control was added. I am also willing to verify this with a real vehicle.

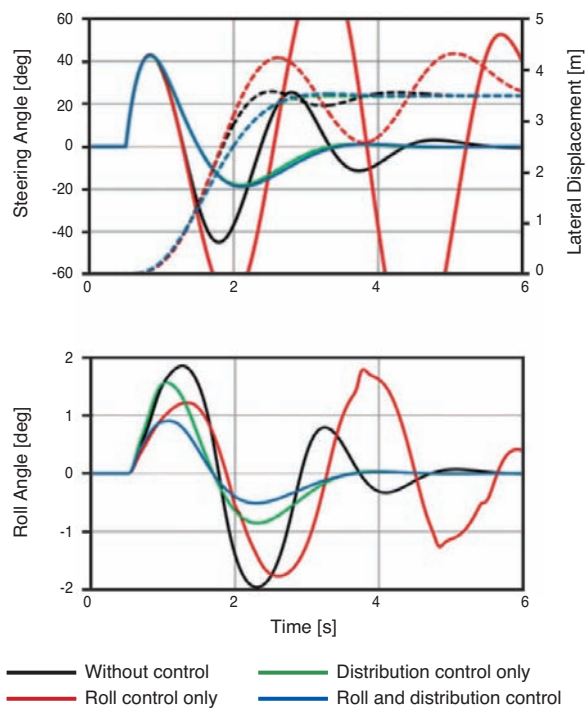


Fig.9 Combined effects of both distribution and roll controls

(2) Effects of distribution control minimizing tire energy dissipation due to slippage

Using the same course, experiments of lane changes were conducted including the distribution control vehicle for the above norm (2) to examine the impact of these distribution controls on the energy dissipation due to tire slip during the motion.

Fig. 10 shows the vehicle motion when a lane change with peak lateral acceleration of around 0.4G is made at the constant speed of 60 km/h. From the graph it is apparent that the motion is almost the same with or without control. Fig. 11 shows how the energy dissipation due to each tire slip and total energy dissipation of all the tires change depending on the type of control from the start of lane change to the end. In addition, Fig. 12 shows the motion of the vehicle when a steep lane change with peak lateral acceleration of 0.6G is applied and Fig. 13 shows the tire energy dissipation during that time.

When the peak lateral acceleration with the lane change increases from 0.4G to 0.6G, the energy dissipation due to tire slip drastically increases; however, the norm (2), which is the distribution control minimizing the square sum of energy dissipation due to tire slip in real time, is most effective for reducing the energy dissipation due to slip in all cases. With this control, among others, the energy dissipation at each tire is equalized showing similar energy dissipation at all the tires. It is expected that the tire wear due to motion will be equalized with four wheels by this control.

Although the tire load equalization control was initially considered to be also effective for energy dissipation, the result was adverse; showing larger total tire energy dissipation due to slippage even when compared to the case without control. Since the workload ratio on each tire is equalized, the distribution control produces a large force in the horizontal plane at the tire with heavy load resulting in large energy dissipation due to tire slip by that large force which contributes to large total energy dissipation even compared with the case without control. Even if this control contributes to stabilizing the motion, it should promote imbalance of tire wear. A control that distributes the tire force in real time and estimates the energy dissipation of each tire at each instance due to slip based on a tire model is required in order to realize motion that minimizes tire energy dissipation and tire wear.

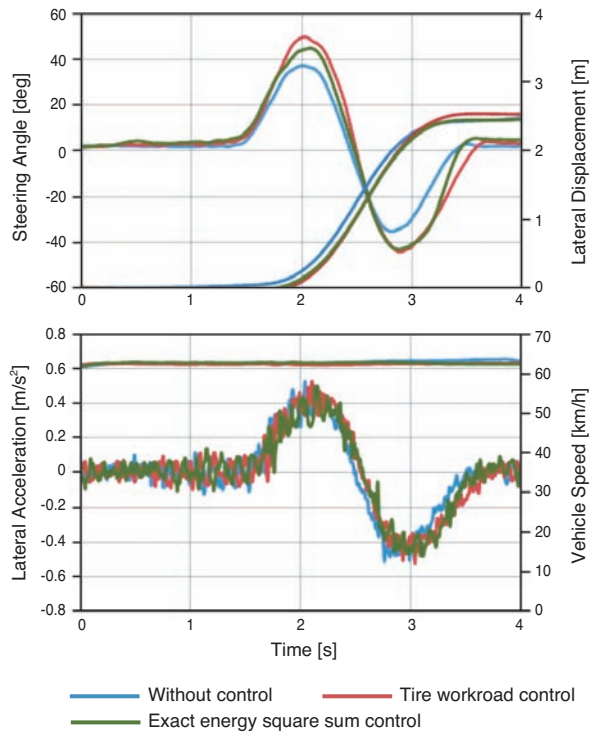


Fig.10 Lane change with peak lateral acceleration 0.4G

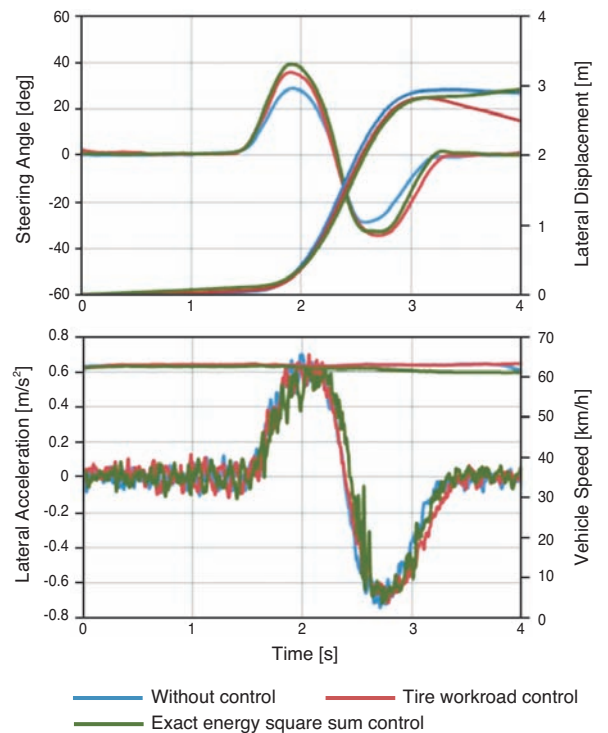


Fig.12 Lane change with peak lateral acceleration 0.6G

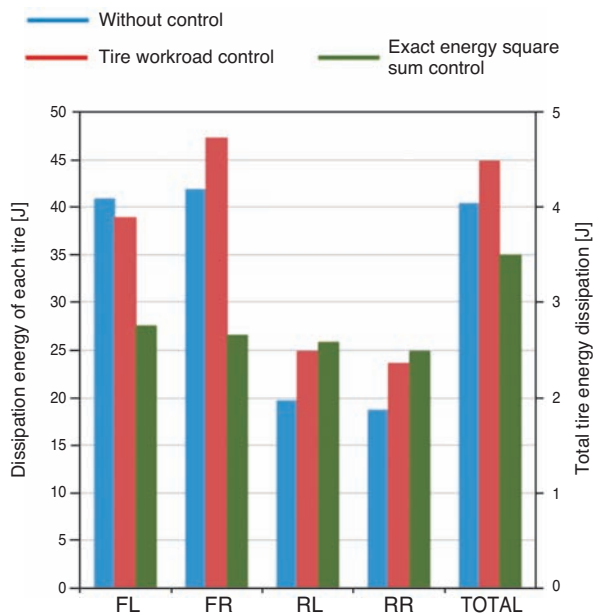


Fig.11 Effects of distribution controls on tire energy dissipation (0.4G lane change)

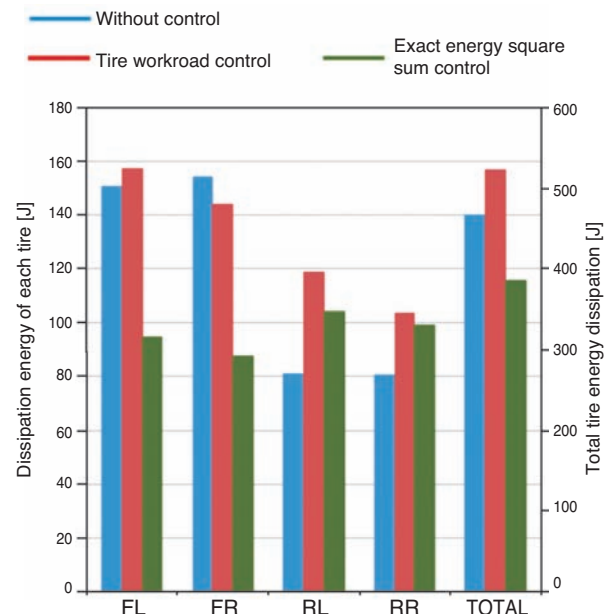


Fig.13 Effects of distribution controls on tire energy dissipation (0.6G lane change)

4. Challenges

I have given an overview of the past active control approaches for vehicle motion and described an ultimate intelligent integrated active motion control vehicle for electric vehicles and indicated that it is not merely a desk theory.

Although this approach can basically realize any response to the steering, the method that can be generally discussed to determine which response is to be realized is not yet proposed or established. This is an old issue about the relation between a driver's subjective evaluation of the vehicle steering properties and objective vehicle motion performance. This indicates that the method that depends on the driver's feeling is not reduced to the general method for vehicular motion performance design. The vehicle should be easily maneuverable and highly perceived by a driver and the vehicular motion performance design should contribute to safety and also be "fun to drive."

We have recently proposed a method to evaluate vehicular motion performance using a driver model of simple steering angle control by identifying key parameters of the model from the actual driver's behavior and vehicle motion^{13), 14)}. The driver parameters identified in this method reflects the vehicle motion performance and this method should provide a reasonable logic between the objective motion performance and the driver's evaluation. We have seen many examples where the evaluation of motion performance from this method matches with the driver's sensory evaluation very well. One of the ongoing challenges should be to explore which response to the steering that must be realized by the ultimate vehicle active motion control based on, for example, this method.

Also, when "steer by wire" or "drive by wire" is equipped, how to set the steering reaction will become an important issue, as briefly mentioned earlier. Currently, there is no generally established method. The steering reaction is not an issue directly related to the vehicle motion performance. Rather, it is an issue of the driver's evaluation. Although it is not an issue of the motion performance itself, in our recent research we found that by changing the steering torque property in the steering angle control driver model mentioned earlier without changing any parameters in the model for vehicle motion properties at all, the model parameters would change in concert with the sensory evaluation as if the vehicle motion performance had changed¹⁵⁾. It is quite interesting in

how to set the steering torque as well as how to apply the method using this driver model and should also be one of the important challenges for the ultimate intelligent integrated active motion control vehicles.

Reference

- 1) Y. Furukawa and M. Abe "Advanced chassis control systems for vehicle handling and active safety" *Vehicle System Dynamics*, Vol. 28, pp. 59-86, 1997.
- 2) M. Abe "Vehicle dynamics and control for improving handling and active safety: from four-wheel steering to direct yaw moment control" In proceeding of *IMechE*, Vol. 213, part K, pp. 87-101, 1999.
- 3) G. Mastinu, E. Babbal, P. Lugner, D Margolis, D. Mittermayr and B. Richiter "Integrated controls of lateral vehicle dynamics" *Vehicle System Dynamics*, Supplement 23, Vol.23, pp.358-377, 1994.
- 4) S. Sato, H. Inoue, M. Tabata and S. Inagaki "Integrated chassis control system for improved vehicle dynamics" In proceedings of the *AVEC92*, pp.413-418, 1992.
- 5) T. Gordon, M. Howell and F. Brandao "Integrated control methodologies for road vehicles" *Vehicle System Dynamics*, Vol.40, pp157-187, 2003.
- 6) M. Abe "A Study on Effects of Roll Moment Distribution Control in Active Suspension on Improvement of Limit Performance of Vehicle Handling" *JSAE Review* Vol.12, No.3, July 1991
- 7) O. Mokhiamar and M. Abe "Simultaneous optimal distribution of lateral and longitudinal tire forces for the model following control" *Transactions of the ASME, Journal of Dynamic System, Measurement and Control*, Vol.126, pp753-763, December 2004
- 8) P. Reinold, V. Nachtigal and A. Traechtler "An advanced electric vehicle for development and test of new vehicle dynamics control strategies" *Proceedings of IFAC AAC2010, Munich, July 2010 in CD*
- 9) N. Bajcinca and Y. Kouhi "Distributed optimization for feed-forward global chassis control" *Proceedings of IFAC AAC2010, Munich, July 2010 in CD*
- 10) M. Abe "Evaluation of active vehicle motion controls from tire energy dissipation points of view" *Keynote presentation of AVEC2012, Proceedings of 11th International Symposium on Advanced Vehicle Control Seoul, Korea, August 2012 in CD*

- 11) M. Abe et al. "Tire Force Distribution Control to Reduce Energy Dissipation Due to Tire Slip During Vehicle Motion for Full Drive-by-Wire Electric" Vehicle Proceedings of Chassis tech – plus, Munich Germany, June 2013 in CD
- 12) M. Abe et al. "A study on active vehicle chassis control reducing dissipation energy by tire slip for full drive-by-wire electric vehicle" to be presented at 23rd IAVSD symposium, Qingdao, China, August 2013
- 13) Jun ISHIO et al. "Vehicle Handling Quality Evaluation through Model Based Driver Steering Behavior" Proceeding of 20th IAVSD Symposium, Berkeley August 2007
- 14) Yasuhiro Aoki, Yoshio Kano and Masato Abe "Variable Stability Vehicle with Response Parameters Controlled by Active Chassis Control Devices" Proceedings of 22nd IAVSD symposium, August 2011, in CD
- 15) M. Hibi et al. "A study on steering reactive torque for steer-by-wire vehicle using driving simulator" Proceedings of FISITA2012, F2012-G04-006, Beijing, China, November 2012, in CD

〈 *Author biography* 〉

Masato Abe

Doctor of Engineering, Professor, Department of Vehicle System Engineering, Kanagawa Institute of Technology

1971	Completed doctor course, School of Engineering, The University of Tokyo, Doctor of Engineering
1980	Assistant Professor, Department of Mechanical Engineering, Kanagawa Institute of Technology
1987	Professor, Department of Mechanical Systems Engineering, Kanagawa Institute of Technology
1995-1996	Visiting Professor, Mechanical Engineering, University of Leeds
2006	Professor, Department of Vehicle System Engineering, Kanagawa Institute of Technology

【Research fields】

Vehicle motion dynamics, Active control of vehicle motion, Man-vehicle system, Driving assistance, Preventive safety

【Academic society and committee affiliations】

1992-Present	Editorial Board Member of VSD Journal - Official Organ of International Association for Vehicle System Dynamics
1995-2005	Trustee of International Association for Vehicle System Dynamics (affiliated to IUTAM)
1995-Present	Editorial Board Member of Proceedings for I.Mech.E. Part D
1996-2002	Chairman, Technical Paper Editing Committee, Society of Automotive Engineers of Japan
1998-2004	Trustee, Technology, General Affairs, Society of Automotive Engineers of Japan
2001-2006	Co-editor of VSD Journal
2006-2011	Vice president of International Association for Vehicle System Dynamics and assumed several positions at the Society of Automotive Engineers of Japan including Trustee, Representative, Member/Chairman of Committees and General Chairman of International Conferences. Fellow, Society of Automotive Engineers of Japan

NTN Module Technology Contributes to Energy Efficiency and CO₂ Reduction in Automobiles

Takehiko UMEMOTO



In recent years the pursuit of environmental performance, through fuel efficiency improvements for CO₂ reduction and the re-use of energy, together with the pursuit of advanced electronic controls for safety and comfort, is progressing rapidly in the automotive sector.

NTN are traditionally developing and supplying mechanical components such as bearings that reduce heat generation, friction and energy loss. More recently NTN is supplying automotive manufacturers with Energy Efficiency Improved Module products that comprise of several different component parts.

This article introduces NTN Module Product lines which are a significant contributor to the improvements seen in automotive energy efficiencies.

1. Introduction

Recently, fuel economy for domestic automobiles has made big strides achieving up to 36.4km/L at JC08 mode (reviewed by the Ministry of Land, Infrastructure, Transport and Tourism) with commercially available automobiles in the market as of September, 2013. The low fuel consumption is a result of implementing several technological advancements including light-weight body, hybrid system, idling stop function, CVT (continuous variable transmission), variable valve timing system, cylinder rest engine, etc.

In an automobile more than 100 bearings are used that contribute to the reduction of energy loss and heat generation, which are generated by the friction of many components. At NTN we are developing thinner and lighter bearings with higher load capacity and longer service life by adopting advanced analytical technology for high efficiency, high functionality, extremely clean materials, special heat treatment, etc. Consequently, we announced and introduced ULTAGE Series *1 in the market as high-function, next-generation bearings.

In addition to these high-function bearings, we developed module products where the ball screw, constant-velocity joint, gear, motor, etc are integrated

with the peripheral components and have been supplying them to automobile manufacturers. These module products are contributing to lower-fuel economy and the improvement of environmental performance by reuse of energy and pursuit of safety and comfort by state-of-the-art electric control.

In the following sections, I would like to introduce our module products and their technology used in the hub, brake, AMT (automatic manual transmission), engine variable valve actuation mechanism, CVT (continuous variable transmission), and engine chain system.

2. NTN module technology

Table 1 shows examples of our module product lines for automobiles which are currently in production or which development is completed.

The module products are expanding to every part of the automobile including the engine, brake, hub, and transmission, contributing to lighter-weight, more compactness, and higher efficiency by combining parts or in the combining of parts with peripheral components.

The uses and features of the module products in **Table 1** are introduced next.

*1 ULTAGE is a name created from combining the words "ultimate", signifying refinement, and "stage", signifying NTN's intention that this series of products will be employed in diverse applications and is the general name for NTN's new generation of bearings that are noted for their industry-leading performance.

Table 1 NTN Module product lines

Area of application	Drivetrain	Brake	
Module product name	Press connect spline hub joint	Ball screw drive module for electro hydraulic brake	Electromechanical braking unit with parking brake
Characteristics	Compact Light weight	Highly efficient regeneration mechanism Small form factor/light weight	Reduction of environmental load Highly efficient regeneration mechanism Small form factor/light weight
Appearance			

Area of application	Manual transmission	Engine
Module product name	Ball screw actuator for gear shift unit	Ball screw actuator for variable valve event & lift mechanism
Characteristics	Improved fuel economy Improved comfort High response	Improved fuel economy Cleaner gas emission Enhanced engine output
Appearance	<p>Shift side</p>  <p>Select side</p> 	

Area of application	Continuous variable transmission (CVT)	Engine chain system
Module product name	Hollow ball screw unit for driving pulley	Low friction chain lever/chain guide
Characteristics	High efficiency Light weight/compact High response	Reduced friction loss Improved fuel economy Appearance
Appearance		 Lever  Guide

3. Press Connect Spline Hub Joint PCS-H/J

The power from the engine is transmitted to the hub bearings and tires through the drive shaft, as shown in Fig. 1. Currently, the hub bearings (H/B) and constant velocity joint (CVJ) are engaged through splines machined on both CVJ stem and inside H/B.

The torque is transmitted through the spline teeth surface. This surface is not completely mated because of the difference of tooth pitch due to the process accuracy. This gap between the teeth leads to backlash and the length of engaged splines must be increased in order to obtain the required torque capacity.

With the new technology of press connect spline hub joints (PCS-H/J), a special spline (groove and raised feature) is machined on the CVJ stem and a spline with tooth width smaller than the CVJ stem is

machined within the inner diameter of H/B, as shown in Fig. 2 (b). They are forcibly engaged by bolt tightening and the splines within the inner diameter of H/B are elastically deformed.

NTN calls this joint method the "Press Connect" method. In the press connect method, the engaged surfaces are completely mated and transmit the torque with the entire surface of the teeth, therefore, the length of the spline engagement can be reduced. Since this method uses elastic deformation for engagement, the same condition can be obtained no matter how many times they are engaged. By taking advantage of this feature, we were able to downsize the components by methods such as thinning the inner diameter part of the hub ring and bolt fastening mechanism to achieve a lighter underbody (approx. 12% per vehicle). This technology was only made possible by turning the H/B and CVJ into modules with highly efficient fastening.

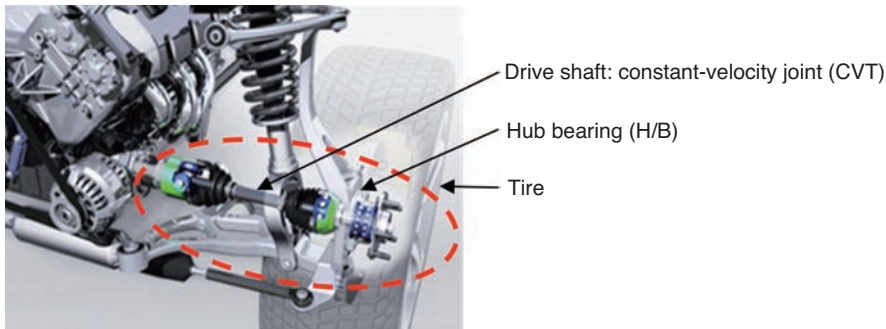


Fig.1 Drivetrain

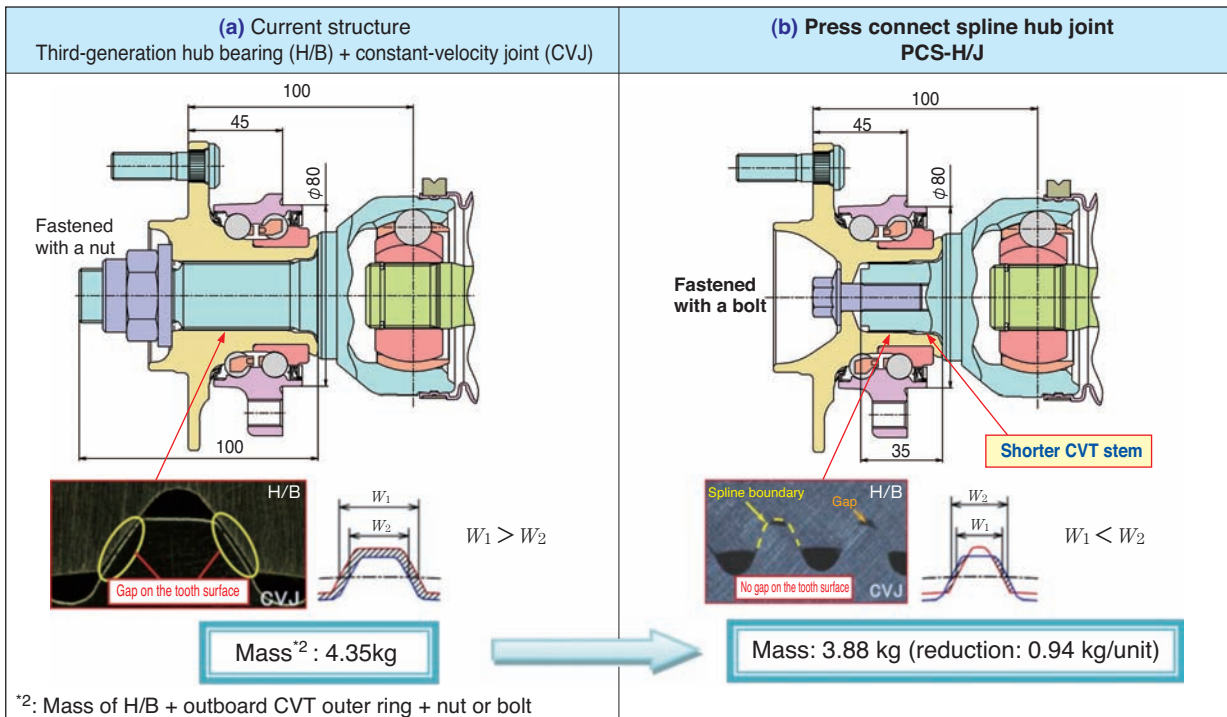


Fig.2 Comparison with "Gen 3H/B+CVJ" and PCS-H/J

4. Ball Screw Drive Module for Electro Hydraulic Brake

The regenerative brake was adopted for electric and hybrid vehicles to recover kinetic energy as electric energy while the brake is applied. In order to recover the most possible electric energy, it is necessary to create a mechanism that uses the motor braking force (regenerative brake) to the maximum and supplement it with hydraulic braking force.

The cooperative control between the regenerative brake and hydraulic brake is also critical, so that the system can immediately respond to the changing braking force.

Fig. 4 shows the construction of Electro Hydraulic Brake (EHB) with a regeneration cooperative brake mechanism. Our “ball screw drive module for electro hydraulic brake” (Fig. 5) was adopted in mass-production vehicles.

The mechanism for this module is explained using the system configuration in Fig. 4 and as follows: When a driver presses the brake, the pedal stroke signal is sent to ECU and the optimum braking force and hydraulic force are calculated. ECU operates the ball screw drive module for the electro hydraulic brake with a DC motor and moves the piston in the hydraulic cylinder to the optimum extent. The hydraulic force produced from the hydraulic cylinder is transmitted to the caliper of each wheel to apply the braking power.

By using the ball screw drive module, quick and precise control and the maximum energy recovery can be achieved. This significantly increased the fuel economy compared to conventional systems achieving the highest fuel efficiency level in the world.

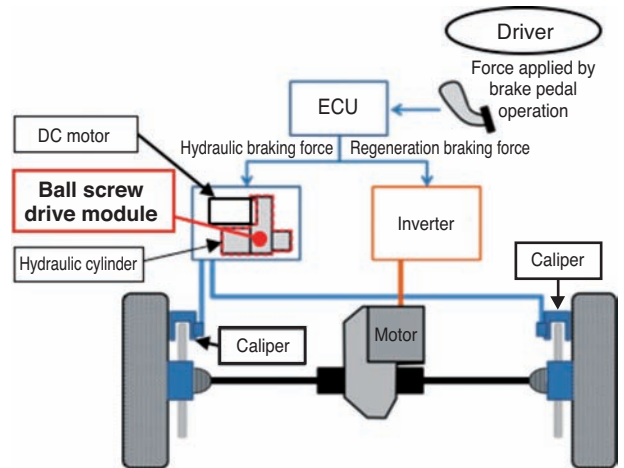


Fig.4 Constitution of electric hydraulic brake

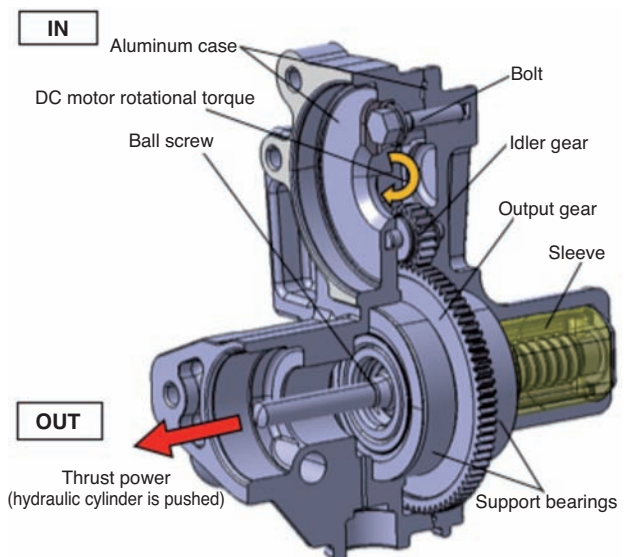


Fig.5 Cross section structure of ball screw drive module

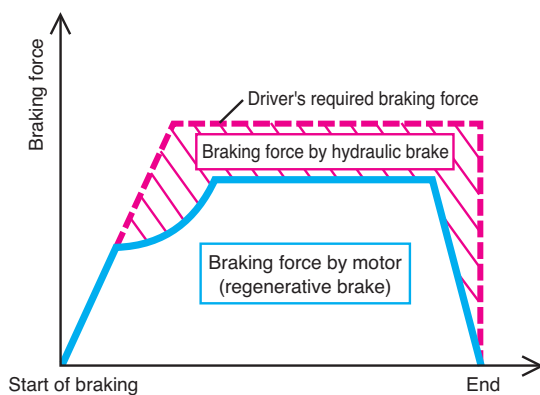


Fig.3 Regeneration cooperative brake

5. Electromechanical Braking Unit with Parking Brake

The regenerative brake technology which recovers kinetic energy as electric energy when the brake is applied is expanding mainly with hybrid and electric cars for improved fuel economy.

Commercially available automobiles today are equipped with hydraulic brake systems; however, as a method for the efficient recovery of energy, EHB (introduced in the previous section) would contribute to highly efficient regeneration.

There is another technology for improving the current hydraulic brake system for highly efficient energy recovery by directly operating the friction brake called Electromechanical Brake (EMB).

Having already developed an electromechanical braking system, NTN developed “Electromechanical Braking Unit with Parking Brake” by adding a parking brake mechanism to the electromechanical brake and

is proposing its adoption.

The mechanism of electromechanical brake and parking brake is explained using the schematic of electromechanical braking unit in Fig. 6. The DC motor attached to the unit drives the rotation of the sun roller in the electromechanical braking unit through the gear reducer. This driving force to the sun roller drives autorotation and revolution of the adjacent planetary roller moving the screw between the planetary roller and the outer ring which drives the outer ring itself toward the axial direction. This axial force of the outer ring is transmitted to the brake pad producing the braking force.

The parking brake mechanism is equipped immediately below the intermediate gear. The pin inside the solenoid is inserted to the ratchet groove set on the reverse side of the intermediate gear to activate the parking brake and is pulled out to release the brake.

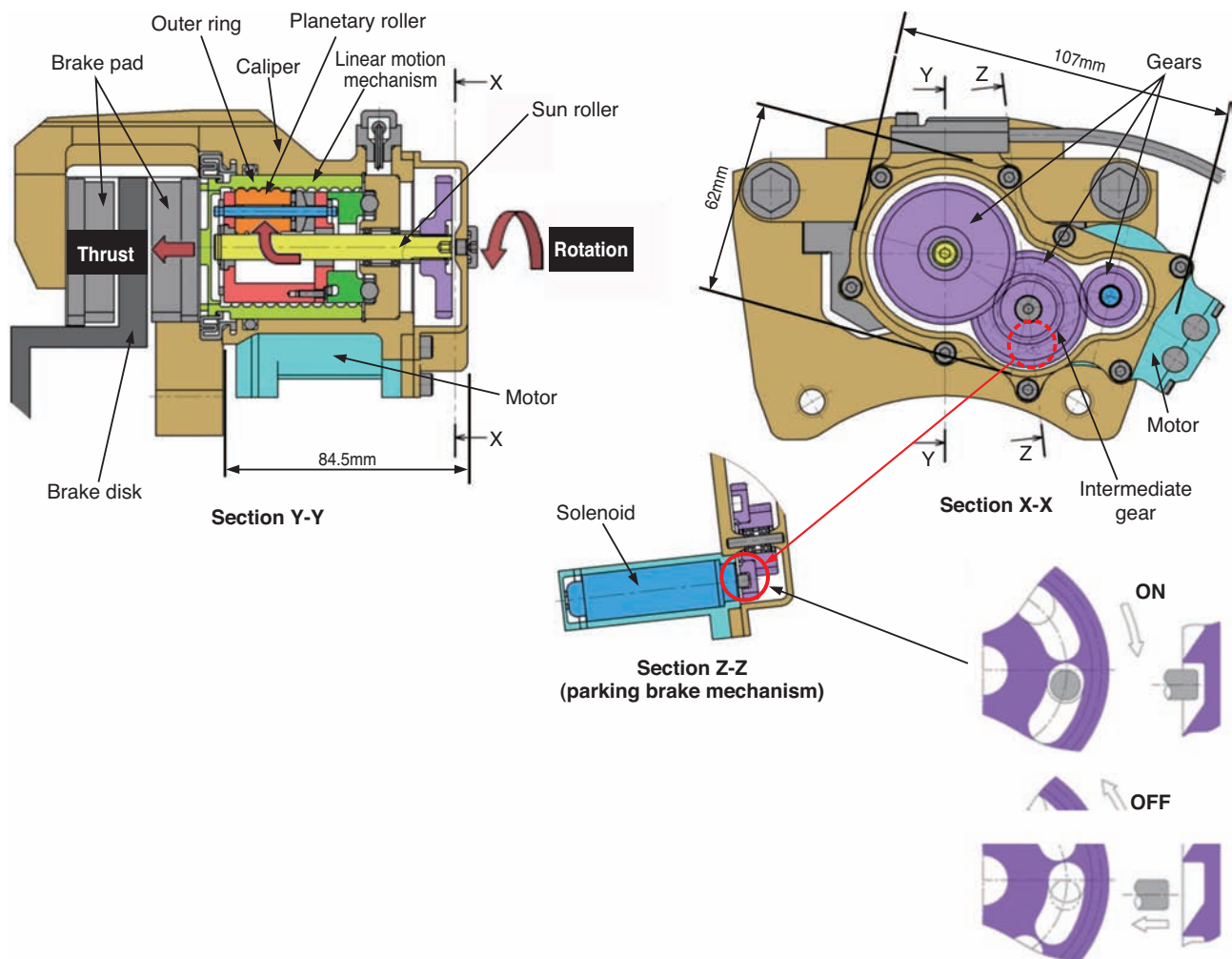


Fig.6 Schematic of EMB unit

6. Ball Screw Actuator for Automated Manual Transmission Gear Shift Unit

Vehicles with automated manual transmission (AMT) are expanding for improved fuel economy and comfort. There are different designs for the structure of AMT. Here, we are describing AMT with a gear shift unit which adopts NTN-developed ball screw actuators.

Since 2004 this gear shift unit has been adopted for mid to small size trucks with a frequent start/stop trend. Fig. 7 shows an external view of AMT and Fig. 8 shows how the gear shift unit is installed.

Fig. 9 shows the structure of the gear shift unit and Fig. 10 shows an external view of the ball screw for the actuator.

The mechanism of operation is explained using the structure diagram of the gear shift unit in Fig. 9. The ball screw actuator on the select side inside the unit moves the striker to the axial direction and then the ball screw actuator on the shift side oscillates the striker to shift the gear to the selected speed. The gear shift is made by cooperative control of the orthogonal ball screw actuator with the motor. The response is very fast with an operation time of 0.06 sec in the shift side and 0.08 sec in the select side.

This AMT is characterized by a compact size without significant change in the structure by installing the gear shift unit on top of the regular manual transmission.

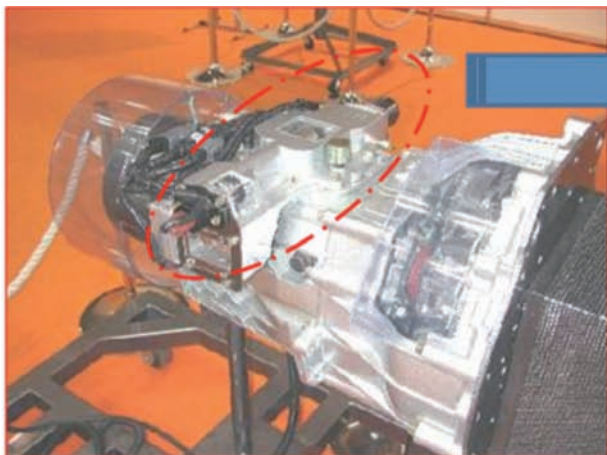


Fig.7 Automated manual transmission

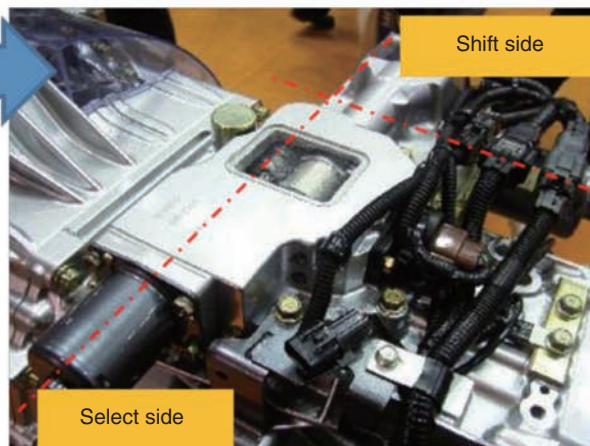


Fig.8 Gear shift unit

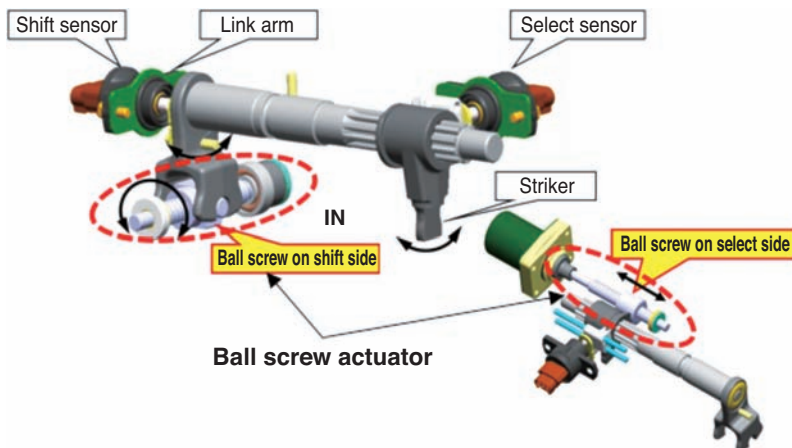


Fig.9 Gear shift unit

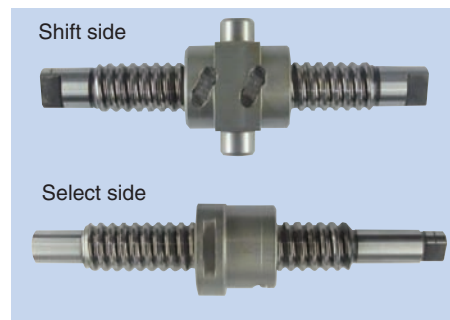


Fig.10 Actuator for ball screw

7. Ball Screw Actuator for Engine Variable Valve Event & Lift Mechanism

For global environmental improvement and enhanced power output, technological development is in progress for refined engine control in order to achieve the optimum response to driving conditions. One of the technologies for the optimum control is the variable valve event & lift (VEL) mechanism. Improved fuel economy and power output are pursued by optimizing the valve open/close timing and the lift volume at the top of the engine. The engine variable valve event & lift mechanism, which adopts our ball screw actuators, has been mass produced and deployed in the market since 2007 for passenger vehicles, sports cars, and RVs.

This mechanism makes instantaneous and precise control possible due to the adoption of the ball screw actuator and achieves improved engine output and response, improved fuel economy of about 10%, and cleaner gas emission.

Fig. 11 shows the variable valve event & lift (VEL) mechanism and Fig. 12 shows the structure of the ball screw actuator. The translatory movement of the nut of the ball screw actuator directly connected to the DC motor controls the rotational phase of the control shaft which is converted to vertical movement of the valve lifter.

This mechanism variably and continuously controls the valve lift and valve event by precisely controlling the movement of the ball screw actuator nut with the position sensor.

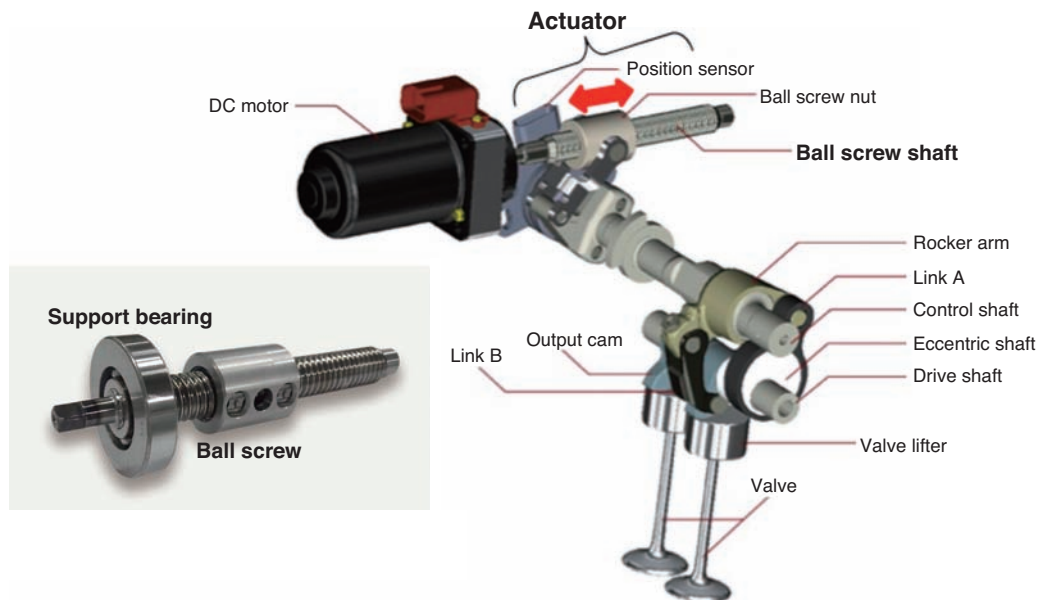


Fig.11 Appearance of VEL system

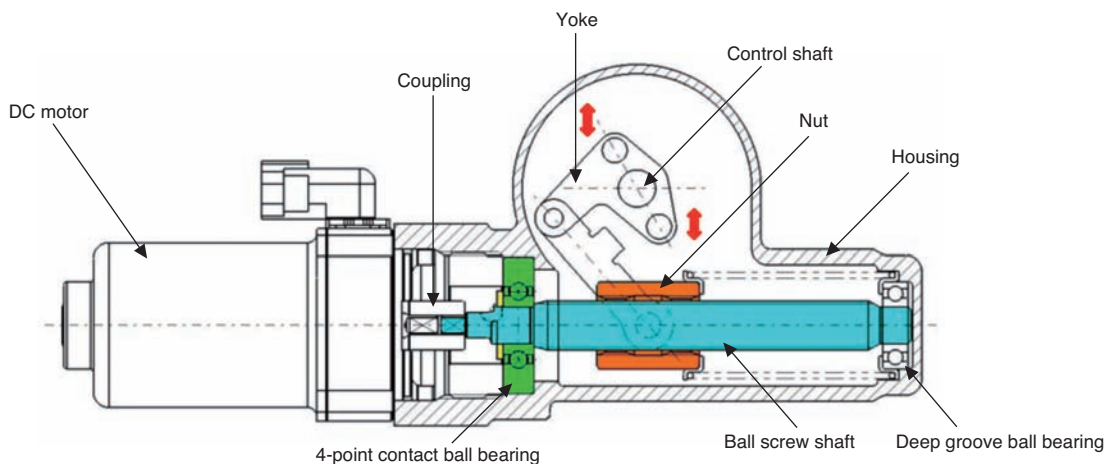


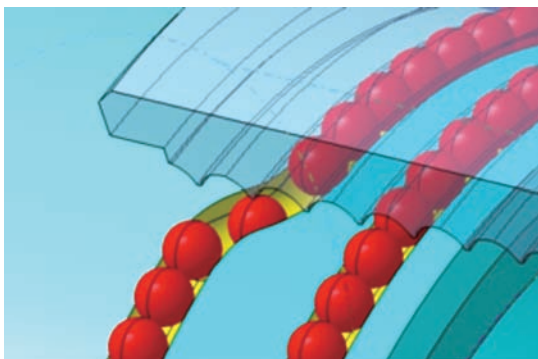
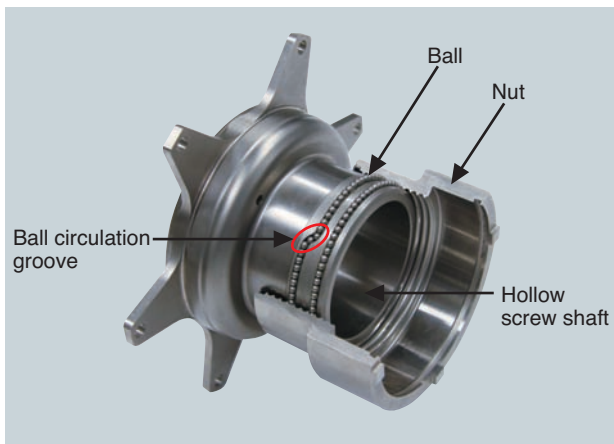
Fig.12 Structure of ball screw actuator

8. Hollow Ball Screw Unit for Continuous Variable Transmission (CVT)

The continuous variable transmission (CVT) ^{*3}, which contributes to fuel economy as well as smooth speed shifting, is currently adopted by many vehicle models.

The pulley driving method of the CVT transmission mechanism is now changed to electronic control from the conventional hydraulic control for more precise speed control and reduced power loss. However, since the current improved electronic control still uses the sliding screw for pulley drive, there is further room for improvement in terms of power loss.

The "Hollow Ball Screw Unit" developed by NTN (Fig. 13) converts the rotational power of the DC motor into axial movement of the pulley with a high efficiency of 70% or more. Due to the light weight, thin, and compact construction of the hollow axis, it



Ball circulation mechanism

Fig.13 Hollow ball screw unit

can be installed coaxially with the pulley driving mechanism. This is a world's first technology that achieved ball circulation at the screw shaft side for the ball screw circulation mechanism.

The example of the structure in Fig. 14 describes a mechanism where the rotational power from the DC motor is transmitted to the hollow screw shaft and the nut fixed to the housing moves the screw shaft with a driving pulley toward the axial direction for changing speed.

By the adoption of the "Hollow Ball Screw Unit," the motion force and electric power loss associated with the pulley drive and the DC motor size can be reduced as well as the downsizing of the entire electronic-controlled CVT driving mechanism.

^{*3} CVT: An abbreviation of Continuously Variable Transmission. The system for changing the speed by adjusting the pulley width by the pulley driving mechanism.

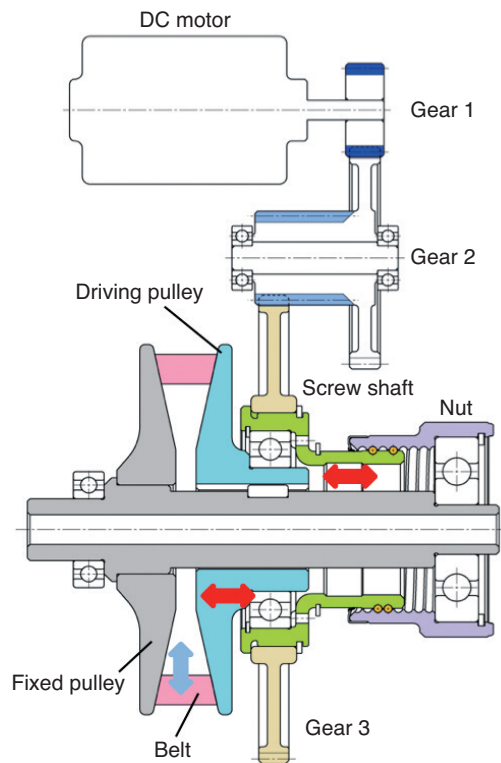


Fig.14 CVT mechanism

9. Low Friction Chain Lever/Chain Guide

It is important to transmit generated power with the timing chain, precisely drive cam shaft, and produce exact valve timing to achieve a high performance engine. Synchronization accuracy and durability are needed for transmitting power and a chain system is composed of the “timing chain”, “sprocket”, “tensioner”, “chain lever” and “chain guide” as shown in Fig. 15.

The friction loss in diverse parts of the engine must be reduced as much as possible for effectively using the generated power.

The ratio of the loss generated in different components is 80% in the crankshaft including pistons, 4% in the cam shaft, and 16% at the chain systems. 1)

The breakdown of the second largest chain system

loss indicates 27% at the chain lever and 13% at the chain guide which suggests a large ratio of friction loss due to the sliding operation of the chain and the lever guide.

We have developed and proposed in the market the low-friction chain lever/chain guide by converting the sliding of the resin lever guide into rolling as shown in Fig. 16.

The low-friction chain lever/chain guide is an addition of the small and highly rigid bearing roller unit onto the current resin-made lever guide. As shown in Fig. 17, the chain does not directly contact the lever or guide but rolls over the bearing roller unit resulting in 22% reduction of friction loss.

The adoption of this low-friction chain lever/chain guide resulted in 1% *4 of improvement in fuel economy for the entire vehicle.

*4 Calculated value based on experimental data

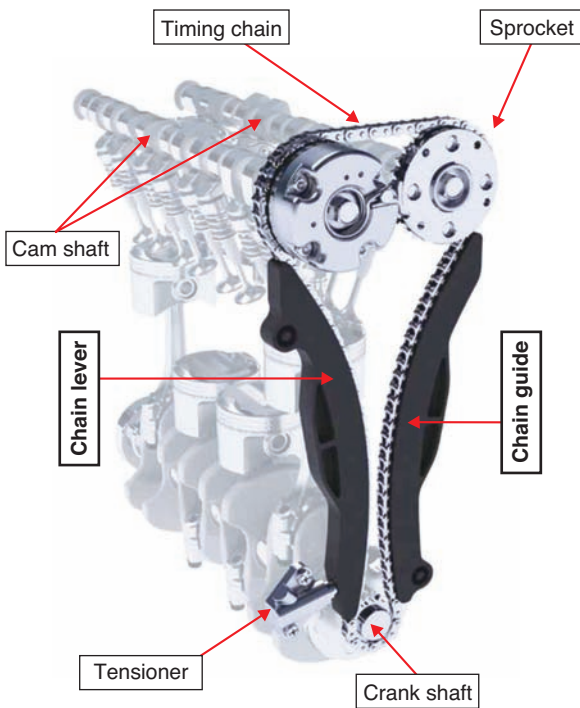


Fig.15 Timing chain system

	Current product	Low friction product
Lever side		
Guide side		

Fig.16 Chain lever and guide

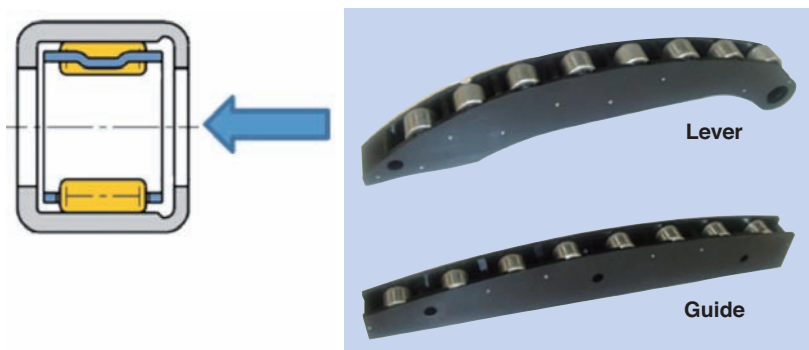


Fig.17 Low friction chain lever and guide

10. Conclusion

I have introduced NTN products already in mass production and adopted by our customers as well as the products which are being developed and currently being proposed to customers among our module technologies and products that contribute to the improvement of energy efficiency of vehicles.

Traditionally, NTN has been contributing to the high functionality and high energy efficiency of individual elements such as bearings, CVJ, and ball screws. NTN considers that further enhancements, improvements, and higher functionality are increasingly important by utilizing module technology where the peripheral components are also integrated. In addition to the improved fuel economy, the pursuit of safety and comfort is becoming quite important in the automotive community.

NTN is striving to continue development of combined technology consisting of our existing technologies such as tribology, machine technology, and mechatronics technology for contributing not only to the vehicles with low-fuel consumption engines but also to the next generation vehicles such as EV, HEV, and FCV.

Reference

- 1) Exhibit: Society of Automotive Engineers of Japan, Academic Conference preprint issue, No. 55-00

Photo of author



Takehiko UMEMOTO
Executive Officer
Automotive Business HQ
EV Module Business HQ

Recent Technology Trends of In-Wheel Motor System for Automotive



Tomoaki MAKINO*
Aiko ISHIKAWA*
Chinami ITOU*
Kayo SAKAI*

In the electric vehicles equipped with in-wheel motors, the degrees of freedom for vehicle design are high because there is no restriction of drivetrain layouts such as drive shaft. Moreover, independent, quick and precise control of driving force of each wheel can be realized by in-wheel motor system, meaning that the driving stability can be improved significantly. This paper describes the technology trends of in-wheel motor system expected to be powertrain for new generation electric vehicle.

1. Introduction

Electric vehicles have recently been drawing attention as possible measures against environmental issues such as global warming, air pollution, and energy issues such as the depletion of fossil fuel.

In-wheel motor electric vehicles have driving motors in the wheels, so the power is transmitted to the tires without needing a differential gear and drive shaft. There is no restriction of the layout caused by the drive train, enabling a higher degree of freedom for the vehicle design. In addition, the vehicle maneuverability can be greatly increased since the driving power can be quickly and accurately controlled for each wheel independently.

NTN has been developing an in-wheel motor system with high mobility functions combining independent wheel driving and steering control as well as a reducer mechanism that effectively contributes to light-weight vehicles.

In this article, we introduce the technology trend of in-wheel motors which holds a high expectation as the driving method for the next-generation electric vehicles and includes NTN's developments.

2. Dawn of in-wheel motor electric vehicles

The history of in-wheel motor vehicles is long. In 1899, Dr. Ferdinand Porsche already developed a series of hybrid vehicles which drove the front wheels with a motor powered by electricity generated by the installed engine. **Fig. 1** shows the structure of the in-wheel motor patented by Dr. Porsche. It used a direct drive method with no reducer and the in-wheel motor of essentially the same structure was installed in the vehicle mentioned above.

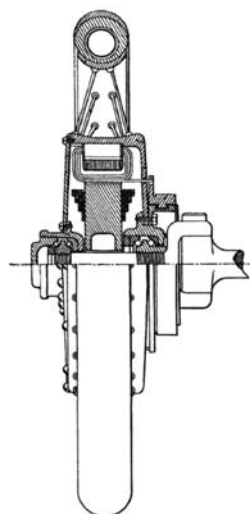


Fig. 1 Structure of the first in-wheel motor 1)

* Drive System Engineering, EV Module Business HQ

Back in those days, performance of the battery and motor was not high enough and had a short driving range so the vehicle performance was insufficient. Electric vehicles started losing their competitive edge with the development of oil resources and improved availability of gasoline as well as the cost reduction of reciprocal engine vehicles starting with the mass production of the Ford T model in 1908.

Subsequently, the era of full-scale development of motorization with reciprocal engine vehicles started. In the 1970s, oil supply concerns presented by the oil crisis and environmental issues such as air pollution due to exhaust gas started emerging. Electric vehicles were looked as a measure against those issues; however, they did not evolve into one due to problems such as battery performance, etc.

In the 1990s and thereafter, performance of electric vehicles significantly increased due to the development of (1) a lithium-ion battery which has higher energy/output density compared to the conventional lead battery, (2) a permanent magnet synchronous motor using neodymium magnet and (3) inverter-based motor control technology. As the global warming issues due to greenhouse gas such as CO₂ are widely recognized, electric vehicles and the development of in-wheel motor is attracting attention in recent years.

3. Structure of in-wheel motor

As shown in Fig. 2, drive systems of electric vehicles are broadly divided into the onboard system, which installs a motor in the body and transmits the power to the tires through a drive shaft, etc, and an in-wheel motor system which installs motors inside the wheels.

The in-wheel motor system is further subdivided into a direct drive system, which does not equip a reducer and a system which employs a reducer concurrently.

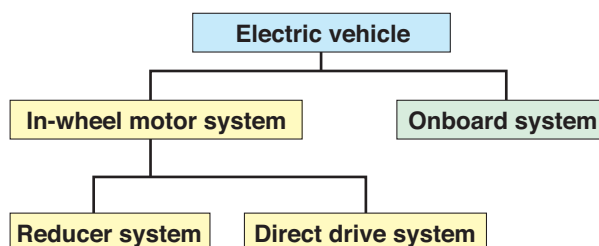


Fig. 2 Classification of electric vehicle by driving system

3.1 Direct drive system

Many of the direct drive systems developed so far adopt the outer rotor method which places the rotor on the outside of radial direction from the stator²⁾⁻⁴⁾. Fig. 3 shows an example of its structure. A case of development of vehicles with in-wheel motors of this system is also reported³⁾. Fig. 4 shows an appearance of such a vehicle.

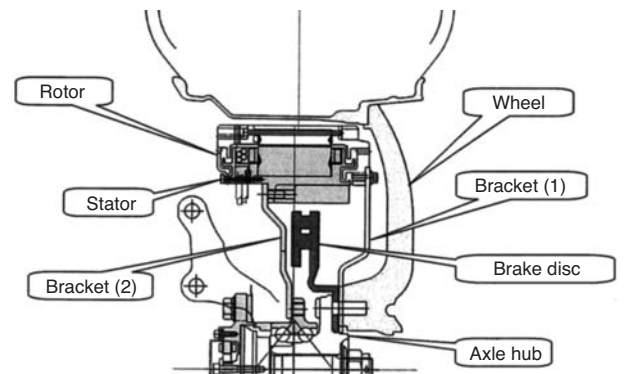


Fig. 3 An example of the structure of direct driving system in-wheel motor²⁾



Fig. 4 Developed vehicle equipped with direct driving system in-wheel motors³⁾

3.2 Reducer system

Although using a reducer brings some disadvantages such as complex structure with an increased number of components, the torque required for the motor can be reduced which allows for a smaller motor size resulting in a more compact and lighter in-wheel motor as a whole.

Many cases of development of in-wheel motors of this method are reported⁵⁾⁻⁹⁾. Fig. 5 and 6 show some examples of those cases. The example of Fig. 5 adopts a reducer with the planetary type reduction gear and the example of Fig. 6 adopts both the reducer with planetary type reduction gear and the parallel shaft type reduction gear.

Fig. 7 and Fig. 8 show the basic structure of cycloid reducer, which is K-H-V type planetary type reduction gear, and the structure of in-wheel motor that NTN developed using this reduction gear^{10), 11)} respectively. This reduction gear consists of a cycloidal disc that has an epitrochoid curve and multiple ring gear pins placed at equal intervals on the

circumference. Only the rotation movement of the eccentrically revolving cycloidal disc is transmitted to the output shaft, located inside the cycloidal disc. Since the cycloid reducer is able to provide a large reduction ratio with only one stage, it is superior to other reducer systems for its compact size and light weight.

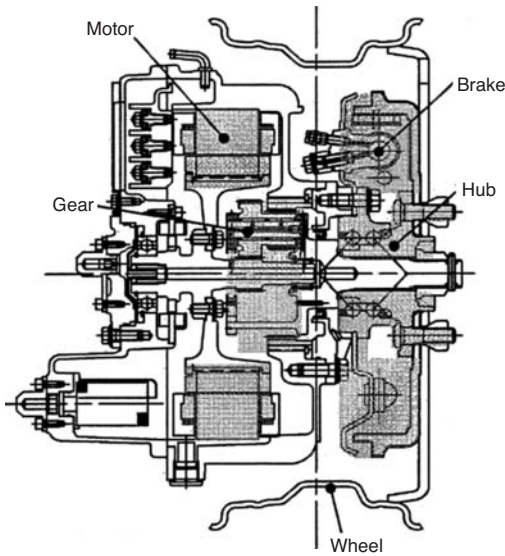


Fig. 5 An example of the structure of reducer system in-wheel motor⁸⁾

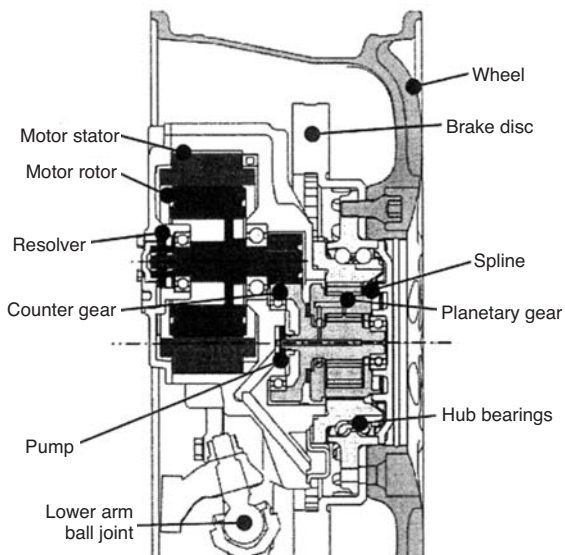


Fig. 6 An example of the structure of reducer system in-wheel motor⁹⁾

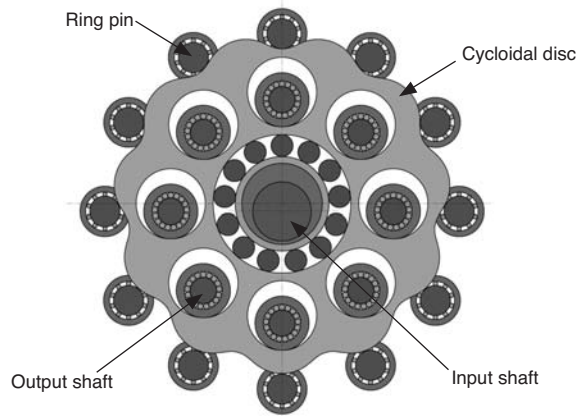


Fig. 7 Cycloid reducer

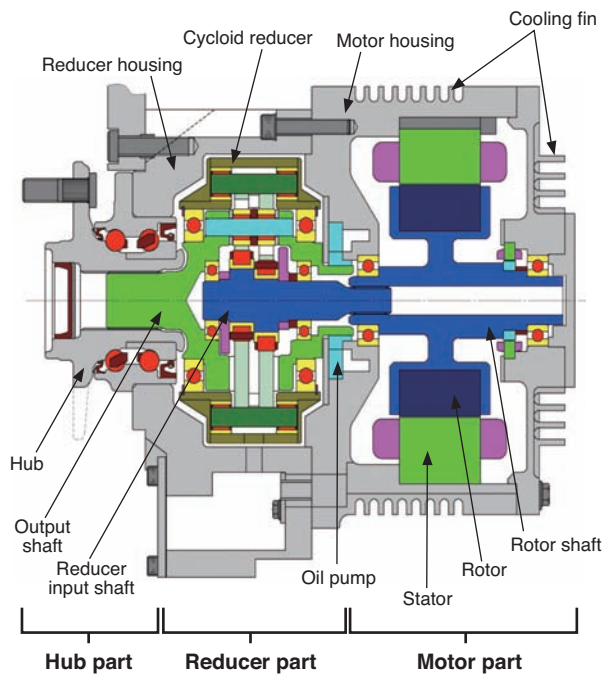


Fig. 8 In-wheel motor with cycloid reducer¹¹⁾

4. Impact of unsprung mass

In general, an in-wheel motor system increases the unsprung mass compared to an onboard system, which adversely affects the comfort and road-hugging property of the tires.

The basic oscillation model for a suspension system includes a two-degree of freedom oscillation model considering sprung and unsprung masses. Fig. 9 shows the sprung mass acceleration based on this oscillation model. As the unsprung mass increases, the unsprung resonance frequency decreases and the sprung acceleration in the low frequency range increases¹²⁾. Humans are most sensitive to a vertical vibration of 4-8 Hz¹³⁾. Therefore, an increase of the sprung acceleration in this range due to increase of unsprung mass significantly reduces the comfort level. It also reduces the followability of unsprung mass to the irregularities of the road surface which adversely affects the road-hugging property of the tires.

Several reports on the impact of in-wheel motors to the increase of unsprung mass are available^{14), 15)} so reducing the weight of in-wheel motors to reduce its impact is critical. In addition, an initiative to address this unsprung mass issue by a mechanism is also underway. For example, a mechanism was developed to prevent adverse effect of riding comfort configuring the motor mass with a movable dynamic damper that is mounted vertically¹⁶⁾.

NTN achieved a significant reduction of in-wheel motor weight by integrating the cycloid reducer as mentioned above.

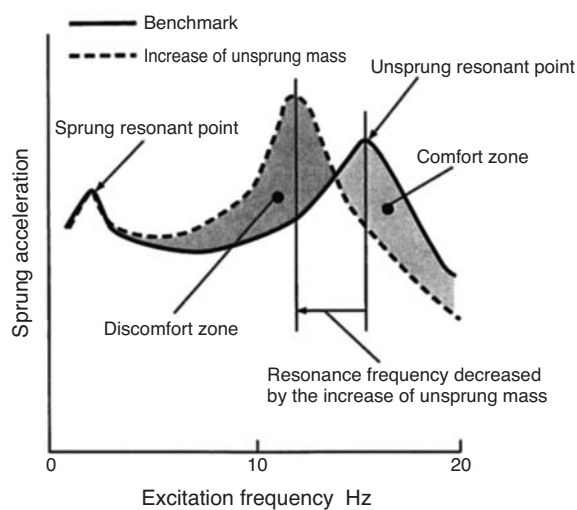


Fig. 9 Effect of unsprung mass on vehicle sprung acceleration¹²⁾

5. Vehicle motion control

The drive motion control by an electric motor has the following advantages over internal combustion engines.

- (1) High torque response
- (2) Highly accurate torque control
- (3) Ability to generate and control braking force
- (4) Independent control of driving force for each wheel by mounting motors in them

In addition, an in-wheel motor system allows further high-response torque control since it is not affected by resonance of the power train such as the drive shaft¹²⁾. It is also able to control braking force with an even higher response than ABS (anti-lock brake system) and hydraulic brakes for traction control used with internal combustion engine vehicles¹⁷⁾.

By using the above properties, particularly electric vehicles with an in-wheel motor system, can control highly advanced vehicle motion which is difficult with internal combustion engine vehicles.

5.1 Anti-slip control

Fig. 10 shows the characteristics of lateral and longitudinal (driving or braking) forces between the tires and road. The characteristics of Fig. 10 can be theoretically derived from a model to consider the tires as infinite elastic bodies independently placed on the

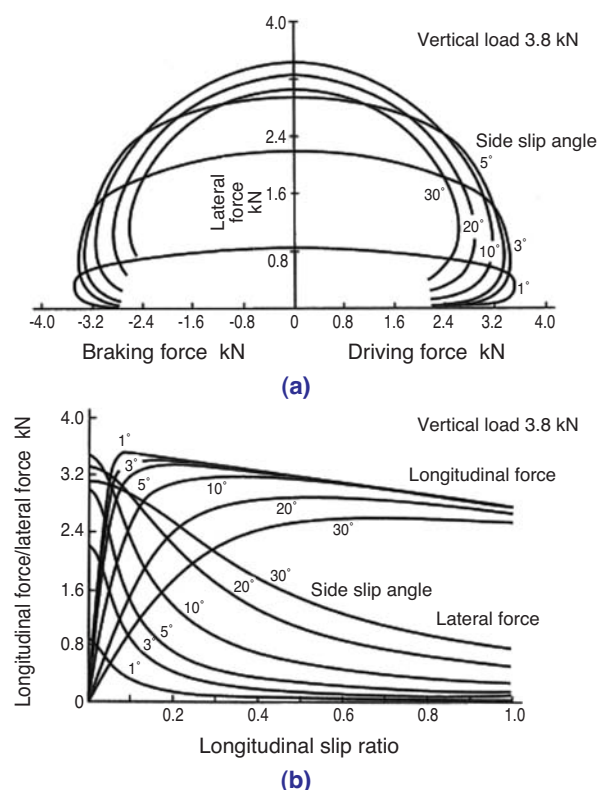


Fig. 10 Tire characteristics with driving and braking¹⁸⁾

circumference. The longitudinal force produced at the tires increases along with the slip ratio and decreases after reaching the peak. Conversely, the lateral force decreases as the slip ratio increases¹⁸⁾.

As the road condition changes and an excessive slip occurs on the tires, both the driving force and lateral force decrease and may cause not only the reduction of acceleration performance but also the loss of directional stability. Therefore, prevention of excessive slip of tires is critical in order to avoid unstable vehicle behavior.

By using the motor driving properties mentioned earlier, electric vehicles can achieve a more superior anti-slip control than internal combustion engine vehicles. Particularly, an in-wheel motor system can provide the most stable control. Several researches were made and reported regarding anti-slip control using an in-wheel motor system, such as the feedback control using the wheel speed and slip ratio control aiming the maximization of driving/braking force¹⁹⁾⁻²¹⁾.

5.2 Vehicle stability control

Under the condition where the tire slip ratio is relatively small and the degree-of-freedom for driving/braking force control is relatively high, the vehicle driving stability can be increased by independently controlling the driving/braking forces of each wheel. For example, since yaw moment can be directly controlled by giving different driving forces to the right and left wheels, the vehicle maneuverability such as the yaw rate followability during steering increases^{22), 23)}.

In addition, the traveling performance can be increased by appropriately controlling the driving force of each wheel. For example, turning performance can be increased by allocating a larger driving force to the wheel which has allowance for tire grip^{24), 25)}. This type of performance improvement can be further increased by controlling the driving force and steering altogether.

Fig. 11 and **Table 1** shows the appearance and main specifications of a test vehicle NTN created. This vehicle has in-wheel motors on all four wheels and the capability to independently steer these four wheels. NTN and Kanagawa Institute of Technology identified that by independently controlling the driving force and the steering angle the energy dissipation of the tires is reduced²⁶⁾, the tire load rate is decreased, and the vehicle limit performance is improved²⁷⁾.

In addition, with an in-wheel motor system the vertical load produced by the driving force through the suspension mechanism becomes larger than a vehicle with a drive shaft since the knuckle that supports the in-wheel motor receives the torque reaction¹²⁾. By



Fig. 11 Test vehicle with four wheel independent driving and steering

Table 1 Main specifications of test vehicle

Body size	2600×1560×1350mm (Length×width×height)
Mass	619kg
Drive system	Four-wheel drive (in-wheel motor)
Steering system	Four-wheel independent steering (steer-by-wire)

taking advantage of this property, the vertical body motion due to the driving power action can be more effectively and independently controlled for each wheel than with drive shaft-driven vehicles, thus improving response to the roll and yaw motions²⁸⁾. The comfort can be also improved by reducing the vehicle roll and pitch motions²⁴⁾.

6. Next-generation mobility

The in-wheel motor system does not require a power train such as a drive shaft for transmitting power. Therefore, vehicle structure and motion not easily accomplished by conventional vehicles can now be achieved.

Fig. 12 shows an example of in-wheel motor application for a two-passenger commuter vehicle designed for short/mid range mobility²⁹⁾. By installing drive motors within the wheels, plenty of passenger and cargo space can be secured despite the size of its compact body. In February 2013, the Ministry of Land, Infrastructure, Transport and Tourism announced the start of a certification program for a "ultra-small mobility" vehicle standard for two-passenger cars smaller than a "light motor vehicle." This is a trial measure for establishing a new vehicle standard expected to be applied for elderly and child-support, tourism and regional promotion, etc. With the establishment of the dedicated standard for this category of vehicles, it is expected that their expansion will be accelerated in the future.

In addition, by combining an in-wheel motor and independent wheel steering mechanism, "sideway motion" and "pivot turning" can be achieved. Fig. 13 shows an example of such a vehicle and Fig. 14 shows the steering for each traveling mode. For "pivot

turning," the wheels are steered so that the axis of rotation of each wheel points to the center of the vehicle. For "sideway motion," all of the wheels are steered perpendicular to the ordinary forward direction³⁰⁾.



(a) Without cowl²⁹⁾



(b) Registered vehicle with cowl

Fig. 12 In-wheel motor type two-seat commuter



Fig. 13 In-wheel motor type electric mobility

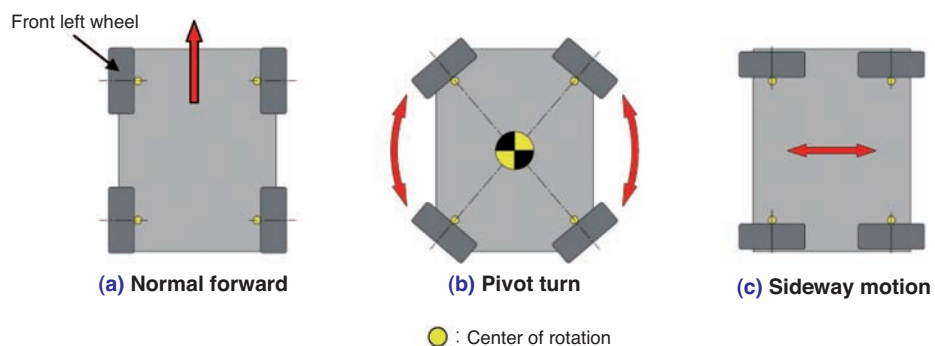


Fig. 14 Steering status at each running mode³⁰⁾

7. Conclusion

In this article, we have described the structure of typical in-wheel motors, initiative for reducing impact of unsprung mass increase and the technological trend of vehicle motion control using in-wheel motors while focusing on the recent development trend. In-wheel motors can realize a level of vehicle motion which is difficult to achieve with conventional vehicles, which makes it an ideal drive system for the next generation electric vehicles. NTN will further improve both the mechanism and control aspects of the system with an aim for early commercialization.

References

- 1) F. PORSCHE : Improvements in or relating to Electrically Driven Road Vehicles, G. B. Patent 18099 (1900).
- 2) YOSHIHIRO OKAMOTO, TOMOAKI KIRITANI, YUKIHIRO NODA: Development of High Efficiency In-wheel Motor System for using 20-inch Wheel Mounted Motor, Toyo Denki Review, Vol. 117 (2008), 12.
- 3) TOMOYUKI SHINKAI, et al.: Development of an Electric Vehicle "SIM-WIL" Journal of Society of Automotive Engineers of Japan, Vol. 66, No. 9 (2012) 84.
- 4) A. WATTS et al. : Integrating In-Wheel Motors into Vehicles-Real-World Experiences, SAE Int. J. Alt. Powerl, 5.1 (2012) 289.
- 5) SHIRO MATSUGAURA, KIYOMOTO KAWAKAMI, HIROSHI SHIMIZU: A Proposal on Chassis Structure and Performance Evaluation for an Electric Vehicle, Transaction of Society of Automotive Engineers of Japan, Vol. 35, No. 3 (2004) 117.
- 6) YASUAKI TAHARA, et al.: Development of the In-Wheel Motor unit, Proceedings of the Society of Automotive Engineers of Japan, No. 131-06 (2006) 9.
- 7) R. S. ZHOU & F. HASHIMOTO : Highly Compact Electric Drive for Automotive Applications, SAE Technical Paper 2004-01-3037.
- 8) YUTARO KANEKO, et al. : Development of compact and high power In-Wheel-Motor unit, Proceedings of the Society of Automotive Engineers of Japan, No. 7-09 (2009) 11.
- 9) SATOSHI MURATA: Development of In-wheel-motor drive unit, Proceedings of the Society of Automotive Engineers of Japan, No. 28-10 (2010) 5.
- 10) MINORU SUZUKI, et al.: Development of In-Wheel Motor Type Axle Unit, NTN TECHNICAL REVIEW, 75 (2007) 46.
- 11) YUICHI ITOH, KAYO SAKAI, YUSUKE MAKINO: In-Wheel Motor System, NTN TECHNICAL REVIEW, 79 (2011) 22.
- 12) HIROAKI YOSHIDA: Evolution of In-Wheel Motor System, Journal of Society of Automotive Engineers of Japan, Vol. 65, No. 3 (2011) 80.
- 13) Society of Automotive Engineers of Japan: Automotive Technology Handbook 1, Introduction/Theory (1990) 269.
- 14) M. ANDERSON et al. : Unsprung Mass with In-Wheel Motors – Myths and Realities, Proc. AVEC'10, (2010) 261.
- 15) R. ROEL et al. : Influence of in-wheel motors on the ride comfort of electric vehicles, Proc. AVEC'10, (2010) 835.
- 16) GO NAGAYA, YASUMICHI WAKAO, AKIHIKO ABE: Development of an –In-Wheel Motor with Advanced Dynamic-Damper Mechanism, Proceedings of the Society of Automotive Engineers of Japan, No. 83-02 (2002) 9.
- 17) F. BOTTIGLIONE, A. SORNIOTTI & L. SHEAD : The Effect of half-shaft torsion dynamics on the performance of a traction control system for electric vehicles, Proc IMechE PartD : J Automobile Engineering, 226, 9 (2012) 1145.
- 18) MASATO ABE: Automotive Vehicle Dynamics (2nd Edition), Tokyo Denki University Press (2012) 38.
- 19) YOICHI HORI: Future Vehicle driven by Electricity and Control -research on four-wheel-motored, SEISAN KENKYU Vol. 56, 2 (2004) 131.
- 20) MOTOKI SHINO, YOSHIAKI OHSHIMA, MASAO NAGAI: Wheel Velocity Control of Micro-Scale Electric Vehicle for Improving Directional Stability, Transactions of the Japan Society of Mechanical Engineers Series C, Vol. 70, No. 694 (2004) 1680.
- 21) HIROSHI FUJIMOTO, MASATAKA YOSHIMURA: Driving Force Control for Electric Vehicle Based on Slip Ratio Control, Proceedings of the Society of Automotive Engineers of Japan, No. 3-11 (2011) 11.
- 22) MAKOTO KAMACHI, KEVIN WALTERS, HIROAKI YOSHIDA: Improvement of Vehicle Dynamic Performance by Means of In-Wheel Electric Motors, Mitsubishi Motors Technical Review, No.18 (2006) 107.
- 23) F. BRAGHIN & E. SABBIONI : Development of a control strategy for improving vehicle safety in a hybrid vehicle with four independently driven in-wheel motors, Proc. AVEC'10, (2010) 91.

- 24) DAISUKE AKAHO et al.: Development of Vehicle Dynamics Control System for In-Wheel-Motor Vehicle, Proceedings of the Society of Automotive Engineers of Japan, No. 120-10 (2010) 1.
- 25) J. KANG, Y. KYONGSU & H. HEO : Control Allocation based Optimal Torque Vectoring for 4WD Electric Vehicles, SAE Technical Paper 2012-01-0246.
- 26) RYOJI NAKAJIMA et al.: The Effects of tire force distribution control on reducing tire slip energy dissipation, Proceedings of the Society of Automotive Engineers of Japan, No. 30-13 (2013) 21.
- 27) YUDAI SUZUKI et al.: A study on effects of tire force distribution control on vehicle motion with Full-Drive-By-Wire EV, Proceedings of the Society of Automotive Engineers of Japan, No. 30-13 (2013) 25.
- 28) ETSUO KATSUYAMA: Decoupled 3D Moment Control by In-Wheel Motor, Proceedings of the Society of Automotive Engineers of Japan, No. 3-11 (2011) 1.
- 29) TETSUYA YAMAMOTO, AIKO ISHIKAWA, WATARU YAMADA: Development of In-Wheel Motor System for Electric Commuters, NTN TECHNICAL REVIEW, No. 79 (2011) 29.
- 30) AKIRA YAMAGATA et al.: Development of Two-seat Electric Mobility with In-Wheel Motors NTN TECHNICAL REVIEW, No. 79 (2011) 51.

Photo of authors (titles are at the time of development)



Tomoaki MAKINO
Drive System Engineering
EV Module Business HQ



Aiko ISHIKAWA
Drive System Engineering
EV Module Business HQ



Chinami ITOU
Drive System Engineering
EV Module Business HQ



Kayo SAKAI
Drive System Engineering
EV Module Business HQ

Electro-mechanical Brake Unit with Parking Brake

Tatsuya YAMASAKI*
Makoto MURAMATSU*
Yui MASUDA**



The new brake technology such as regenerative braking and Electric Parking Brake (EPB) has been spreading in order to meet the demands to improve the fuel economy and convenience of vehicles. It needs to utilize Electro- mechanical Brake (EMB) which is the final form for the further advanced features of brake.

NTN has developed the EMB unit which has parking brake function.

1. Introduction

Electric parking brakes (EPB)¹⁾ that operate the parking brake by an electric actuator and a regenerative brake which recovers vehicle kinetic energy as electric energy by motor, etc. are growing among brake related technologies.

Two types of EPBs are commercially available, namely, the type that installs a dedicated electric actuator on hydraulic brake caliper and the type that pulls the wire of the conventional parking brake mechanism with an electric actuator. EPBs have several advantages such as improved convenience with automatic uphill start assistance and space saving in the cabin by replacing the parking brake lever with a switch.

A regenerative brake is a technology to recover the vehicle kinetic energy as electric energy when the brake is applied. This helps to improve the fuel efficiency (electric cost) and its use has been expanding mainly with the hybrid and electric vehicles which use motors for driving power. In addition, some vehicle engines which recover the vehicle kinetic energy by alternators, etc. and use the energy as the power source for auxiliary equipment are also recently being commercialized. In order to efficiently recover energy using a regenerative brake, it is important to

use coordinated control technology with a service brake which uses friction for obtaining braking force. The commercial vehicles control the service brake using an electric-powered hydraulic actuator²⁾⁻⁵⁾, however, not only brake oil that has high environmental load is used with the current hydraulic system. Due to the insufficient response, it is also difficult to maximize recovery of kinetic energy. As a means to solve this issue, brake manufacturers are developing an electro-mechanical brake (EMB) that operates the service brake by mechanically controlling brake pistons using rotation of the motor.

NTN has been developing and is proposing compact and light actuators for electro-mechanical brakes using our proprietary linear motion mechanism⁶⁾⁻⁹⁾. We have now developed an electro-mechanical brake unit with a newly added parking brake function and revisited the internal design to further reduce its compact size and enhance its performance. In this article, we are introducing the structure of the improved actuator and characteristics of the electro-mechanical brake unit.

*Chassis System Engineering, EV Module Business HQ

**Control Systems Engineering, EV Module Business HQ

2. Structure of electro-mechanical brake unit with parking brake

2.1 Electro-mechanical brake unit

Fig. 1 shows an appearance of an electro-mechanical brake unit developed for the rear wheels of 1500cc-class vehicles and Fig. 2 shows its internal structure. In addition, Table 1 and 2 show the specifications of the unit and the motor used in the unit.

This unit has a linear motion mechanism and a motor equipped in parallel and parallel shaft gears are used for the transmission of torque between them. The torque produced by the motor is transmitted to the linear motion mechanism via the gears and converted to the load (hereinafter, “pressure”) to press the pad onto the disc. To reduce the size of the entire unit, a planetary roller screw mechanism⁶⁾ of NTN's own

invention is used for the linear motion mechanism. This mechanism has a high load conversion ratio (ratio of output pressure over the input torque); therefore, the reduction ratio of the gear train can be low which contributes to the small size of the entire unit.

In this development, we have revisited each element of design to reduce the volume of the actuator by 30% compared to the conventional product (developed in 2011) and in addition, improved the response, as described later.

Furthermore, we have added a parking brake mechanism to the gear area as a new function. With this function, no separate parking brake is necessary for the vehicle with expected improvement on the assembly work and cost. The parking brake mechanism is described in the next section in detail.

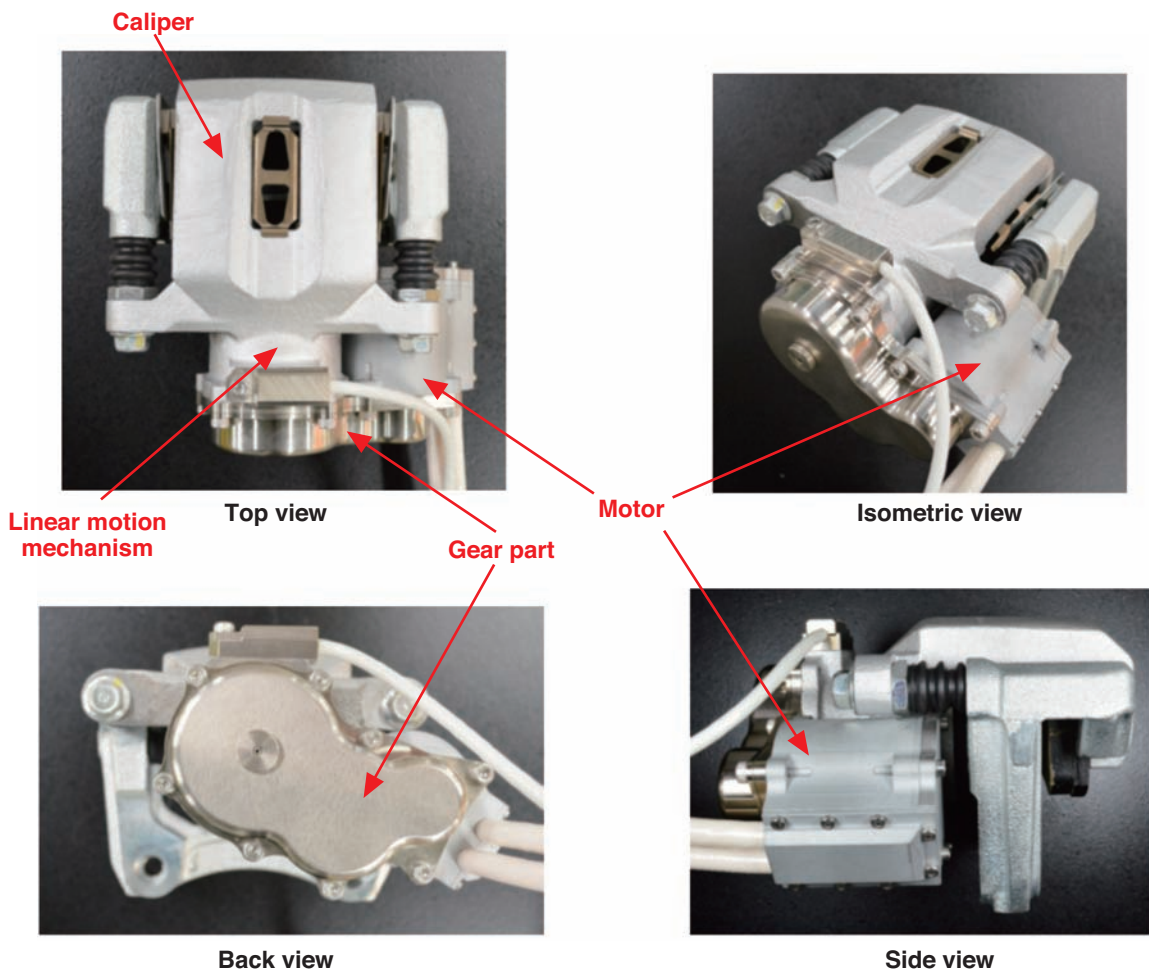


Fig. 1 EMB unit

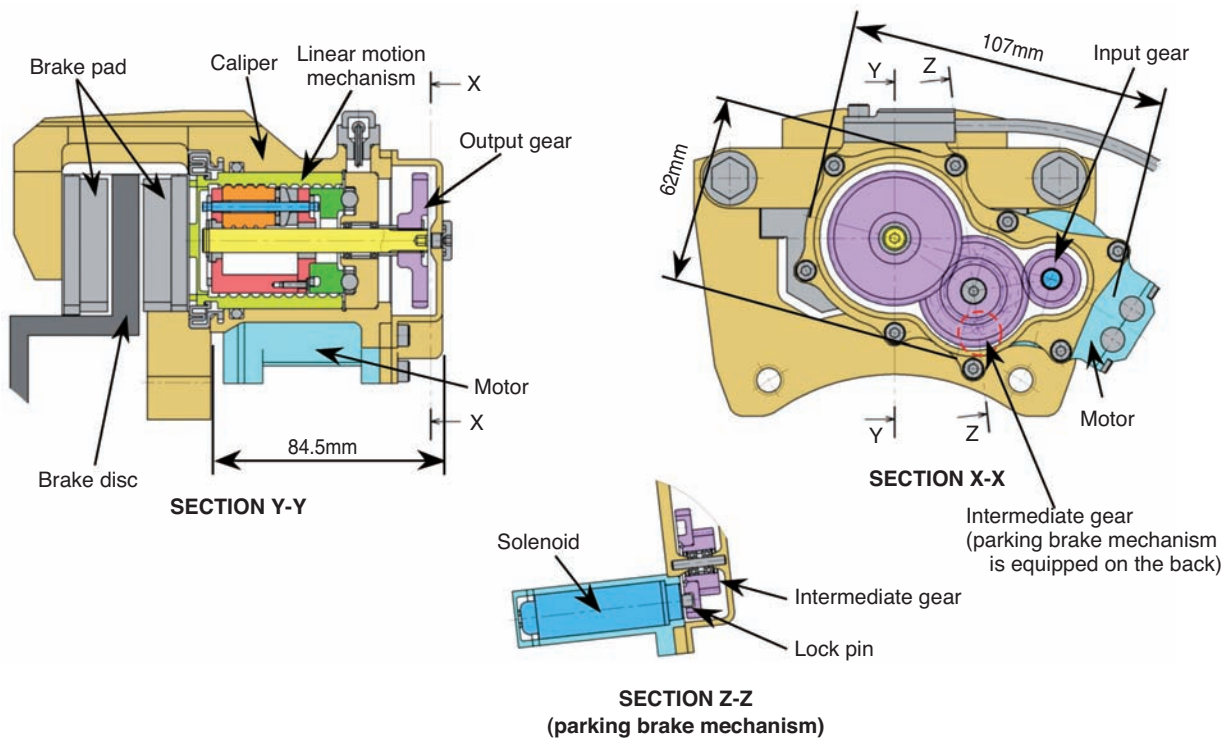


Fig. 2 Schematic of EMB unit

Table 1 Specification of EMB unit (for the rear wheels of 1500cc-class vehicles)

Item	Specification	Remarks
Service brake pressure	12 kN or greater	Hydraulic brake (cylinder dia. 33), hydraulic pressure 14 Mpa equiv.
Parking brake pressure	9.3 kN or greater	Pad $\mu=0.15$, slope capability: 20% equiv.
Actuator size	107×62×84.5	-30% compared to the conventional product (developed in 2011)(occupied volume)
Weight (excluding pad and mount)	2.8kg	-0.4 kg compared to the conventional product (developed in 2011)

Table 2 Specification of motor

Item	Specification
Type	DC brushless
Size	46×52
Supply voltage	12V
Maximum output	140W

2.2 Parking brake mechanism

Fig. 3 shows the schematic of the parking brake mechanism.

The parking brake mechanism consists of lock holes on the intermediate gear, a solenoid mounted in the motor housing, and a lock pin. The control flow of the parking brake is described as follows using Fig. 4:

<Control-flow of parking brake>

[(a) Operation]

- (1) The pressure is added to the specified value by the motor.
- (2) The solenoid is activated to advance the lock pin.

- (3) Power supply to the motor is stopped. The intermediate gear rotates to the direction to reduce the pressure due to the reaction force from the pad.
- (4) The lock pin and the lock hole are engaged and the rotation of the intermediate gear to the direction of pressure reduction is restricted. Power to the solenoid is switched off to end the operation.

[(b) Release]

- (1) The motor is driven to the direction to increase the pressure.
- (2) When friction applied to the lock pin is released, the intermediate gear and the lock pin are disengaged.
- (3) The lock pin is pulled back by the return spring in the solenoid.
- (4) The motor is driven corresponding to the operation of the brake pedal (end of release action).

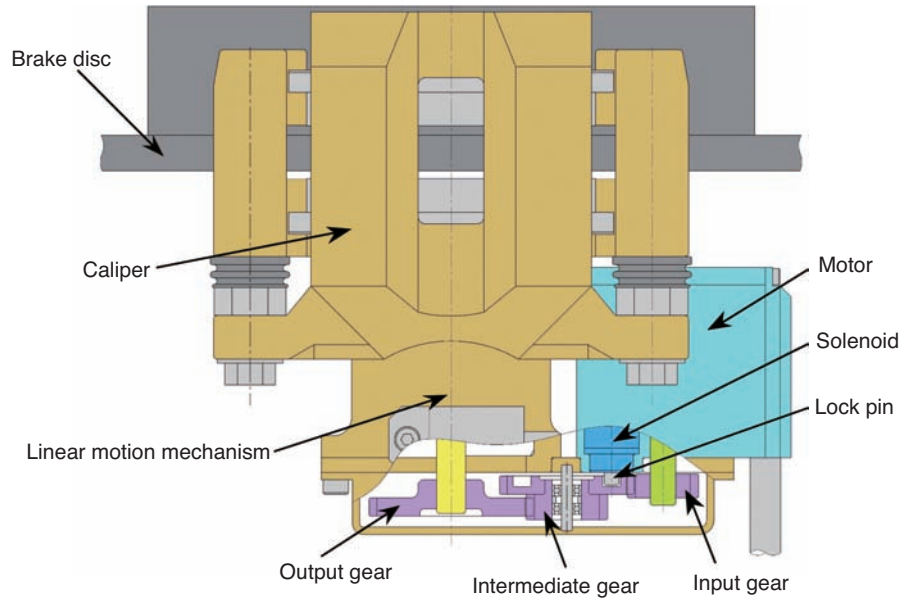


Fig. 3 Schematic of parking brake

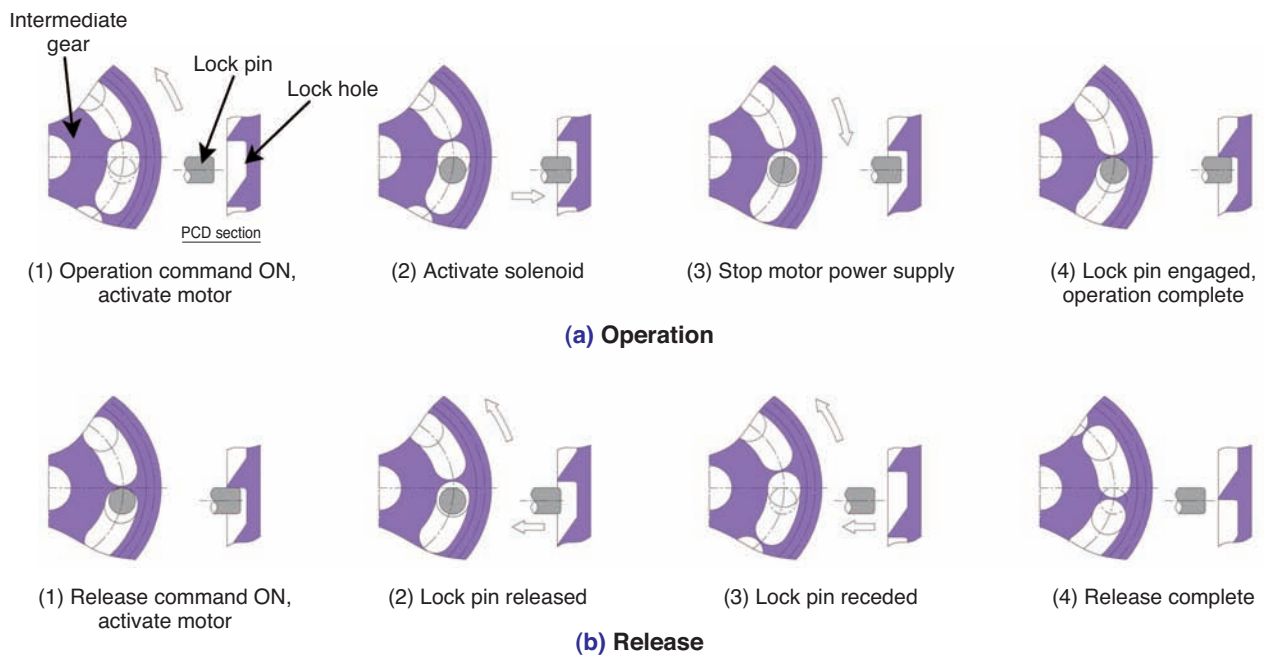


Fig. 4 Control-flow of parking brake

3. Response

The evaluation result of the response, which is one of the key characteristics of the unit, is described in the following. An inverter dedicated to the electro-mechanical brake unit was designed and built for conducting the evaluation and the pressure feedback control where the load is detected by the load sensor within the unit was configured.

3.1 Service brake

Fig. 5 shows an example of the evaluation results of response of the service brake. It shows how the actual pressure tracks the pressure command of the rectangular shape (0 kN↔12 kN). The initial clearance between the pad and disc is 0 mm. The result shows that the response is approximately 30% improved over the conventional products both for rise and drop of pressure.

3.2 Parking brake

Fig. 6 shows the change of pressure when the parking brake is operated (released) when the service brake pressure command is 0 kN (clearance: 0.1 mm).

To operate the parking brake the solenoid is activated to advance the lock pin while the pressure above a certain level is applied, as described in the previous section. In that state, the pressure is reduced and when the phases of a lock hole on the side of the intermediate gear and the lock pin match, the intermediate gear is locked (A in the figure). To release the parking brake, the pressure is raised by the motor first to release the friction applied to the lock pin (B in the figure) then the pressure is released. The operation completes within 0.3 seconds from the command both for operating and releasing the parking brake.

Similarly, it was confirmed that the operation completes within approximately 0.3 seconds when the service brake is operated (the brake pedal is pressed).

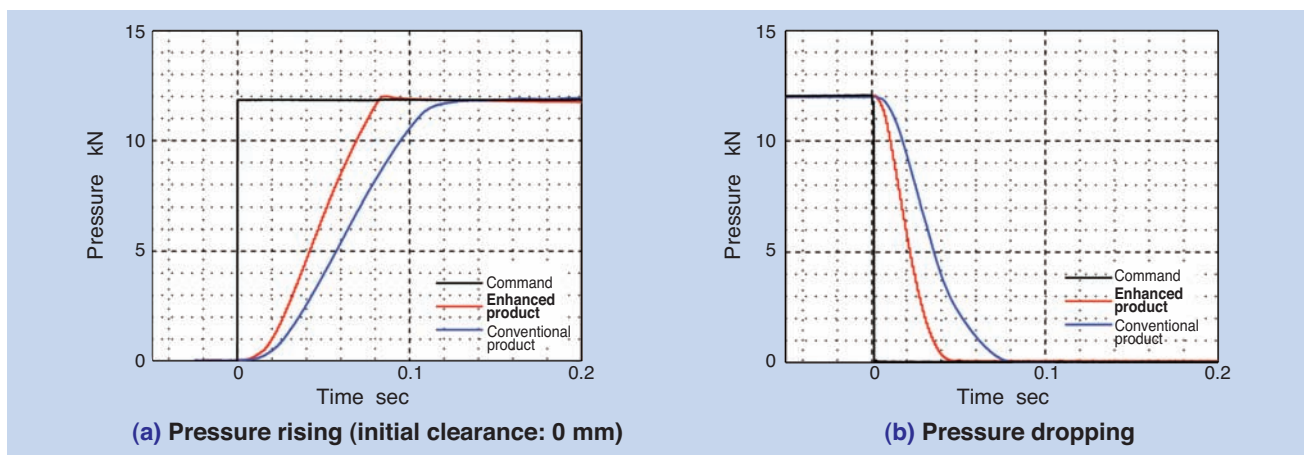


Fig. 5 Response of service brake

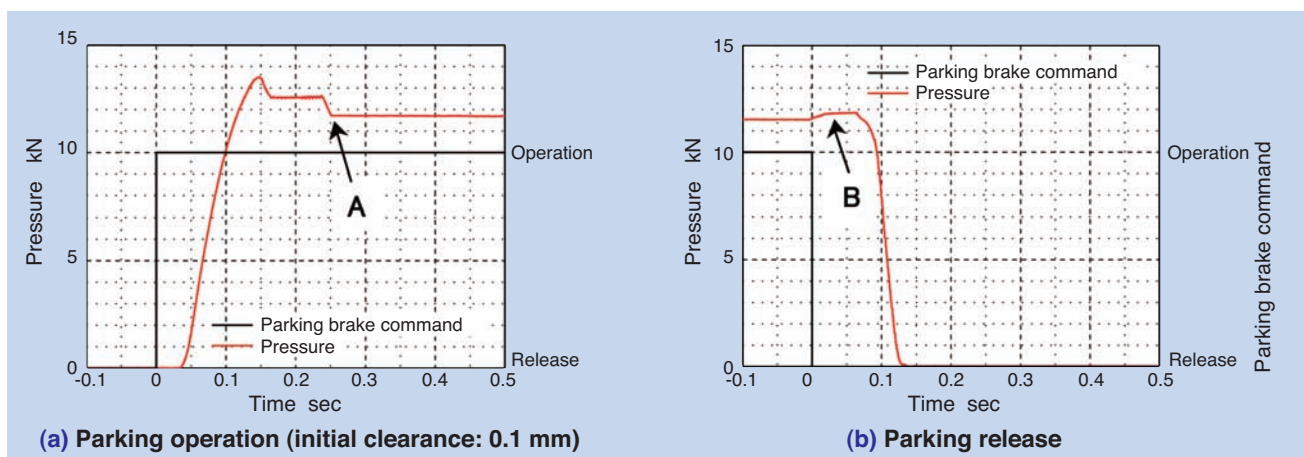


Fig. 6 Response of parking brake

4. Conclusion

In this article, we introduced a small electro-mechanical brake unit with a parking brake function which is applicable for rear wheels of 1500 cc class vehicles. This unit achieved a reduced size and enhanced performance compared to the conventional products by revisiting the internal design.

The enhanced performance of a brake is effective not only for fuel economy of the vehicles but also for the safety¹⁰⁾⁻¹³⁾; therefore, it is assumed that the demand for the electro-mechanical brake will be increased in the future. We will continue to develop an electro-mechanical brake, improving the unit and control technology for commercialization.

References

- 1) Yutaka Noguchi, Manabu Takegawa: Introduction of Electronic Parking Brake System, SUBARU Technical Review, No. 36 (2009) 70-72.
- 2) Takuya Obata, Yukio Ohtani, Yoshinori Itou, Shinnosuke Gotoh, Yuichi Koike: Development of Electrically-Driven Intelligent Brake Actuator with Regenerative Braking System, Proceedings of the Society of Automotive Engineers of Japan Annual Congress No. 20115172 (2011).
- 3) Naoto Okubo, Takashi Nishioka, Kohei Akamine, Kunimichi Hatano: Development of Electric Servo Brake System, HONDA R&D Technical Review, Vol. 25, No. 1 (2013) 47-51.
- 4) Yasushi Aoki, Kenji Suzuki, Hiroshi Nakano, Yoshikazu Nojiri: Development of Hydraulic Servo Brake System for Hybrid Vehicle, HONDA R&D Technical Review, Vol 18, No. 2 (2006) 60-66.
- 5) Christain von Albrichsfeld, Jurgen Karner : Brake System for Hybrid and Electric Vehicle, SAE Paper, 2009-01-1217(2009).
- 6) Yamasaki, Eguchi, Makino: Development of an Electromechanical Brake, NTN TECHNICAL REVIEW 75 (2007) 53-61.
- 7) Yamasaki, Eguchi, Makino: Actuator for Electromechanical Brake, NTN TECHNICAL REVIEW 77 (2009) 40-44.
- 8) Tatsuya Yamasaki : Linear Motion Actuator for Electromechanical Brake, World Tribology Congress 2009
- 9) Yamasaki: Development of Actuator for Electromechanical Brake, THE TRIBOLOGY, 285 (2011) 34-36.
- 10) Tomohiko Adachi: The Electronic Stability Control System, Journal of Society of Automotive Engineers of Japan, Vol. 60, No.12 (2006) 28-33.
- 11) Bo Cheng, Tadashi Hatano, Toshiya Hirose: Effects of Brake Assistance Systems in Emergency Situations, Proceedings of the Society of Automotive Engineers of Japan Annual Congress No. 20065894 (2006).
- 12) Yasuo Konshi, Masahito Hattori, Masakazu Sugisawa, Michiharu Nishii: Development of Hydraulic Brake Actuator for Active Brake Control, Proceedings of the Society of Automotive Engineers of Japan Annual Congress No. No.9739075 (1997).
- 13) Hirohisa Tanaka, Hiroyuki Kodama, Yoshiki Matsuzaki, Kaoru Tsubouchi: Innovative Technologies of Braking System and Components, Journal of Society of Automotive Engineers of Japan, Vol 59, No. 1 (2005) 69-74.

Photo of authors



Tatsuya YAMASAKI
Chassis System Engineering,
EV Module Business HQ



Makoto MURAMATSU
Chassis System Engineering,
EV Module Business HQ



Yui MASUDA
Control System Engineering,
EV Module Business HQ

Ball Screw Drive Module for Electric Hydraulic Brake

Hayato KAWAGUCHI*
Keisuke KAZUNO*



Recently, EV and Hybrid Vehicle percentage is getting higher at the automotive market main caused by the low fuel consumption requirement and CO₂ emission reduction requirement. Those vehicles have the regenerative braking system, in order to obtain the vehicle running range expansion and the highest electric efficiency. NTN have developed the compact lightweight ball screw drive module for regeneration cooperative brake system.

This report introduces the development result and the typical feature for it.

1. Introduction

The regenerative brake system used in hybrid and electric vehicles uses a motor for driving the vehicles as generators when the brake is applied in order to recover the kinetic energy as electrical energy. However, the braking force by the rotational resistance of the motor alone does not provide the necessary braking power intended by the driver, therefore, the shortfall indicated by the shaded area in Fig. 1 needs to be augmented by a hydraulic brake. In order to recover as much electric energy as possible, it is necessary to operate the regenerative brake to

the maximum extent; however, the regenerative brake and hydraulic brake must be used cooperatively to instantaneously respond to the demanded braking power that changes from time to time.

NTN has developed a high response, high thrust, compact and lightweight "ball screw drive module for an electric hydraulic brake" for a regeneration cooperative brake system which can instantaneously and arbitrarily control a hydraulic brake.

2. Configuration of electric hydraulic brake

The configuration of an electric hydraulic brake used for a regeneration cooperative brake system is shown in Fig. 2. The mechanism to apply hydraulic pressure to the caliper of each wheel is as follows:

When a driver presses the brake pedal, the amount of pressure applied to the pedal is transmitted to ECU. From this signal and the vehicle's traveling information such as the vehicle speed, ECU calculates the hydraulic pressure required for producing the supplementary braking force by considering the braking force required by the driver and producible regenerative brake force. ECU drives the DC motor based on this calculation result. The ball screw drive module is operated by the DC motor pressing the piston in the hydraulic cylinder to produce an

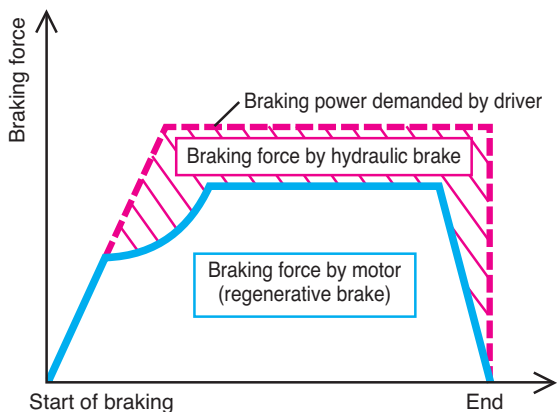


Fig. 1 Regenerative brake system

*Chassis Engineering, Automotive Business HQ

appropriate pressure and the braking force is created by each wheel caliper.

Adoption of the ball screw drive module realizes precise control that responds to the demanded action enabling recovery of additional energy even in the area of low recovery efficiency such as the start and end of the braking action.

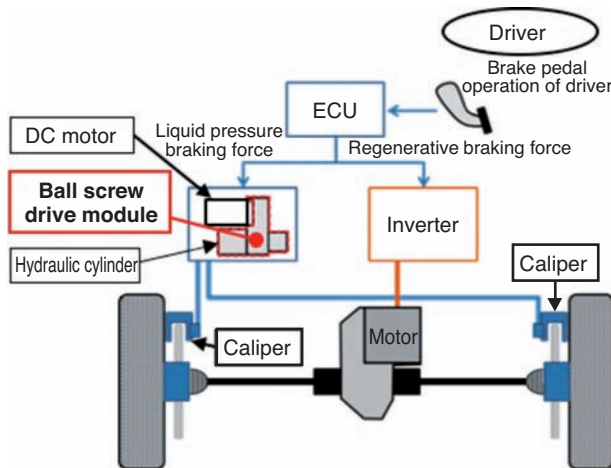


Fig. 2 Constitution of electric hydraulic brake

3. Benefits of ball screw drive module

3.1 Compact, lightweight and simple design

The ball screw drive module is designed for compactness and lightweight with a simple structure that uses few components as shown in Fig. 3.

The rotational torque of the DC motor is transmitted to the ball screw nut through the gear train for the reducer for linear motion of the ball screw shaft.

The key components include a ball screw, supporting bearings, sleeve as the rotation stopper, gear train as reducer which transmits the rotational torque from the motor, and aluminum case housing.

The ball screw drive module is a module product that brought together not only the ball screw and the supporting bearings, which are the key components for converting the rotational torque of the DC motor to axial thrust power, but also many of the NTN's proprietary technologies such as sintered materials.

The following is the description of the detailed structure of the components:

Fig. 4 shows the details of the idler gear structure for the reducer. The idler gear unit is inserted to the supporting shaft with washers on both sides. Shell-shape needle bearings are press fit inside the idle gear to reduce the friction loss.

The joint of the aluminum case is sealed with a liquid gasket. The adoption of a liquid gasket that

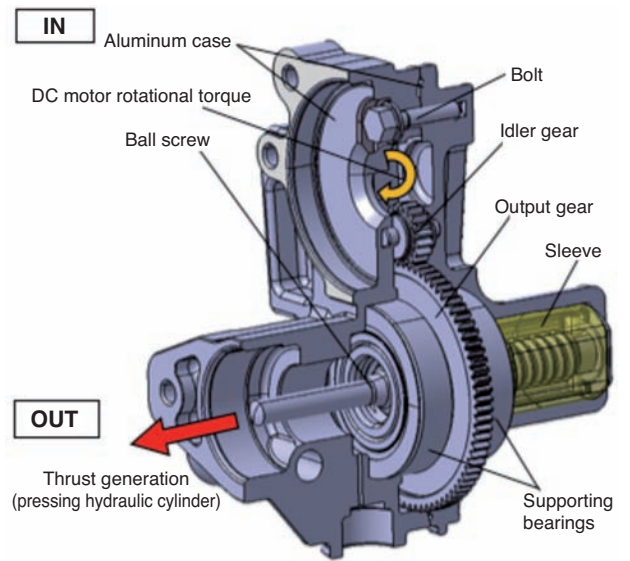


Fig. 3 Cross section structure of ball screw drive module

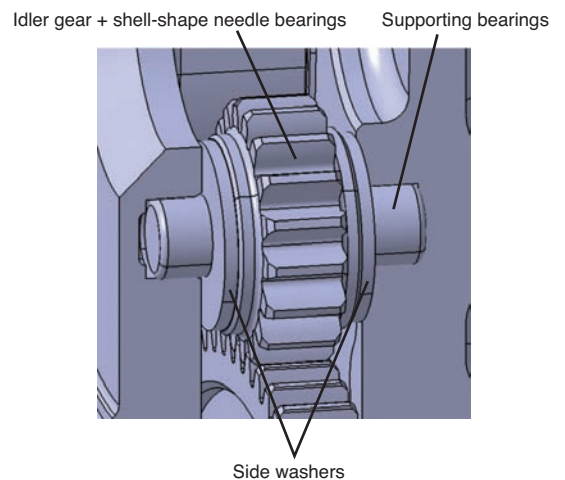


Fig. 4 Idle gear structure

forms an elastic and adhesive film enabled followability to elastic deformation of the joint, as well as a high level of airtightness.

3.2 Long-life, high-strength and environment-resistant specification

(1) Long life and high-thrust power of ball screws

For long-life ball screws, the load capacity can be improved by increasing the shaft diameter, ball size and number of balls. On the other hand, the smaller the lead the more thrust power when the rotational torque is converted to the axial thrust power by the ball screws. However, if larger balls are used in excess of the size of the lead in the ball screw of normal design, the balls of adjacent leads make contact to each other jeopardizing the ball screw function.

We developed a long-life ball screw that allows ball size in excess of the lead by taking note of the fact that the “balls are withdrawn to the deflector before going on one circle” which is the characteristic of the deflector type circulation and adopted it in this module.

Fig. 5 shows the schematic of products of conventional design and long-life design.

Table 1 shows the specification comparison between the ball screws of conventional design and long-life design. By introducing larger balls and optimizing the groove specification, we have successfully developed compact, long-life, and high-thrust power ball screws of double load capacity compared to the conventional products without increasing the nut length, outer diameter or leads.

In order to verify the durability, we conducted ball screw shaft linear motion tests under specified loads at a low temperature of -30°C to a high temperature of 110°C.

After these tests, we conducted performance verification and disassembly inspection of the ball screw drive module and the result indicated no significant changes in efficiency, airtightness, etc. satisfying the set functions. No anomalies were found in all the components including the ball screw and gears thus showing sufficient durability.

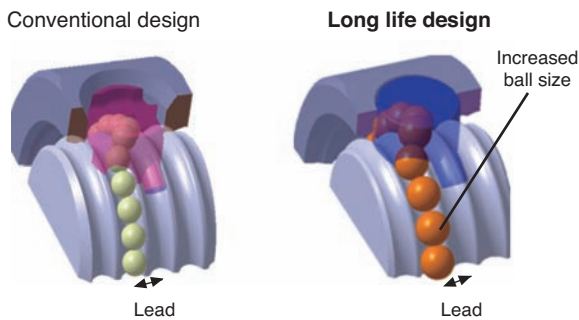


Fig. 5 Schematic of long life ball screw

Table 1 Ball screw specifications comparison

Specification	Conventional design	Long life design
Shaft diameter (mm)	16	
Lead (mm)	4	
Ball diameter (/conventional design)	1	1.33
Dynamic load rating C_a (/conventional design)	1	2.06
Static load rating C_{0a} (/conventional design)	1	2.06

(2) High-strength aluminum case

Aluminum die cast is adopted for the case of the ball screw drive module. The benefits of die cast manufacturing include the ability to cast a thin and precisely sized plate, superior mass productivity with short cycle time, as well as high material strength due to refined structure and formation of a chill layer (layer with high internal density) on the surface by rapid solidification.

The strength of the aluminum case of the ball screw drive module was verified through FEM analysis in advance and the maximum stress on the most vulnerable part of the aluminum case was confirmed before selecting the optimum thickness to secure a sufficient safety factor.

(3) Environment resistance

The ball screw drive modules are used in the brake system, which is one of the key vehicle components, and therefore performance is required to be maintained for a long time under diverse environments. As it is exposed outside the body, the environment resistance was evaluated under high temperature, high humidity, and salt spray tests.

After the tests, we conducted performance verification and disassembly inspection of the ball screw drive module and the results from all the tests indicated no significant deterioration or change in size that would cause any issues in the function, thus showing sufficient environment resistance.

Fig. 6 shows the case joint area after a cyclic corrosion (salt spray) test. We verified that there was no corrosion inside the aluminum case seal in the salt spray test.

We also verified that there was no water immersion inside the aluminum case seal after submerging the ball screw drive module in high temperature water, during the high-temperature submergence test.

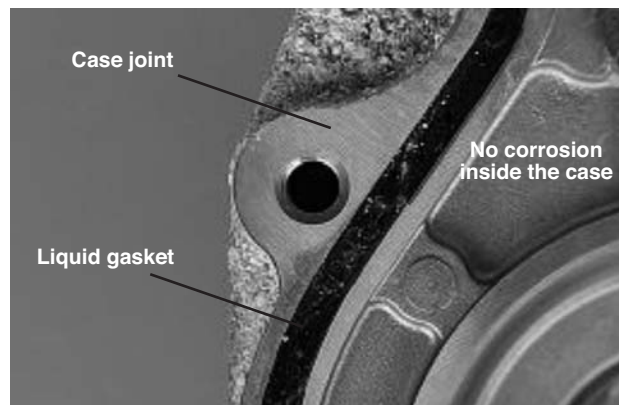


Fig. 6 Aluminum case after cyclic corrosion test

4. Conclusion

In this article, we introduced the ball screw drive module adopted in the electric hydraulic brake.

The market for the compact and light-weight ball screw drive module is expected to grow as vehicles adopt more "by-wire" control and electric power.

NTN succeeded in the application of module products consisting of mainly ball screws into key vehicle components by this development.

We strive to continue development and enhancement of not only the ball screw technology but also technology of peripheral components such as cases, reducers, and motors in order to achieve light weight and improved functionality of module products.

References

- 1) Kazuno, et al.: Ball-screw Unit for Variable Valve Event and Lift System, NTN TECHNICAL REVIEW No. 75 (2007) 72-77.
- 2) Japan Aluminium Association, Aluminum Handbook (7th Edition)

Photo of authors

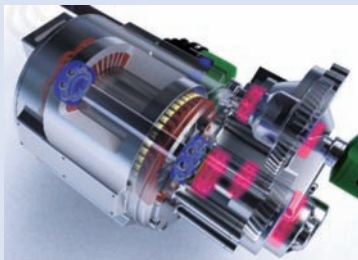


Hayato KAWAGUCHI
Chassis Engineering,
Automotive Business HQ



Keisuke KAZUNO
Chassis Engineering,
Automotive Business HQ

Low Torque Deep Groove Ball Bearings for EV and HEV



Tsuyoshi KODA*
Takahiro WAKUDA**
Tomohisa UOZUMI***

In order to improve mileage per charge, various approaches for EV and HEV parts to achieve low electricity consumption, weight reduction, and downsizing are attempted. And also, for bearings to be utilized in EV motors, further low torque performance is a strong demand. This paper introduces High Speed and Low Torque Deep Groove Ball Bearing for EV/HEV as Oil Lubrication Type and Low Torque Sealed Ball Bearing as Grease Lubrication Type from NTN, and explains its features and performances.

1. Preface

In EV/HEV motors, two types of ball bearings, namely, transmission oil lubricated and grease lubricated, are used. The oil lubricated type is used in high speed applications for small motors. On the other hand, the grease lubricated type tends to be used in relatively low speed applications for larger motors.

Two types of bearings have been developed to contribute to low power consumption of motors, namely, high speed/low torque, oil lubricated, deep groove bearings and low torque, grease lubricated, sealed deep groove ball bearings; the following article introduces them.

2. High speed low torque deep groove ball bearings (oil lubrication)

2.1 Concept

In order to reduce electric power consumption of EV/HEV, it is required to reduce the size and weight of motors. However, simple reduction of size would cause a shortage of output torque of the motor, which needs to be supplemented by high speed rotation. Under this high rotational speed condition, the bearings are required to operate with $d_{m\Omega}$ value*1 of approximately 1.6×10^6 . However, the $d_{m\Omega}$ value of the

existing bearings used for ordinary vehicles is approximately 0.5×10^6 and any operation at higher $d_{m\Omega}$ conditions would cause problems such as heating up or deformation of cage, etc.

The developed product achieves low torque operation by optimization of internal specifications and implementation of a newly developed cage. It can be used under high $d_{m\Omega}$ conditions due to enhanced cage strength.

*1 Product of the diameter of bearing rolling element pitch circle and rotational speed

2.2 Benefits of developed product

Table 1 shows a comparison of the conventional product and developed product. The newly developed “combined type resin cage” is a cage that is made of two pieces of the same shape combined together as shown in **Fig. 1**.

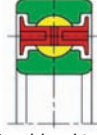
Under conditions in excess of $0.5 \times 10^6 d_{m\Omega}$, a standard cage may deform by the centrifugal force and make contact with the outer ring or rolling element and/or be damaged by heat at the raceway. With this developed product, heating has been reduced by optimizing internal specifications of the deep groove ball bearings, as well as implementation of a “combined type resin cage” which has little deformation by centrifugal force. In addition,

*Powertrain Engineering, Automotive Business HQ

**Drivetrain Engineering, Automotive Business HQ

***Drive System Engineering, EV Module Business HQ

Table 1 Comparison between ordinary and developed

	Conventional product	Developed product
Material of bearings	SUJ2	SUJ2
Material of cage	SPCC, PA66	PA66
Structure of cage	 Steel plate  Cantilever resin	 Combined type resin

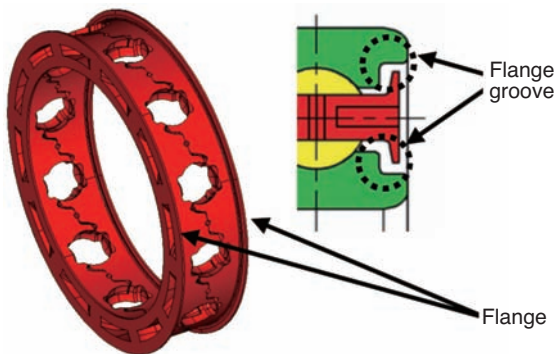


Fig. 1 Feature of combined type resin cage

temperature rise of the bearings in high speed rotation has been lowered by reducing the oil inflow and stirring resistance with the flanges on the cage sides and the flange grooves of inner/outer rings.

2.3 Performance of developed product

1) Rotational torque

Table 2 shows the measurement conditions and **Fig. 2** shows the measurement results.

The developed product shows at least 50% lower torque compared to the conventional products at a rotational speed of 3,000 min⁻¹ or more.

Table 2 Torque measurement conditions

Bearing size	Upgraded rated load based on 6909
Cage specification	Conventional corrugated iron plate cage
	Conventional cantilever resin cage
	Developed combined type resin cage
Rotational speed	Max. 6,000 min ⁻¹
Load	Radial 100N
Temperature	40°C
Lubrication	ATF
Oil level	Lowest rolling element pitch circle diameter

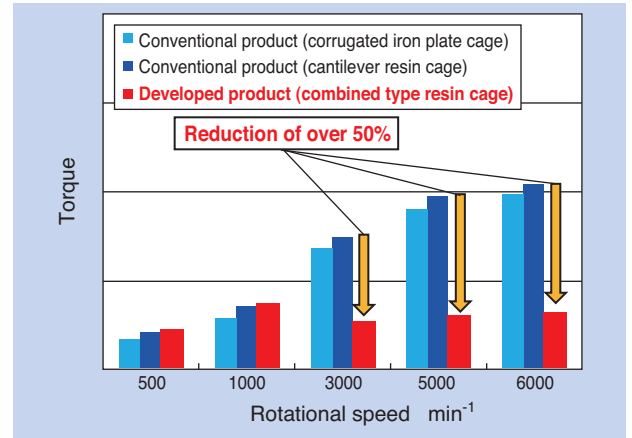


Fig. 2 Torque measurement results

2) Durability

Table 3 shows the test conditions. When the developed product was operated at 1.6×10⁶ d_mn for 1,000 hours, it did not show any seizure or damage of the cage. **Fig. 3** shows the appearance of the bearing components after the test. The developed product showed no signs of damage, such as peeling and flaking, on the raceway of the inner/outer rings or rolling elements

Table 3 Durability test conditions

Bearing size	6008
Cage specification	Developed combined type resin cage
Lubrication	ATF
Rotational speed	30,000 min ⁻¹
Load	Radial 1,000N
Operation time	1,000h

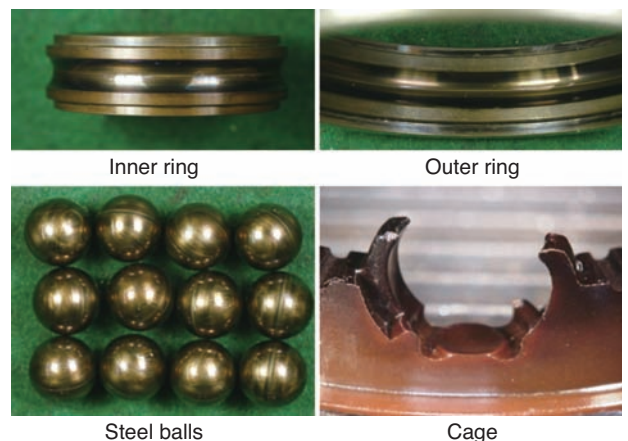


Fig. 3 Sample after durability testing

3) Strength of cage

Fig. 4 shows the analysis result of the stress produced on the cage by the centrifugal force under a d_{min} value of 1.6×10^6 . The stress on the cage of the developed product was verified to be under the material fatigue limit, exhibiting no problems. In addition, the radial deformation was shown to be 1% or less, a sufficiently small value.

One of the causes of the cage damage is stress due to advance/delay of the rolling elements. The strength of the cage has been verified by forcing advance/delay of the rolling elements. This was achieved by applying a moment with no lubrication.

Table 4 shows the test conditions and Fig. 5 shows the test results under these conditions. The conventional product broke at the pocket area in a short time, however, the developed product continued under the same condition, indicating superiority in strength compared to the conventional products.

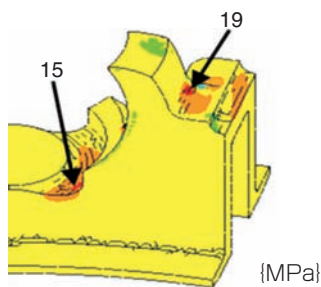


Fig. 4 Cage centrifugal force analysis results

Table 4 Cage strength test condition

Bearing size	6008
Cage specification	Conventional cantilever resin cage
	Developed combined type resin cage
Lubrication	No lubrication
Rotational speed	$4,000 \text{ min}^{-1}$
Moment	$19.6 \text{ N} \cdot \text{m}$

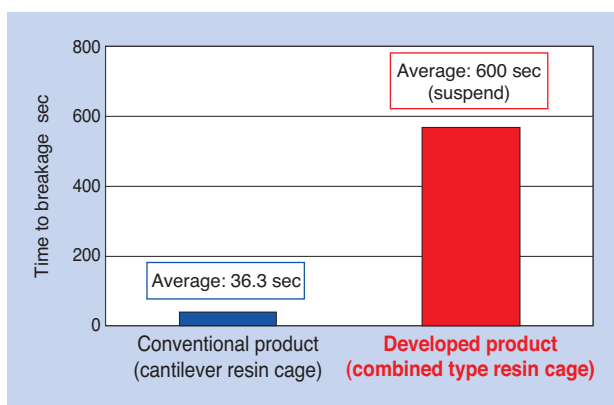


Fig. 5 Cage strength test results

3. Low torque sealed deep groove ball bearings (grease lubrication)

3.1 Concept

There are 6 torque factors in grease-sealed deep groove ball bearings as shown in Fig. 6. Factors (1), (2), (5) and (6) are determined by the internal specifications of the bearings and can be obtained by calculation.

The stirring torque due to grease viscosity, factor (3), is significantly affected by the grease properties. In addition, the shear torque of the grease between the cage and rolling elements, factor (4), is affected by the configuration of the cage. For the developed bearings, focus was given to factors (3) and (4) to lower the torque by improving the grease properties and the cage configuration.

- (1) Rolling viscosity torque on the raceway
- (2) Elastic deformation torque of the rolling element
- (3) Stirring torque due to the grease viscosity
- (4) Shear torque of grease between the cage and rolling element
- (5) Torque due to the differential slip between the rolling element and raceway rings
- (6) Torque due to the spin slip between the rolling element and raceway rings

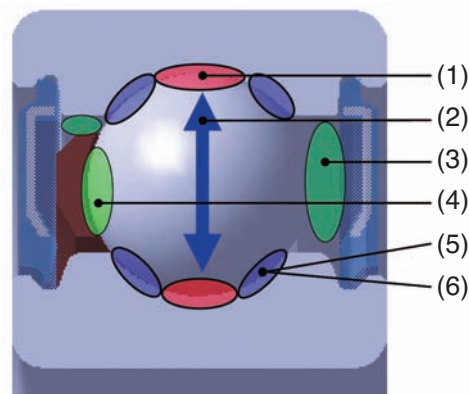


Fig. 6 Torque factors

3.2 Features

1) Adoption of newly developed grease

The newly developed grease for reducing the “stirring torque due to the grease viscosity”, factor (3), consists of a refined thickener and a base oil of low viscosity. Table 5 shows the grease properties. As shown in Fig. 7, the ability of the thickener to hold the base oil was improved by refining the thickener structure; this allowed reduction of the thickener content and consequently, the resistance of thickener. The resistance of the base oil was reduced by

adoption of low-viscosity base oil. Both these measures aided in reducing grease stirring of the bearing rolling elements.

Table 5 Grease property table

		Conventional product	Developed product
Thickener		Urea based	Urea based
Base oil		Synthetic oil	Synthetic oil
Base oil viscosity mm ² /s	40°C	40.6	33.4
	100°C	7.1	5.8
Consistency		243	280
Low temperature torque -40°C mNm	Starting	350	250
	Rotating	80	70

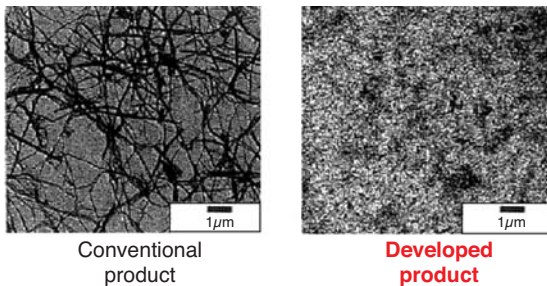


Fig. 7 Thickener structure

2) Adoption of newly developed cage

In order to reduce “shear torque of grease between the cage and rolling element”, factor (4), it is important to supply the minimum oil quantity without allowing excessive grease inflow between the cage and rolling element.

For the developed cage, a grease scraping mechanism was added to the outer diameter of the cage pocket as shown in Fig. 8, to prevent excessive grease inflow, and achieve lower torque.

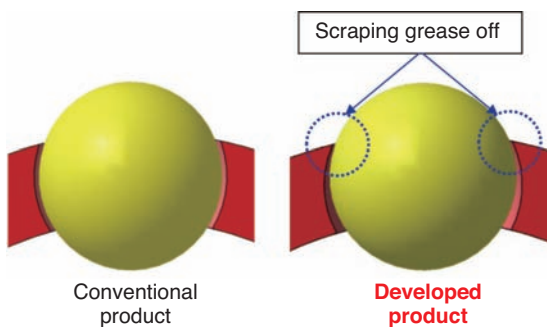


Fig. 8 Comparison between conventional and developed products

3.3 Performance of developed product

1) Rotational torque

Fig. 10 shows the torque measurement result with the measurement equipment and test conditions in Fig. 9. It has been shown that the developed product has at least 50% lower torque compared to the conventional products.

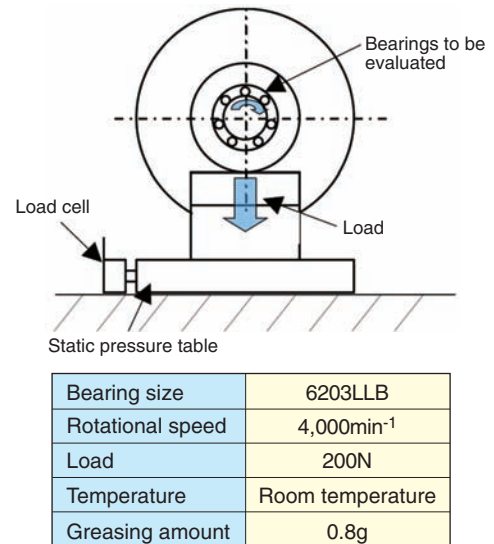


Fig. 9 Torque measurement equipment and conditions

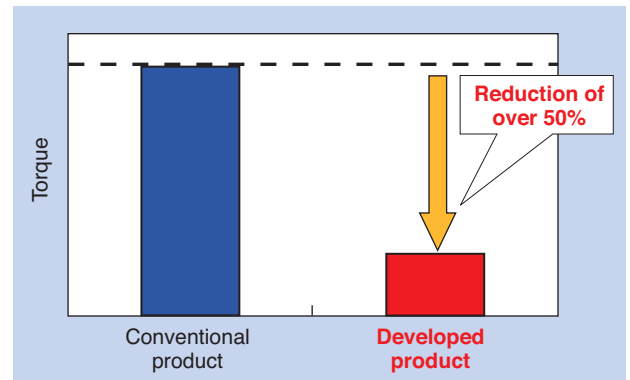
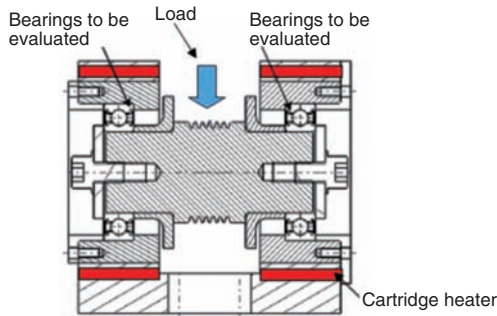


Fig. 10 Torque comparison results

2) Grease life

Fig. 12 shows the result of evaluation for grease life with the measurement equipment and test conditions in Fig. 11. The developed product showed approximately three times life when compared to the conventional products.



Bearing size	6204LLB
Rotational speed	10,000min ⁻¹
Load	2,000N
Temperature	150°C
Greasing amount	1.0g

Fig. 11 Grease life evaluation tester and conditions

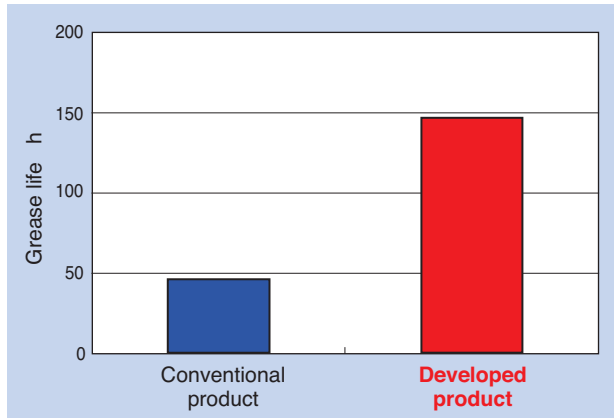


Fig. 12 Grease life evaluation test results

3) Strength of cage

Fig. 13 shows the analysis result of the stress applied to the cage by the centrifugal force. This stress is equivalent to the stress seen in the conventional product, which does not exhibit any problems.

Cage strength has been verified by forcing advance/delay of the rolling elements by applying moment to the bearings. To maximize the stress on the cage, the cage pocket clearance was set to the lower limit. Fig. 14 shows the moment load tester and test conditions and Fig. 15 shows the strength test results.

It has been verified that there is no problem with the cage durability of the developed product.

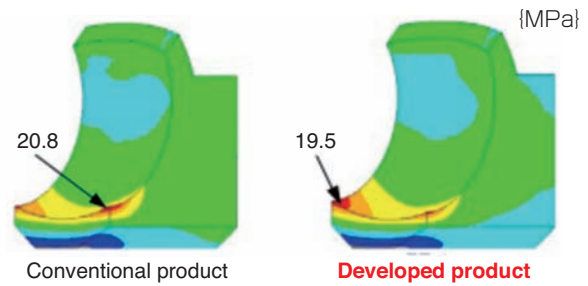
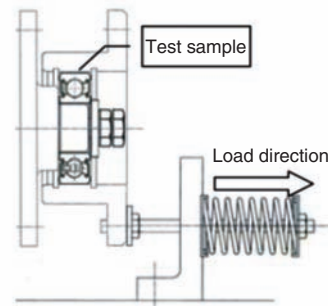


Fig. 13 Cage centrifugal force analysis results



Cage specification	Developed cage with the lowest pocket clearance
Grease type	Developed grease
Rotational speed	5,000min ⁻¹
Moment	11.8N · m
Test time	89 h (loading times: 1×10 ⁷)

Fig. 14 Moment load tester and conditions



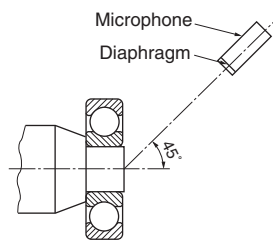
No anomalies such as breakage and cracks are observed

Fig. 15 Moment load test results

4) Acoustic property

As the drive power changes from engine to motor, the requirement for noise reduction of the bearings will also become more vital. The developed bearings have improved acoustic properties compared to the conventional bearings. This has been achieved by refining the thickener structure of the grease. Fig. 16 shows the acoustic tester and test conditions and Fig. 17 shows the acoustic test results.

It has been shown that the developed product is superior in reducing noise as compared to the conventional bearings.



Bearing size	6203LLB
Rotational speed	1,800min ⁻¹
Axial load	20N
Temperature	Room temperature

Complied with JIS B 1548

Fig. 16 Acoustic test conditions

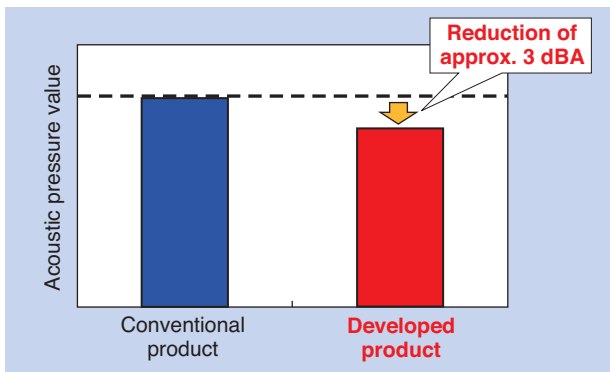


Fig. 17 Acoustic test results

4. Summary

The developed product introduced in this article has the characteristics as shown below. The developed products will be promoted to contribute to compact and power-efficient EV/HEV motors which are expected to expand in the market.

[Low torque deep groove ball bearings for EV and HEV]

High speed rotation

Can be used under conditions with a d_{mN} value of 1.6×10^6

[In case the bearing pitch diameter is 54.0 mm, rotational speed of 30,000 min⁻¹]

Running torque

Over 50% reduction compared to conventional products

[Low torque sealed deep groove ball bearings]

Running torque

Over 50% reduction compared to conventional products

Acoustic

Equivalent or better than our conventional products

Life

Equivalent or better than our conventional products

References

- 1) Proceedings of the Japan Society for Precision Engineering Autumn Meeting in 2001, Agitation torque that occurs with bath lubrication of rolling bearings (report 1 and 2)
- 2) Japanese Society of Tribologists, Tribology Handbook, Yokendo, 2001, 173

Photo of authors



Tsuyoshi KODA
Powertrain Engineering
Automotive Business HQ



Takahiro WAKUDA
Drivetrain Engineering
Automotive Business HQ



Tomohisa UOZUMI
Drive System Engineering
EV Module Business HQ

The Reactor Core for HEV Boost Converter

Takayuki ODA*
 Shinji MIYAZAKI*
 Eiichirou SHIMAZU**



Nippon Kagaku Yakin Co.,Ltd., as one of the NTN group companies, develops various types of magnetic material products¹⁾. The major product is the Amorphous core which has characteristics of high saturation magnetic flux-density, low core loss and superior frequency characteristics.

This article introduces the Amorphous reactor core to meet high current and compact for Hybrid electric vehicle.

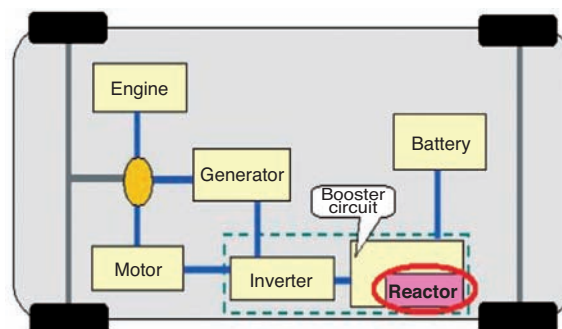
1. Introduction

Vehicles are equipped with batteries and many electric parts which require their respective suitable voltages. Therefore, DC-DC converters are used to convert DC voltages²⁾. Reactors in the DC-DC converters are electromagnetic components used to convert electric energy to magnetic energy and store/release it in the switching circuits. They also provide voltage boosting/dropping and current smoothing. Fig. 1 shows the key power control components in hybrid vehicles (HEVs) and a typical reactor configuration used in the booster circuit.

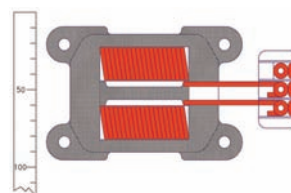
As the DC-DC converters for HEVs supply power to the drive motor, which requires a large output, reactor cores are required to support large current of several tens to hundreds of amperes. In addition, demand for compact reactors is strong since they are mounted onto vehicles. Since higher switching frequency is effective for achieving more compact reactors, it is necessary to address this technology.

Nippon Kagaku Yakin Co., Ltd., as one of the NTN group companies, develops core materials mainly using amorphous alloys to address these challenges. These materials provide more compact reactors compared to widely used ferrite materials. It is also possible to reduce iron loss compared to the Fe-Si based alloy materials.

In this article, we are introducing the amorphous alloy-based cores with high saturation magnetic flux-density, low iron loss, and superior frequency characteristics.



a) Reactor application in electric vehicle



b) Reactor configuration

Fig. 1 The reactor for booster circuit

*Engineering, Nippon Kagaku Yakin Co., Ltd.

**Advanced Technology R&D Center

2. Types and characteristics of amorphous alloy cores

2.1 Types and characteristics of the developed core materials

While an amorphous alloy has excellent magnetic properties, mass production is difficult due to its extreme hardness. Mass production also causes wear on the mold during compression or injection molding and a high burden on the facilities. We have solved this difficult problem by developing our own materials and proprietary manufacturing technologies. These include improving the binder composition blended in the amorphous alloy powders, improving manufacturing facilities and mold structures, optimizing molding conditions, and many more.

Fig. 2 shows typical examples of cores developed by Nippon Kagaku Yakin Co., Ltd.

Two types of materials, “AL60” for compression molding and “AS10” for injection molding, were newly developed. Both materials exhibit a good frequency response by maintaining the magnetic properties up to the higher frequencies. AL60 has a high relative permeability and small iron loss. On the other hand, AS10 has a lower relative permeability and the inductance drop on high current is smaller. AS10 also has a higher degree of freedom for design since it uses injection molding. Inductance is the capability of a coil to generate flux from current. It is important for coils, such as reactors, to maintain their magnitude regardless of the current values.

By taking advantage of these properties, Nippon Kagaku Yakin Co., Ltd. is designing and proposing cores using either type of material or combining both materials to create composite cores. These designs are selected based on the specifications such as the current values and sizes required by customers.

2.2 Properties of amorphous alloys

Fig. 3 shows a SEM photograph of amorphous alloy powders. An amorphous alloy is a non-crystalline metal with a disordered atomic structure. This is produced by rapid cooling of over 1,000,000 °C/sec from a melted state. Since the alloy does not have crystalline structure, it shows the following properties ³⁾:

- **Isotropic physical property**
- **No heterogeneous property such as a crystal grain boundary, twin crystal, lamination defect, or dislocation in the structure**
- **Unlikely to deform because of the no slip plane of crystal**

Based on these properties, an amorphous alloy is a

superior soft magnetic material because of its high permeability and low iron loss. Unlike ordinary soft magnetic materials, amorphous alloys have a coercive force since there is no crystal grain boundary which prevents movement of the magnetic domain wall and has no magnetic anisotropy. It is also extremely hard and resistant to corrosion.

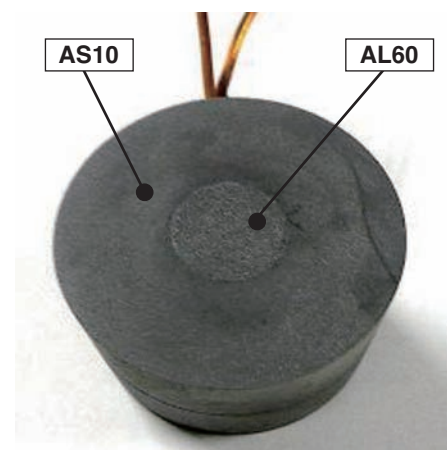
Table 1 shows comparison of properties with other magnetic materials.



a) Compression molding core AL60



b) Injection molding core AS10



c) Composite core (AL60+AS10)

Fig. 2 Core of various processes

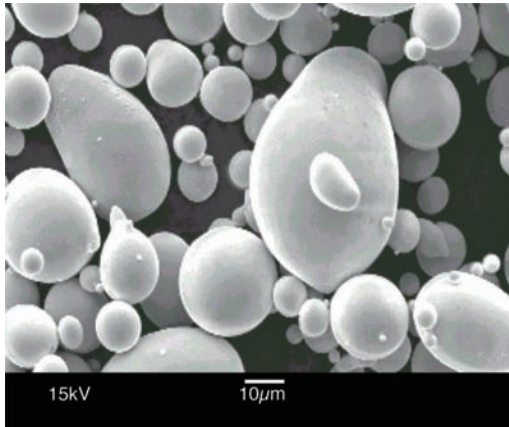


Fig. 3 Amorphous magnetic powder

Table 1 Comparison of material characteristics 4), 5)

	Amorphous alloy	Fe-Si alloy	Ferrite
Permeability	○	○	○
Magnetic flux density	○	○	×
Iron loss	○	△	○
Coercive force	○	△	○
Workability	×	△	△
Wear resistance	○	×	△
Corrosion resistance	○	×	○

○ : Superior △ : Slightly inferior × : Inferior

3. Developed technologies

3.1 Material technology

Amorphous alloys start crystallizing when heated to around 500°C and start losing the optimal properties of amorphous materials. To prevent this, the binder used as the compression molding material needs to have hardening property at low calcination temperature after being molded.

It also needs to withstand the annealing process at around 450°C which is applied for magnetic property enhancement after molding and calcination.

Thermosetting resin, used as a binder for bond magnets, hardens at low temperatures. However, a relatively high amount of the resin content is required to secure the product strength. This reduces the filling ratio of magnetic particles making it difficult to maintain a high magnetic property required for reactor cores of HEVs. Also, the low heat tolerance of the binder content prevents the annealing process.

Therefore, we developed a proprietary binder material for AL60 that enables molding and calcination at low temperatures with a small quantity of binder mix. It also allows the annealing process to take place at 450°C.

On the other hand, AS10 for injection molding uses polyphenylenesulfide (PPS) which has excellent heat resistance as a base material. When it is used with large current, such as in the reactor application for HEVs, the coil and core will be significantly heated. By using PPS as the base material, they can withstand up to 200°C. Typically when the mold is highly filled with magnetic particles, the fluidity of the material during molding is reduced resulting in unstable filling of the mold. However, with AS10, both high filling and high fluidity are achieved by optimizing the grain size and shape of the amorphous alloy powders and additive during kneading.

3.2 Manufacturing technology

Vickers hardness of an amorphous alloy is over 1,000, which is approximately 10 times harder than a ferrite material.

With compression molding, the method used for manufacturing AL60 cores, the material powders are filled in the mold, compressed, and calcinated. Compression molding of ordinary metal particles requires pressure of approximately 500 MPa. Amorphous alloy particles require a significantly higher pressure of approximately 2,000 MPa since the alloy is extremely hard and lacks a plastic deformation property. Therefore, slight misalignment or inclination in molding components and/or the press machine may generate extremely high partial pressure. This causes early wear of the mold or a large load on the auxiliary facilities. We have established ultra-high pressure molding technology improving precision of the press machine by providing a linear guide and achieving a high precision of 1/1000 mm for the mold.

The injection molding method for cores made of AS10 is required to provide measures against wear of the kneading machine, molding machine, and mold. This is necessary since hard amorphous alloy powders act as abrasives during kneading, pelletizing, and injection molding. We have established mass production technology by optimizing the component materials, surface treatment, mold structure, and molding conditions.

4. Performance of developed core

4.1 Large current characteristics

Ferrite cores consisting of iron oxide are generally used for reactors in low power output equipment that produce less than several hundred watts of output. The ferrite cores have extremely high relative permeability of several thousands, compared to amorphous cores with several tens. They also have low saturation magnetic flux density.

In a large current application such as a DC-DC converter for HEVs, the magnetic energy becomes large and the flux through the cores tends to magnetically saturate. At magnetic saturation, inductance of the coil suddenly drops and it is difficult to maintain the properties of the reactor. Therefore, in order to prevent magnetic saturation of ferrite cores with low saturation magnetic flux density, it is necessary to increase the cross sectional area to reduce generated flux density. This is not suitable for vehicle components which are required to be more compact.

Fig. 4 shows the relation between flux density and magnetic field intensity of the AL60 and AS10 amorphous alloy cores, an ordinary ferrite core, and a Fe-Si based compression molding core.

It shows that the ferrite core and the Fe-Si based compression molding core have a steep slope. The ferrite core also saturates at a small field intensity and the flux density does not increase. Since the AL60 compression molding core and AS10 injection molding core do not saturate, they can be applied to DC-DC converters for HEVs, which require a large current.

The change rate of inductance over the change of DC current, called the DC superimposition characteristic, is small with the amorphous cores. As shown in Fig. 5, inductance of the ferrite cores drops around 80% at 50A. However, inductance of AS10 only drops around 10%, even at 100A, showing an excellent DC superimposition characteristic.

4.2 High frequency properties

Reactors for HEVs are required to support large current and high switching frequencies within a small size requirement.

Fig. 6 shows the relation between the frequency and the inductance change rate for different cores. The inductance drops at several kHz with the ferrite core and several hundred kHz with the Fe-Si based compression molding core. On the other hand, the inductance of the developed amorphous cores stayed constant, even in the high frequency range up to around 1000 kHz.

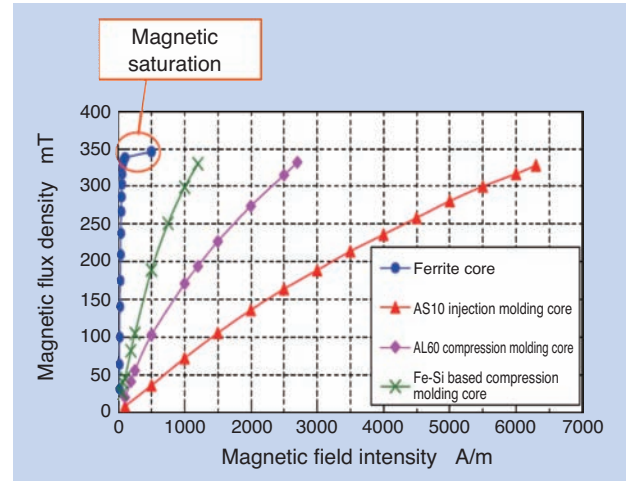


Fig. 4 B-H characteristics

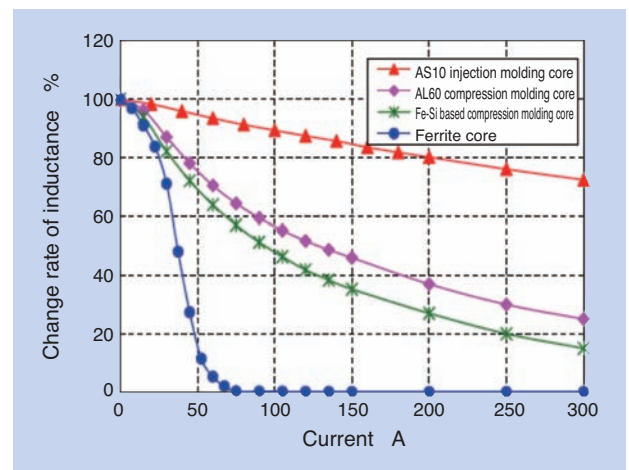


Fig. 5 DC superimposition characteristics

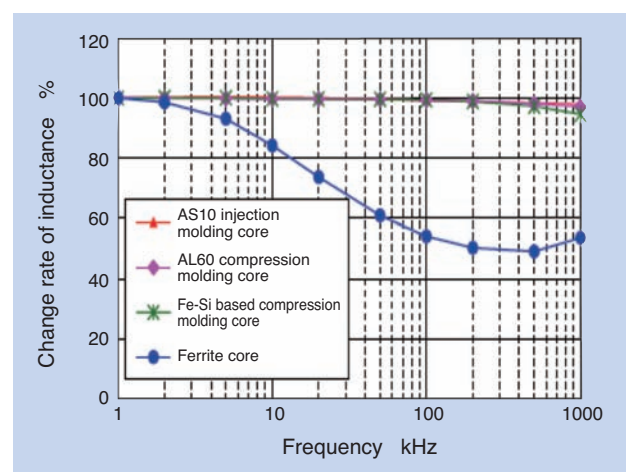


Fig. 6 Frequency characteristics

In the large current applications, Fe-Si based compression molding cores are frequently adopted, which have a large saturation magnetic flux density. However, Fe-Si based compression molding cores have relatively larger iron loss compared to ferrite cores (Fig. 7). The amorphous alloy of Nippon Kagaku Yakin Co., Ltd. has reduced iron loss equivalent to the ferrite cores by applying a special insulation coating treatment.

As stated above, the developed AL60 and AS10 amorphous alloy cores are capable of responding to the demand of large current and high frequencies with small volume. They have a high saturation magnetic flux density, excellent frequency properties, low iron loss, and DC superimposition characteristics.

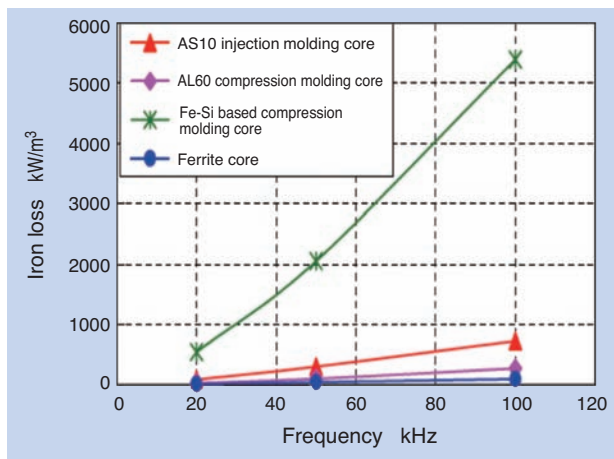


Fig. 7 Iron loss characteristics (50mT)

5. Optimization design by simulation

For restricted size and high power output of the reactor core, it is necessary to increase the drive frequency. The AC resistance of the coil and iron loss of the core increase as the frequency increases. Therefore, the design needs to consider radiation of heat from copper loss of the coil and iron loss of the core.

Since it takes time to conduct experiments and trial manufacturing for this type of design, electromagnetic field analysis simulation is used. It has been proven to be an effective design tool for faster development and estimation of properties difficult to verify in experimentation.

Fig. 8 shows an example of magnetic flux density vector distribution based on electromagnetic analysis. We are utilizing this to optimize the design of the core structure by confirming magnetic circuit configuration and uneven magnetic flux density distribution which

may cause abnormal heating. This information is provided by analysis of the current on the coil, intensity of generated magnetic field, and magnetic flux density.

NTN is also conducting thermo and electromagnetic analysis through the finite element method. Fig. 9 shows an example of the temperature distribution analysis of the reactor. By optimizing conditions for analysis, such as the heat transfer coefficient, temperature distribution of the product in operation can be precisely analyzed. This analysis is contributing to the verification and countermeasures for heat resistance and radiation.

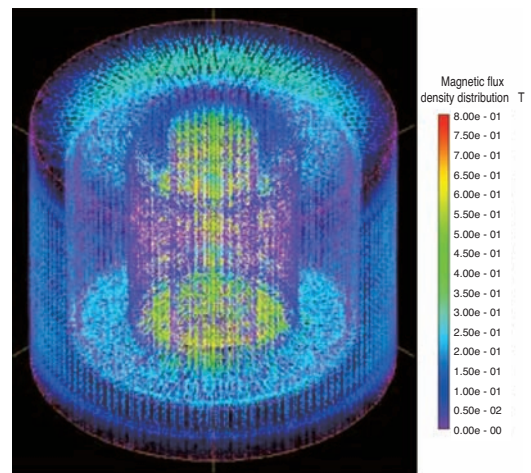
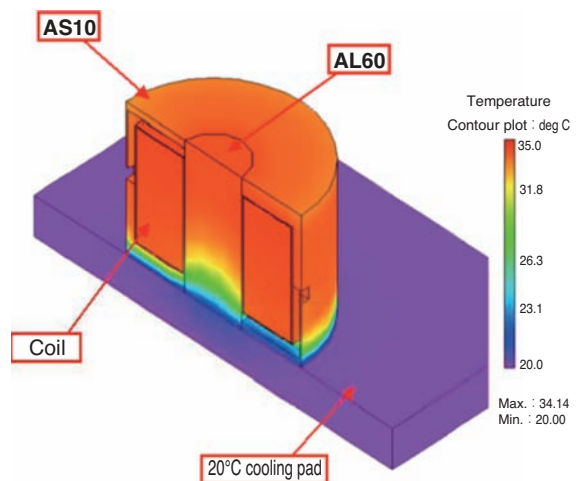


Fig. 8 Magnetic flux density vector distribution of a reactor



		Experimental data	Analyzed data
Heated temperature (°C)	Coil	42	35
	Core	40	34

Fig. 9 The temperature distribution analysis of reactor

6. Summary

Nippon Kagaku Yakin Co., Ltd. developed an amorphous alloy with excellent magnetic properties:

<Benefits of the developed core>

- (1) High saturation magnetic flux density and low degradation of properties, even with large current
- (2) Low degradation of properties at high frequencies
- (3) Low iron loss

We are planning to propose our reactor cores for HEVs to our customers, taking full advantage of the optimized design by electromagnetic and thermal analysis and proprietary manufacturing technologies. This technology will contribute to the improvement of driving performance of HEVs and EVs.

References

- 1) Takuji, Harano, Shinji Miyazaki, Hajime Katsuura: Introduction of Magnetic Material Products, NTN TECHNICAL REVIEW No. 80 (2012) 87-91
- 2) Masayuki Morimoto, Kiyoshi Kanamura et al.: Latest Control Technology for Electric Vehicles, NTS (2011) 78
- 3) Japan Electronics and Information Technology Industries Association: Soft Magnetic Metal Materials
- 4) The Society of Non-Traditional Technology: Magnetic materials of the new era
- 5) Hirota: The Magnetism Society of Japan, Bulletin of the 4th Topical Symposium

Photo of authors



Takayuki ODA
Engineering,
Nippon Kagaku Yakin Co., Ltd.



Shinji MIYAZAKI
Engineering,
Nippon Kagaku Yakin Co., Ltd.



Eiichirou SHIMAZU
Advanced Technology
R&D Center

Hub Bearing with an Integrated High-Resolution Rotation Sensor

Kentaro NISHIKAWA*
Toru TAKAHASHI**
Christophe DURET***



Wheel Speed Sensor is one of the most important sensors on a vehicle and used not only for ABS but also for various control systems. We have developed a new sensor device for high-resolution rotation sensing application and now the sensor can be integrated on hub bearings. In this article, we present the function of the high-resolution rotation sensor hub bearings along with some of the novel data measured on the test vehicle.

1. Introduction

Wheel speed sensors are critical components for vehicle safety control and are widely used not only for anti-lock brake systems (ABS), but also for various control systems such as electronic stability control (ESC).

Sensors have evolved from the passive sensor method consisting of a pick-up coil and a pulsar ring to the active sensor method that employs magnetic sensors such as hall elements and MR elements enabling consistent detection of rotational speed from park to high speed driving.

NTN is promoting unit development where sensors are also integrated into the seal of the hub bearings with magnetic encoders and has commercialized ABS sensor integrated hub bearings (shown in Fig. 1), and sealed sensor integrated hub bearings with enhanced reliability ¹⁾.

While bearings with rotation sensors (shown in Fig. 2) are used in industrial machines and are equipped with output resolution of several tens of pulses per rotation, the demand for higher resolution is increasing along with the evolution of control systems. However, increasing resolution by refining the magnetization pitch of the magnetic encoder causes reduction of the magnetic force. Therefore, NTN-SNR has been pursuing the improvement of the sensor capabilities and has developed a high-resolution sensor with upconversion detection capability (MPS40S) ²⁾. With



Fig. 1 ABS sensor integrated HUB bearings

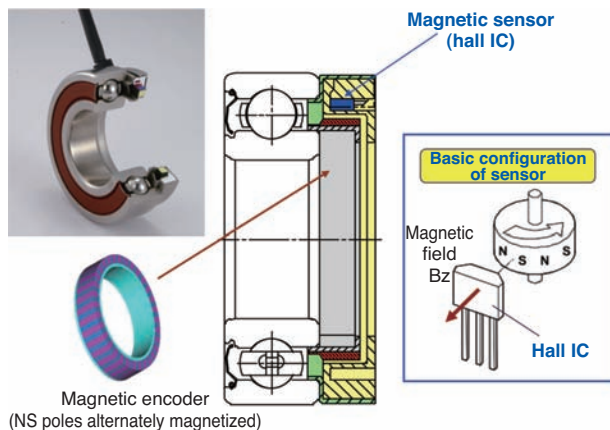


Fig. 2 Rotation Sensor Bearing

*Chassis Engineering, Automotive Business HQ

**New Product Development R&D Center

***NTN-SNR ROULEMENTS Research & Innovation Mechatronics

this technology the detection of rotation is now possible with a resolution that is 40 times higher than the conventional method, even if the sensor is combined with conventional magnetic encoders. NTN-SNR has also developed a tunnel magnetoresistance effect (TMR) element with high sensitivity as the next generation magnet sensor and is expected to be used in the vehicle application as a magnet sensor operable with a large air gap ^{3), 4)}.

The developed high-resolution sensor (MPS40S) complies with the environmental resistance specification required for vehicles and NTN is pursuing its application in the hub bearings. In this article, we provide an overview of hub bearings integrated with high-resolution rotation sensors and introduce some examples of analyses of high resolution signals measured with the sensor-equipped vehicle.

2. Overview of high-resolution rotation sensors

2.1 Structure/configuration

Fig. 3 shows pictures of high-resolution rotation sensors integrated hub bearings. For driving wheels, the sensor is molded with resin together with the fixing core grid and press fit onto the stationary ring (outer ring) of the hub bearings (shown in Fig. 4). For idler wheels, the sensor is fixed inside the water-resistant cap.

In either case, sensor assembly and adjustment process on the vehicle can be omitted since the position between the magnetic encoder and the sensor is controlled by integrating the sensors onto the hub bearings.

2.2 Electric specification/output signal

Mainstream ABS sensors for vehicles use 2-wire interface supplying 9-15V battery power, detecting 14 mA or 7 mA operating current that changes with the rotation. On the other hand, the developed high-resolution sensor uses 5V of supply voltage and outputs a digital voltage signal on the independent signal line. Therefore, it can be connected to the standard digital input terminals that vehicle electric control units (ECUs) have without any conversion circuits.

Table 1 shows key electrical specifications of high-resolution sensor integrated hub bearings. Since the sensor is equipped with output of A/B phases similar to the ordinary rotary encoder output signals, it is capable of detection of the rotational direction, quad edge evaluation processing using A/B phase edges, etc. These electrical specifications comply with the sensor IC specifications ⁵⁾.

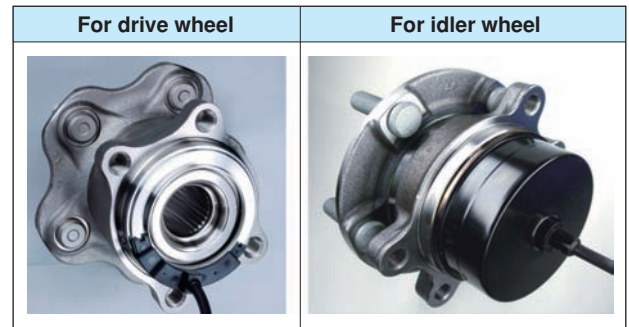


Fig. 3 High-resolution rotation sensor HUB bearings

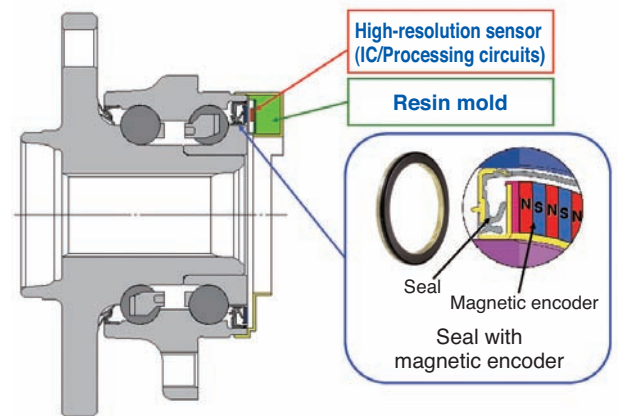


Fig. 4 Integration of the high-resolution sensor

Table 1 Electrical specification of the rotation sensor

Item	Value
Supply voltage $V_{dd}[V]$	5±0.5
Consumption current $I_c [mA]$	40 or less
Output voltage $V_H[V]$ $V_L[V]$	$V_{dd} \times 0.8$ 0.4 or less
Max. output current $I_{out} [mA]$	±15
Start time	500µs or less
Number of output pulses	Number of encoder pole pairs (PP) × multiplication number (m_x)
Multiplication number setting m_x	x40, x20, x10, x5, x32, x16, x8, x4, x2
I/O connection	Power input GND A-phase output B-phase output ABS signal output *

* Optional (output signal without multiplication)

2.3 Resolution and accuracy of rotational speed detection

The high-resolution rotation sensor realizes the multiplication process shown in Fig. 5. This means the duration of one pair of magnetic poles (cycle) is electrically interpolated to generate pulses with cycles of $1/(\text{multiplication number } m_x)$. The interpolated output signals are superimposed with slight errors depending on the distortion of the input magnetic field

and characteristics of multiplication circuits. Therefore, the pulse width slightly fluctuates, synchronized with the cycles of the magnetic poles of the magnetic encoder even when the rotation is at a constant speed. The magnitude of fluctuation is 0.5% or less over the cycle of one pole pair and has a characteristic of repeating along with the cycle of the magnetic poles. Therefore, when the rotational speed is detected using the multiplied pulses, the impact of multiplication error can be effectively reduced by applying a filtering process that uses pulse data from the number of pulses equivalent to one magnetic pole pair cycle.

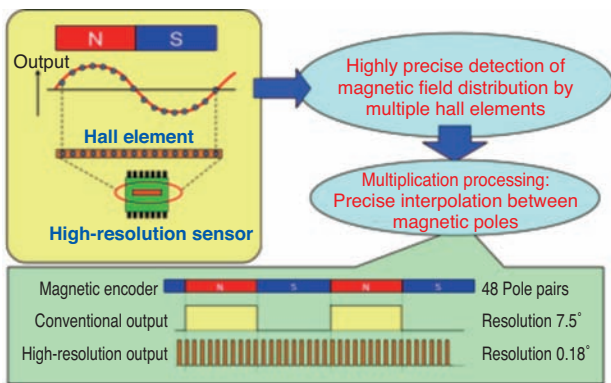


Fig. 5 Interpolated signal of the developed sensor (40 times at most)

3. Output signal of high-resolution wheel speed sensor

3.1 Application of high-resolution rotational signal

Conventional wheel speed sensors output around 48 pulses per rotation. Converting this to the running distance, it is equivalent to the resolution of one pulse per around 40 mm.

The high-resolution rotation sensor provides resolution of one pulse per 1 mm of running distance.

Table 2 shows the output pulse cycle at an extremely low traveling speed of 1 km/h. The interval between output pulses of the conventional sensor is 150 ms meaning it takes a maximum of 150 ms before detecting rotation. However, using output signals of the high-resolution rotation sensor, the detection is completed in 3.7 ms. Therefore, even at a ultra-low speed it is possible to ensure a sufficiently fast data update rate.

Thus, the benefit of using a high-resolution rotation sensor is its enhanced space and time resolution.

The following describes its benefits compared to conventional products.

(1) Rotational signals can be obtained with sufficient

- frequency even at ultra-low speed
- (2) A sufficient amount of data can be obtained even from a short traveling distance
- (3) Rotation immediately after start or immediately before stop can be accurately detected

Table 3 shows examples of high-resolution rotation sensor signal applications. In the following sections, we introduce run data of the test vehicle.

3.2 Test vehicle with the sensor

We drove the test vehicle with the high-resolution rotation sensor. Table 4 shows the specification of the sensor and the test vehicle.

The resolution of the rotation pulses were set to 480 pulses/rotation, which is 10 times higher than the conventional product. The sensors were mounted on the four wheels of the rear wheel drive vehicle to check the difference of rotation behavior between the drive wheels and the idler wheels.

Table 2 Comparison of output resolutions

	Number of output pulses (per rotation)	Resolution of movement detection	Interval of output pulses when driving at 1 km/h
Conventional ABS sensor	48	40mm	150ms
High-resolution rotation sensor	1,920	1mm	3.7ms

Tire radius of 305 mm assumed

Table 3 Application of high-resolution signals

Vehicle condition to be evaluated		Application
Drive/brake	Tire rotation at 1 km/h or less	Automatic driving/parking Hill hold
	Determination of rotational direction	Hill hold
	Drive/brake torque	Improved TCS*
	Higher accuracy and response for difference of rotation speed of right/left wheels	Improved ESC**
Tire condition	Change of tire pressure	Indirect TPMS***
	Change of shape/abnormal wear	Vehicle control in general Safety alarm device
Road condition	Dry/wet (μ estimation)	Vehicle control in general

*Traction Control System
 **Electronic Stability Control
 ***Tire Pressure Monitoring System

Table 4 Specification of the test vehicle

	Item	Specification	Remarks
Vehicle	Drive	RWD	Rear Wheel Drive
Tire	Size	225/55R17	
Sensor	Installation location	All wheels	Common to four wheels
	Magnetic encoder	48 pole pair/rotation	90-degree phase difference output
	Multiplication number	10 times	480 pulses/rotation
	Output signal	A-phase, B-phase	
Measurement	Pulse detection method	Measurement of time between pulse edges	
	Sampling frequency	80MHz	

3.3 Running data (1)

-Estimation of the road conditions-

A method of estimating road conditions is being proposed by analyzing frequency response of speed variation components extracted from the wheel rotation signals of running vehicles ^{6), 7)}. Fig. 6 shows an example of estimating tire-road surface conditions from the variation of rotational speed. In this kind of analytical method from frequency response, data needs to be extracted under the condition of constant speed since the spectrum resolution degrades as the traveling speed changes. It is not easy to extract sufficient varying speed information using the conventional sensors when vehicles run at low speed.

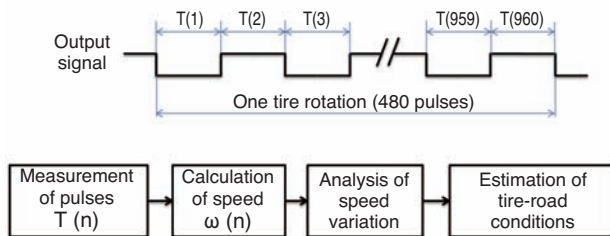


Fig. 6 Signal processing using the rotation signal

As a way to ease this extraction conditions, at **NTN-SNR** we are also exploring a method to estimate road conditions by order frequency analysis of the speed variation components adopting a method to sample speed on the basis of angle-of-rotation using the high-resolution sensor signals ⁸⁾. In the following, we describe an example of run data processing with the test vehicle, to show how to extract variation of rotational speed.

After starting and accelerating for about 30m, rolling on the asphalt road at 25 to 30 km/h, we drove onto the asphalt road with fine sand on the surface three times. Fig. 7 and 8 show the frequency analysis results of the speed variation components extracted from the rotational pulse signals of the front right wheel.

These figures show the results of FFT process using speed information at the respective times for one rotation of the wheel, sequentially displaying the spectrum calculated at the interval equivalent to 1/10 of the wheel rotation which is about 0.2 m of traveling with the traveling distance on the horizontal axis.

Fig. 7 uses frequency (vibration) for the vertical axis and Fig. 8 uses spatial frequency (wave number) for the vertical axis. The color bar on the right of the graphs shows the correlation between the strength and color and indicates that the colors on the upper

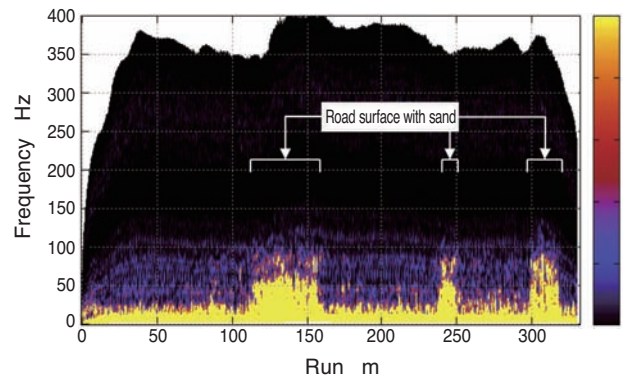


Fig. 7 Time-domain spectral diagram (Vibration frequency (Hz) in vertical axis)

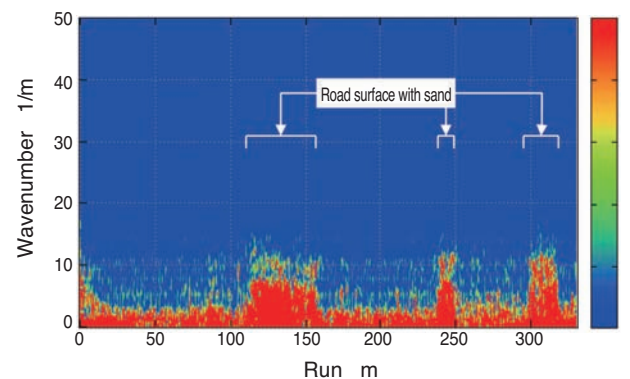


Fig. 8 Spatial-domain spectral diagram (Spatial frequency -wavenumber (1/m) in vertical axis)

area of the color bar are stronger. Fig. 7 only plots the components up to the 100th order, therefore, frequencies over those components are left blank.

The speed variation spectrum of the running vehicle shows changes in the areas corresponding to the road surface with fine sand. In these areas, it is revealed that the speed variation is increased and the variation is spread out to the high frequency range. Because high-resolution rotational pulses are used, frequency components higher than the conventional methods were extracted. It also shows that higher order components can be extracted even when the drive speed is not constant since sufficient data can be obtained even on a short drive.

3.4 Running data (2) -Detection of rotation at acceleration/deceleration-

During initial acceleration and acceleration/ deceleration on slippery roads, vehicles are likely to become unstable because of the wheel slippage. Use of high-resolution rotation sensors enables detailed observations of the wheel behavior at extremely low speed for early detection of slippage or determination of whether the wheel is locked immediately before

stopping.

As an example, Fig. 9 shows the rotation speed data of the front wheel (idler wheel) when a car stops at a traffic light with the brake applied and starts rolling after releasing the brake.

A variation of rotation is observed at the area indicated by an arrow. This shows that the vehicle stopped with load applied by braking and strain was given to the suspension. The observation then reveals that when the brake is released, the front wheel was pushed forward and started rotating. On the other hand, from the output signals of the ABS sensor collected at the same time, this kind of observation was not obtained and the detection of rotation was approximately 0.28 seconds late.

Fig. 10 shows a behavioral data of the rear wheel (drive wheel) when a car begins accelerating on a slippery road as another example. At around 0.65 seconds, a slippage is observed and the high-resolution rotation sensor signals display a smooth curve of how rotation speed rapidly increases. The slip is detected about 0.05 seconds earlier than the speed data from the ABS signals and a sufficient number of data is also acquired for calculating acceleration from the rate of speed variation. Therefore with the high-

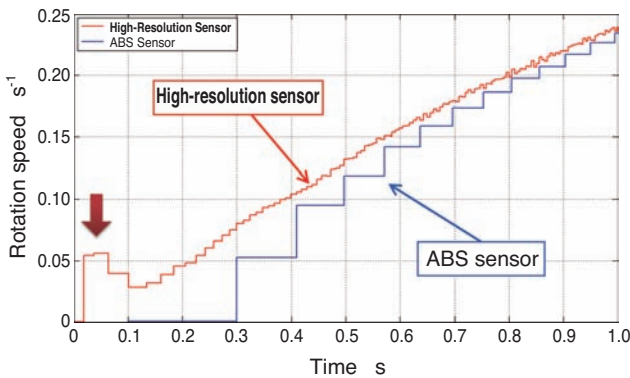


Fig. 9 Rotation signal after releasing brake

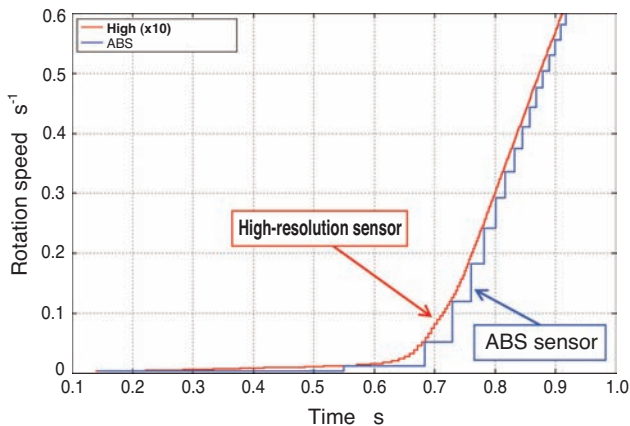


Fig. 10 Slipping on the low-friction surface

resolution rotation sensor, it is possible to provide effective information for traction control on low μ roads (slippery roads) which requires refined torque control, etc.

3.5 Running data (3)

-Observation of non-repetitive phenomena-

The rotation sensor signals reflect the road conditions.

While the example described in section 3.3 used analysis results of variation of rotation speed observed for a certain duration, the example in the following uses a single input to detect road disturbances.

Fig. 11 shows a variation of rotation speed of four wheels when a vehicle passed a joint of the road surface while driving on a bridge at the speed of 20 km/h. An oscillatory waveform of 15 to 35 Hz is observed at the joint, however, the waveforms and vibration frequency are different between the idler and drive wheels. It is considered that the road conditions and the driving force to the wheels are reflected to the rotation speed signals.

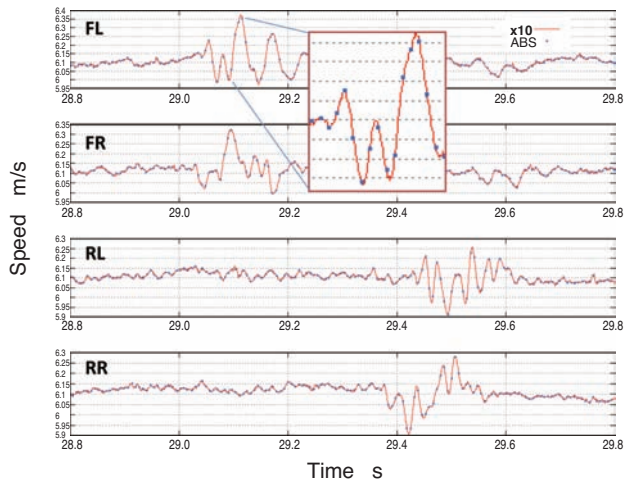


Fig. 11 Rotation signals at a road joint

4. Conclusion

In this article, we have described an overview of the high-resolution rotation sensor integrated hub bearings and introduced examples of run data with the test vehicle. It was clarified that sensing response and accuracy of extracted information can be improved by detecting rotation speed of the wheels at high resolution. We strive for broad adoption of this technology as a means for contributing to improved vehicle safety including deployment in the control applications of the electric vehicles.

References

- 1) Eiji Funahashi, "History of Hub Bearings and Recent Technology", NTN TECHNICAL REVIEW No. 70, pp 52-57 (2002)
- 2) P.Desbiolles, A.Friz, "Development of High Resolution Sensor Element MPS40S and Dual Track Magnetic Encoder for Rotational Speed and Position Measurement", NTN TECHNICAL REVIEW No.75 pp36-41 (2007).
- 3) C. Duret, S. Ueno, "TMR: A New Frontier for Magnetic Sensing", NTN TECHNICAL REVIEW No. 80 pp64-71 (2012)
- 4) C.Duret, J.Paul, B.Negulescu, M.Hehn, "TMR: A New Frontier for Magnetic Sensing", Proc. of 11th MR Symposium, Wetzlar, 2011.
- 5) H. Ito, T. Takahashi, P. Desbiolles, C. Peterschmitt, S. Ueno, "High Resolution Sensor Bearing with an Index Signal", NTN TECHNICAL REVIEW No. 78 pp 76-82 (2010)
- 6) Katsuhiko Asano, Eiichi Ono, Takaji Umeno, Masaru Sugai, Yoshitoshi Watanabe, "Estimation of Tire-Road Friction", Journal of Society of Automotive Engineers of Japan, Vol. 61 No.2 pp 50-55 (2007).
- 7) Takaji Umeno, "Estimation of Tire-Road Friction by Tire Rotational Vibration Model", R&D Review of Toyota CRDL, Vol. 37 No.3 pp 53-58 (2002).
- 8) NTN-SNR, Patent No. 4777347

Photo of authors



Kentaro NISHIKAWA
Chassis Engineering
Automotive Business HQ



Toru TAKAHASHI
New Product Development
R&D Center



Christophe DURET
NTN-SNR ROULEMENTS
Research & Innovation
Mechatronics

Press Connect Spline Hub Joint

Takayuki NORIMATSU*
Tsutomu NAGATA*



In the automotive industry in the world, low fuel consumption is an important issue, the lightening to become one of the solution is demanded from every part constituting a car. NTN developed the lightening of a hub bearing and the CV joint in order to meet these demands.

This report introduces "PCS-hub joint" which is lightening by connecting a hub bearing and CV joint by "the press connect method" that is NTN original technology.

1. Introduction

High fuel economy is an important requirement in the automotive industry today. One of the solutions for achieving high fuel economy is a lightweight design, which is now required for all vehicle components.

In this article, we introduce the "Press Connect Spline Hub Joint (PCS-H/J)" which is 12% lighter than our conventional product and eliminates backlash of the spline joint by connecting the hub bearing (H/B) and the constant velocity joint (CVJ). NTN's technology for the "Press Connect Method" does not require any change in the assembly process of the automotive manufacturers.

2. Structure and features

NTN has been developing the "V-Series Hub Joint (V-H/J)"¹ as an integrated unit of the H/B and CVJ connected with the "Press Connect Method", which uses a swaged CVJ outer ring stem (**Fig. 1b**) to assemble the third generation H/B+CVJ (**Fig. 1a**) where conventional H/B and CVJ are fastened together with a nut. H/B and CVJ are inseparable with V-H/J design and so the vehicle assembly process needed to be changed at the automotive manufacturers. To solve this problem, the newly developed "PCS-H/J" is designed to fasten the H/B and CVJ with a bolt which also assisted in reducing the spline pressure load (**Fig. 1c**).

2.1 Joint methods of components

The joint methods of H/B and CVJ are described using **Fig. 1** in the following:

a) Conventional structure (third generation H/B+CVJ)

Splines are provided on the outer diameter of the CVJ outer ring stem and on the inner diameter of H/B, which are then fit together to transmit torque. The transmission of torque from CVJ to H/B is conducted through the contact of the spline teeth. However, close contact of both components is difficult because of the machining accuracy (difference of pitch of the teeth between the splines). The resulting gap, as shown in the middle section of the figure, causes circumferential backlash. This prevents the torque to be borne by the entire spline, which requires the length of the spline engagement to be increased.

b) V-H/J

The CVJ outer ring stem is machined with special splines (teeth) that are thermally hardened and inserted into the H/B. This causes splines to be formed on the inner diameter of the H/B spindle ring with which CVJ and H/B are tightly connected. NTN calls this joint method the "Press Connect" method.

In this method, since the inner diameter of H/B is formed by elastic deformation, the recessed part of the H/B inner diameter and the raised part of the CVJ outer ring stem are tightly engaged. The input torque

*Chassis Engineering, Automotive Business HQ

can be uniformly borne by the entire teeth area allowing shorter spline engagement length compared to the conventional structure a).

Since the entire teeth area has to be formed, high power is required for the machining process including the use of machining equipment such as a press machine for the joint process, which is a challenge.

c) PCS-H/J

For PCS-H/J, splines are pre-formed on the inner diameter of H/B with smaller tooth width than the CVJ outer ring stem splines (Fig. 2 shows an example of pre-formed splines). The CVJ stem teeth and the splined grooves of the H/B are gapped at specified distances to reduce the power required for the assembly process of the H/B and CVJ that are fastened together by a bolt. With this design, the vehicle production line at the automotive manufacturers does not required to be changed for assembling PCS-H/J.

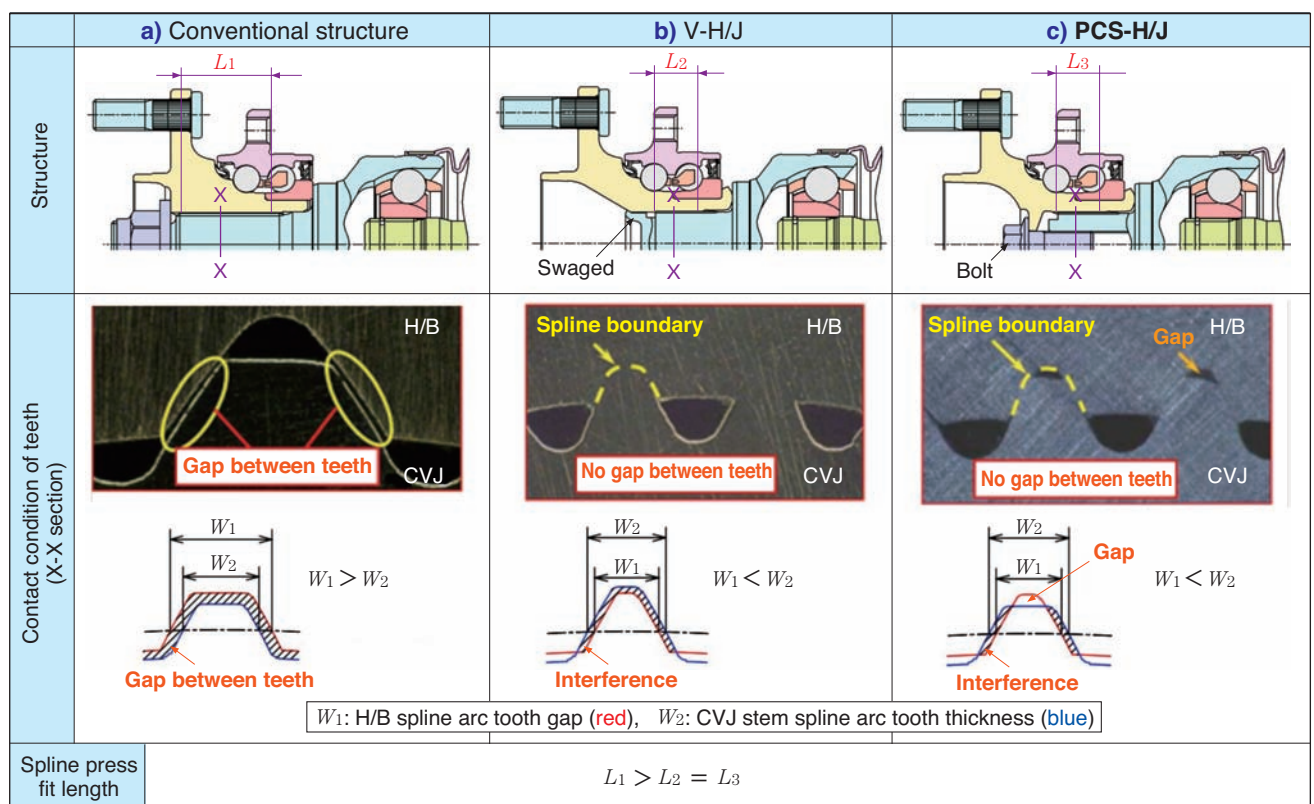


Fig. 1 Contact condition of teeth

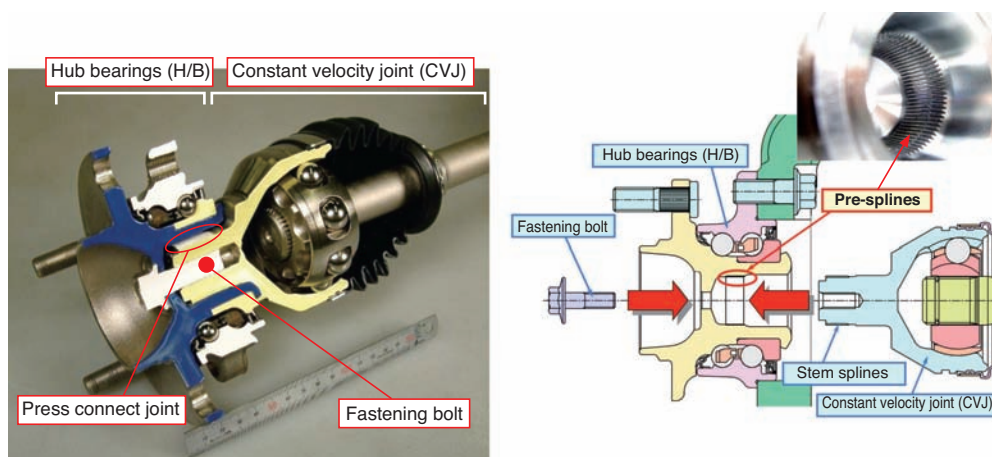
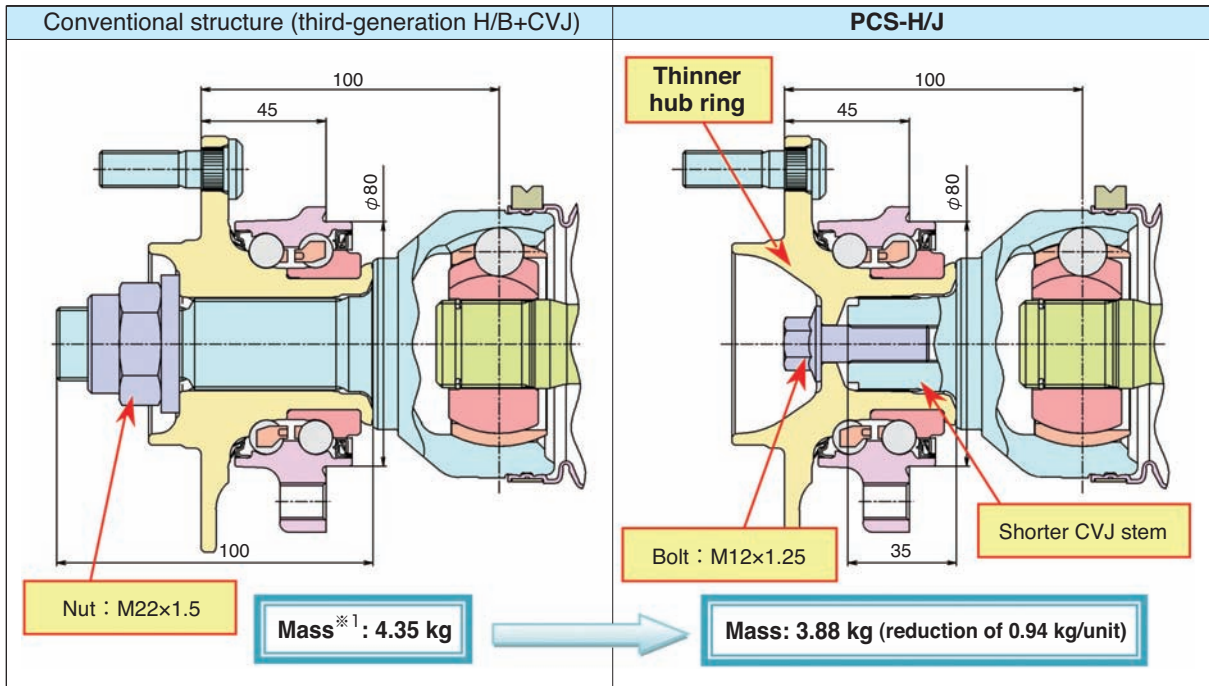


Fig. 2 Structure of PCS-H/J

2.2 Features

PCS-HJ achieved a significant lightweight and eliminated backlash on the splined area thanks to the adoption of the press connect method. Fig. 3 shows an example of the trial application on a C-segment vehicle.

With PCS-H/J, input torque is borne by the entire area of the teeth as opposed to the conventional structure, therefore, the length of the CVJ stem can be reduced by approximately 65%. Furthermore, the weight was reduced to 0.94 kg/unit (approx. 12%) by thinning the inside wall of the hub ring and by using a bolt instead of a nut.



*1: Mass of H/B+Outboard CVJ outer ring+nut or bolt

Fig. 3 Example of the application of PCS-H/J

3. Functional test

3.1 Spline press-fit load

With PCS-H/J, the CVJ outer ring stem is assembled to the inner diameter of H/B by use of a bolt. Fig. 5 shows the measurement results of the spline press-fit load using components with the upper and lower limits of the interference as shown in Fig. 4.

Fig. 5 shows that the spline press-fit load required for the upper and lower limits of interference is below the lower limit of the established axial force of the bolt which means that the H/B and CVJ can be assembled in all specified ranges of interference.

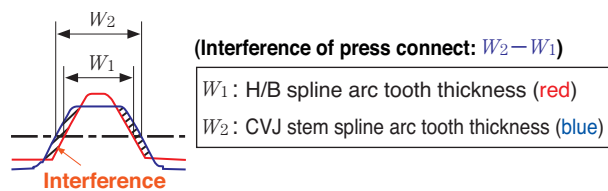


Fig. 4 Interference

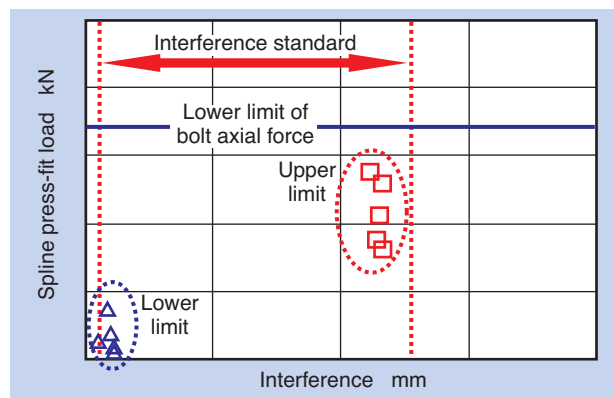


Fig. 5 Spline press fit test

3.2 Strength evaluation of the splined area

Static torsional and bi-directional torsional fatigue strength tests were conducted against the shortened splined area of PCS-H/J and had verified the strength was equal or better than the conventional unit.

3.2.1 Static torsional strength test

Static torsional strength test was conducted for breaking torque when torsional torque is applied in one direction. Fig. 6 shows the test results.

Although the splined area is short, PCS-H/J has equal or better strength than the conventional units.

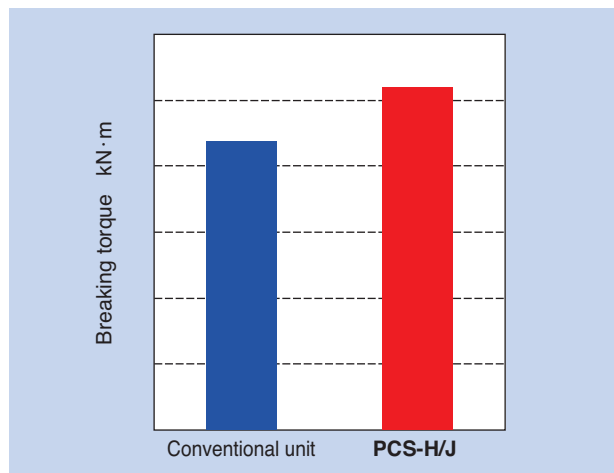


Fig. 6 Static torsional strength test

3.2.2 Bi-directional torsional fatigue strength test

A bi-directional torsional fatigue strength test was conducted where alternating torsional torque is repeatedly applied on the splined area and records the cycle count until the unit breaks. Fig. 7 shows the test results.

Both high torque and low torque were applied repetitively for the evaluation with the assumption that high torque and low torque is what is normally seen on vehicles. PCS-H/J demonstrated to have sufficient fatigue strength over the guaranteed life values of the conventional products even if the splined length is shorter.

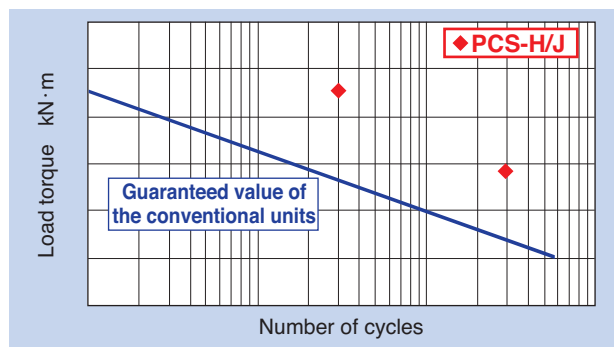


Fig. 7 Bi-directional torsional fatigue strength test

3.3 Disassembly/reassembly test

Service or replacement of the PCS-H/J components was studied. Disassembly of the H/B and CVJ was conducted and the spline press-fit load was evaluated when they were reassembled. The spline strength of the disassembly and reassembly unit was verified to be OK.

3.3.1 Measurement of spline press-fit load during reassembly after disassembly

In this test, spline press-fit load was measured with the combination of both new and reused H/Bs and CVJs, as shown in Table 1, and verified to see if interference still remained in the splined area of the reused components. Fig. 8 shows the test results.

Table 1 Sample combination

		CVJ	
		New	Reused 5 times
H/B	New	(1)	(2)
	Reused 5 times	(3)	(4)

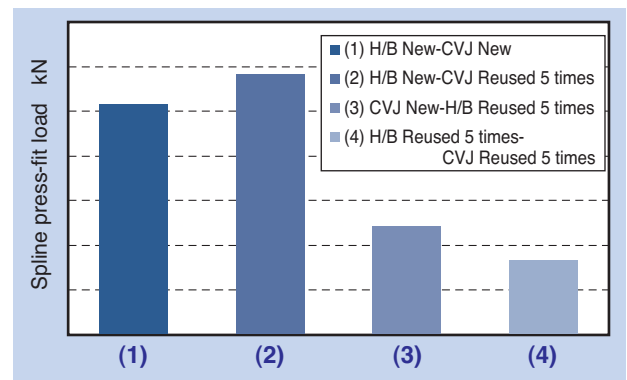


Fig. 8 Re-assembly load test

When only the CVJ was the reused component (Fig. 8 (2)), the press-fit load was almost the same as in the case of new components when comparing the spline pressure load of new components (Fig. 8 (1)). When only the H/B was the reused component (Fig. 8 (3)), the press-fit load was about half of the new component. The press-fit load decreased because the interference had been reduced as the H/B inner diameter was formed by the CVJ splines when the original CVJ was pressed in. When both H/B and CVJ were the reused components (Fig. 8 (4)), the press-fit load was approximately 1/3 of the new components.

Based on the above data it was revealed that when the H/Bs were reused, the press-fit load is reduced compared to the new components, however, the load is not zero and some interference still remained in the

splined area. In addition, the reused components were verified to be fit without any backlash being observed in the joint.

3.3.2 Bi-directional torsional fatigue strength test of disassembled and reassembled units

In order to verify the strength of the splined area of the disassembled/reassembled PCS-H/J, samples which have undergone disassembly/reassembly 5 times were placed on the bi-directional torsional fatigue strength test of the above section 3.2.2. Fig. 9 shows the results.

They were evaluated with high torque and low torque, similar to 3.2.2. The disassembled and reassembled unit has the equivalent level of strength as the first assembled (new) unit.

Based on the above data it was observed that the reuse of H/B and CVJ exhibits no problem for assembly or strength.

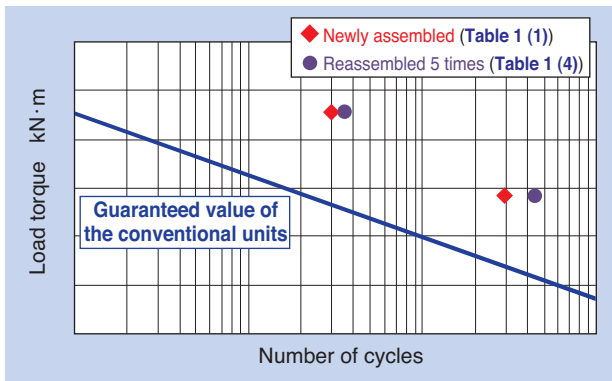


Fig. 9 Bi-directional torsional fatigue strength test

3.4 Verification of impact to H/B

Inspection of the raceway condition after bearings life testing was conducted to verify the impact of press connect on H/B.

3.4.1 Measurement of roundness of raceway

Roundness of raceway of the inner ring before and after press-fitting splines with upper and lower limits of interference (Fig. 4) was measured. Fig. 10 shows the results.

The roundness measurement value after press-fitting the splines increased by approximately 0.5 μm. No impact such as polygon strain was observed. Also, no difference between press connect interference was observed.

3.4.2 Turning life test with 0.8G

A load equivalent to 0.8G which simulates aggressive turning was applied to the PCS-H/J bearings so life testing could be conducted. Fig. 11 shows the results.

The bearing life was equivalent to the conventional products and no difference was exhibited.

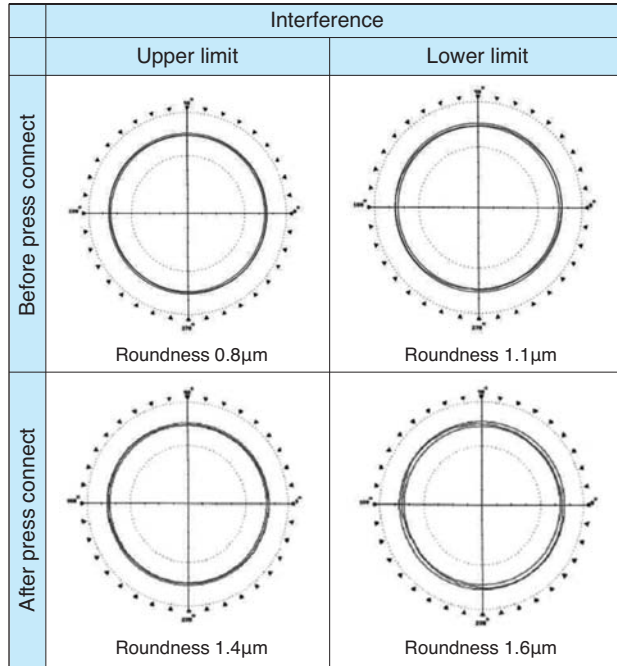


Fig. 10 Circularity measurement of raceway surface

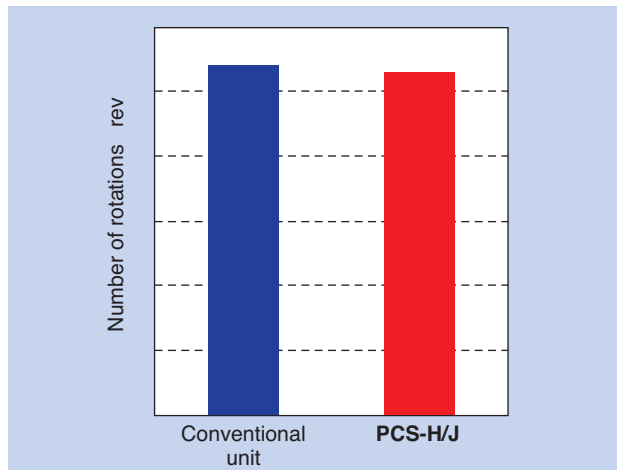


Fig. 11 Turning (0.8G) durability test

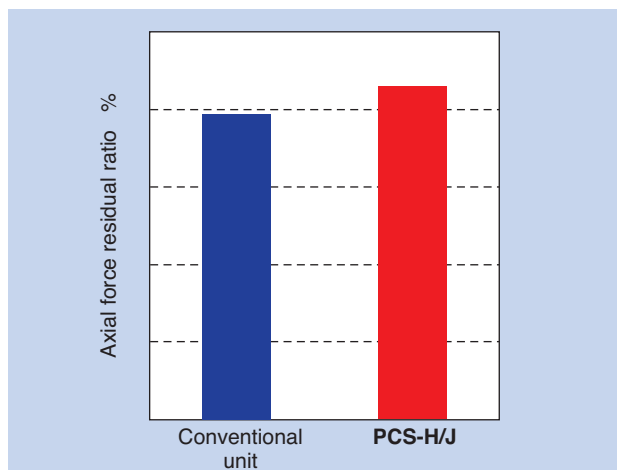


Fig. 12 Axial force residual ratio

3.5 Measurement of bolt axial force

Since the PCS-H/J uses a bolt for fastening instead of the conventional use of nuts (**Fig. 1**), loosening of the bolt during use in the field is a concern.

Bi-directional torsional torque was applied on the splined area of PCS-H/J for predetermined number of times and bolt axial force was measured before and after the test to verify if the bolt had loosened. **Fig. 12** shows the results.

No loosening was observed after the test and the residual ratio of the bolt axial force was 86% or more for PCS-H/J as opposed to the conventional nut fastening of approx. 80%. This is considered to be adequate for operational usages.

4. Summary

We have developed a lightweight PCS-H/J that has no backlash in the splined area by forming pre-splines on the inner surface of the H/B with smaller tooth width than the splines of the CVJ stem, and uses a bolt for connecting the H/B and CVJ.

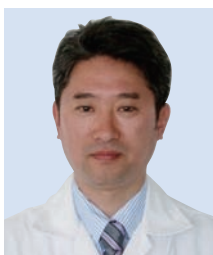
PCS-H/J can be assembled within the existing assembly process in the vehicle production lines of automobile manufacturers. We have pursued weight reduction with PCS-H/J which is desired for the modern vehicles and believe it will significantly contribute to improved fuel economy.

We plan to expand this PCS-H/J into a family of product lines and continue developing modular units.

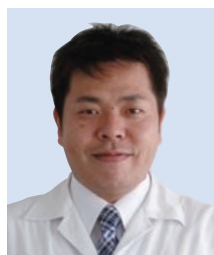
References

- 1) Mitsuru UMEKIDA, Yuuichi ASANO, "V-series Hub Joint", NTN TECHNICAL REVIEW No. 77 p67-72, 2009

Photo of authors



Takayuki NORIMATSU
Chassis Engineering
Automotive Business HQ



Tsutomu NAGATA
Chassis Engineering
Automotive Business HQ

Next-generation High Efficiency Fixed Type Constant Velocity Joint "CFJ"

Teruaki FUJIO*



The demand of low fuel consumption to the car from consideration of environment has increased in recent year. In NTN, in order to realize high efficiency of drive shaft, we developed a fixed constant velocity joint which reduced torque loss by original design. This paper introduces the feature and performance of the CFJ.

1. Introduction

The common challenge of the world automotive industry for achieving "high fuel economy" is to reduce the loss of torque from the components that comprise the powertrain.

The power from the engine is transmitted to the tires through the transmission, differential gear and drive shaft. This drive shaft is called constant velocity joint (CVJ) because it smoothly transmits torque at a constant speed even when the input differential gear shaft and output shaft on the tire side rotate at different angles. CVJ is usually configured with a fixed-type CVJ, which enables a greater joint angle but is not capable of axial sliding, and a sliding-type CVJ, which enables only a small joint angle but is capable of axial sliding, connected by a shaft (Fig. 1). As shown in Table 1, the torque loss of the CVJ has been small among the powertrain components; however, further improvement of efficiency is now required for overall high fuel economy.

Fig. 2 shows the history of weight reduction and efficiency improvements of fixed-type constant velocity joints at NTN. NTN has been working to enhance the fixed-type CVJ and was among the first to develop the lightweight, compact, and highly efficient E-Series³⁾ while contributing to the improvement of the vehicle fuel economy. On the other hand, the torque loss of the sliding-type CVJ is small compared with the fixed-type CVJ (about 0.2%) as the tripod type with integrated rolling bearings has been in the mainstream.

In this article, we introduce features and performance of "CFJ", which reduced torque loss by half against EBJ by adopting NTN's original design to reduce internal friction loss of the fixed-type CVJ.

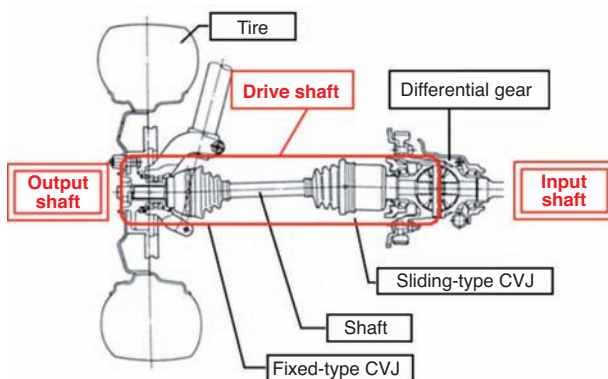


Fig. 1 Layout of drive shaft 1)

Table 1 Torque loss of drive-train 2)

Component	Torque loss rate
Transmission	1~5%
Differential gear	1~5%
Drive shaft (CVJ)	1%

*Drivetrain Engineering, Automotive Business HQ

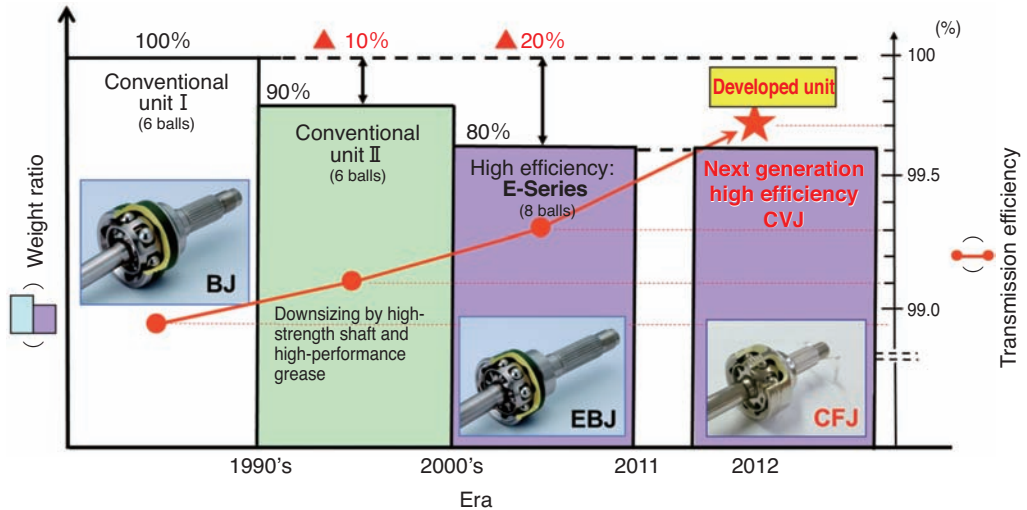


Fig. 2 Transition of the weight saving and increase in efficiency of NTN's fixed constant velocity joint.

2. Structure and features of CFJ

2.1 Structure of CFJ

CFJ consists of an inner ring/outer ring equipped with a ball raceway groove (track), eight balls that transmit running torque, and a cage that holds the balls (Fig. 3).

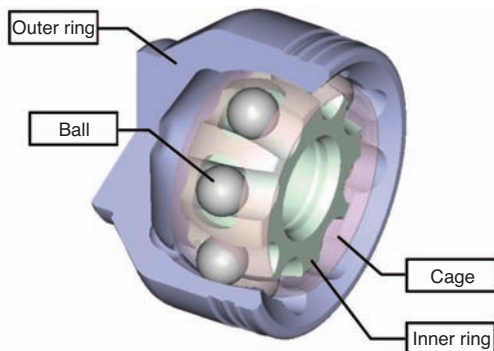


Fig. 3 Configuration of CFJ

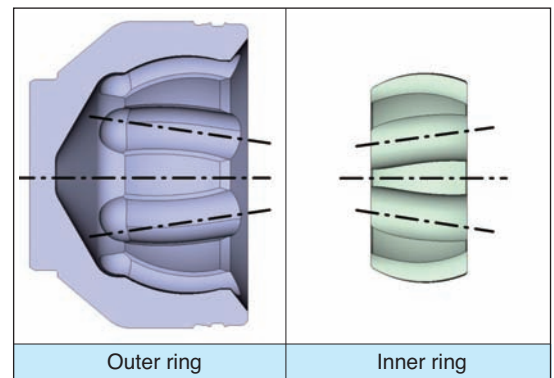


Fig. 4 Configuration of track form

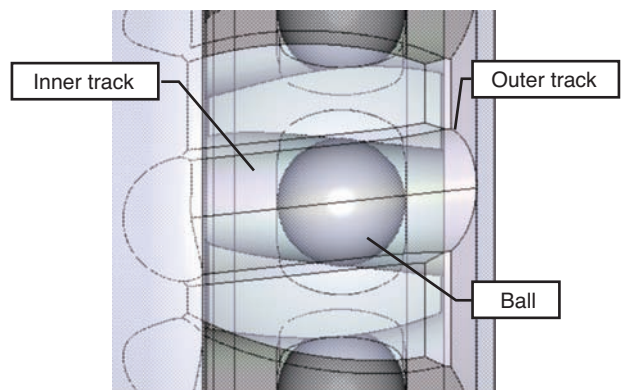


Fig. 5 Layout of track and ball

2.2 Features of CFJ

For reduction of torque loss, we have adopted our unique structure to reduce friction of contact points in CVJ.

Feature 1: Circular arc tracks of the inner and outer rings are inclined to the axial direction and the adjacent tracks are arranged in mirrored symmetry (Fig. 4).

Feature 2: The slopes of the inner and outer tracks are crossed with each other and a ball is placed in the intersection (Fig. 5).

3. Mechanism of reduction of torque loss

Torque loss of a CVJ is caused by the energy loss due to the friction of contact points.

Fig. 6 shows the contact conditions of the current EBJ. The tracks of the inner and outer rings are formed on the circular arc and their centers are displaced on the opposite directions from the joint center. The ball that transmits power is held by the tracks of inner/outer rings which form a wedge angle (τ) and is supported by the cage. When torque is applied to the joint, the tracks of inner and outer rings and the ball make contact and the ball is given force (F) to push the cage because of the wedge angle. Then, another load that balances with this force is generated between the cage outer spherical surface and the outer ring inner spherical surface, as well as the cage inner spherical surface and the inner ring outer spherical surface.

In the development of CFJ, we focused on the reduction of friction resistance of sliding motion on the spherical surface (Fig. 6 (4) and (5)).

Fig. 7 shows the inner force that is generated. As mentioned in Section 2, adjacent circular arc tracks are mirrored-symmetrically placed in the CFJ layout. The direction of the force that the balls push the cage (F) can be alternately distributed to the outer ring

opening side (F1) and the reverse side (F2). As F1 and F2 have the same magnitude and are applied in the opposite directions, they are cancelled out and the cage axial displacement is limited. As a result, the spherical contact force generated between the cage and outer ring, as well as the cage and inner ring can be significantly reduced.

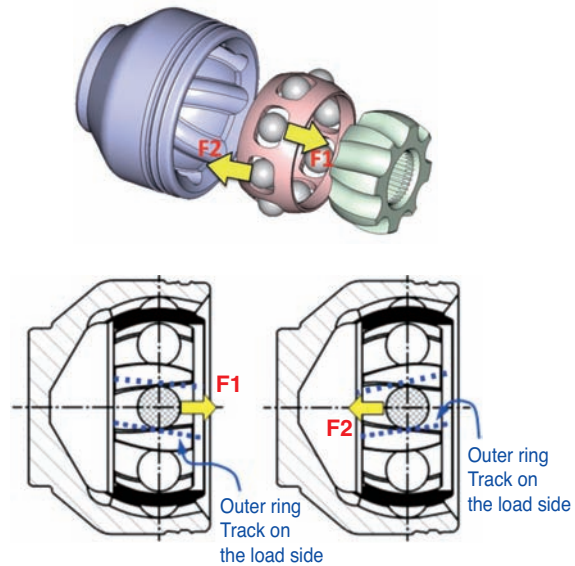


Fig. 7 Contact force of CFJ

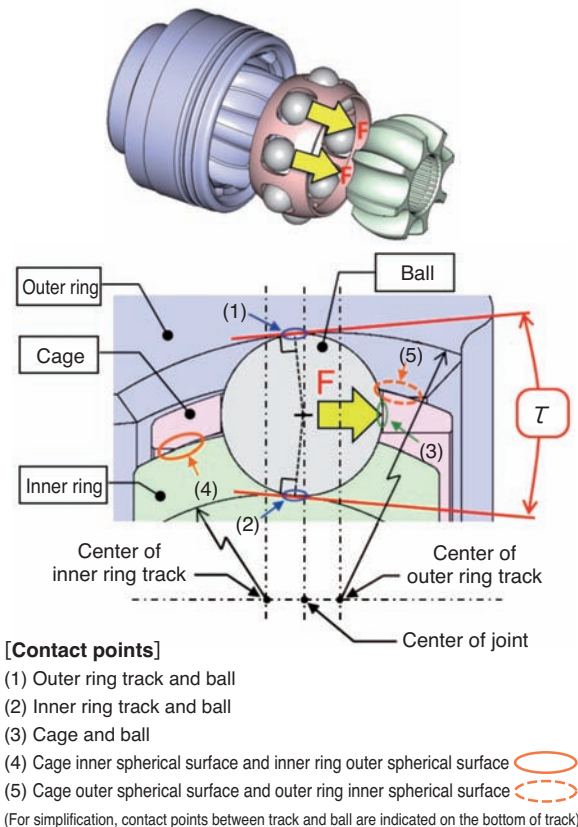


Fig. 6 Composition of EBJ

4. Verification by analysis

Fig. 8 is a comparison of contact force of spherical parts between CFJ and EBJ which is obtained by structural analysis. It shows that the contact force of spherical parts of CFJ is significantly low at any joint angles.

We could verify that the mechanism of the torque loss reduction by our unique structure is working as designed from the analysis result as well.

We also obtained similar results for the force between the cage and inner ring.

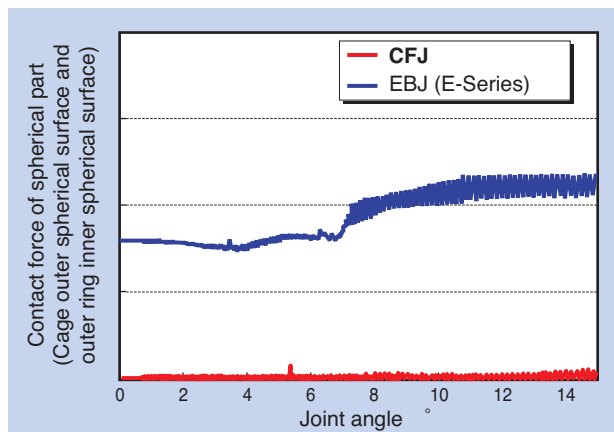


Fig. 8 Analysis result of contact force of spherical part

5. Performance characteristics

5.1 Transmission efficiency (torque loss rate)

Fig. 9 shows a comparison of torque loss rates among CFJ, EBJ, and BJ which is used worldwide as conventional joint.

It shows that the current EBJ has lower torque loss rate and higher efficiency than BJ. We could verify that CFJ's torque loss rate is significantly lower than EBJ at the joint angles of more than 6 degrees.

In general, torque loss rate deteriorates as the joint angle increases because of the increased relative motion of the internal components; however, CFJ is not very affected by the joint angles, thus maintaining a low torque loss. Therefore, CFJ is able to provide a higher loss reduction effect when installed on the vehicles where the joint installation angles become relatively large such as SUVs having a greater vehicle height.

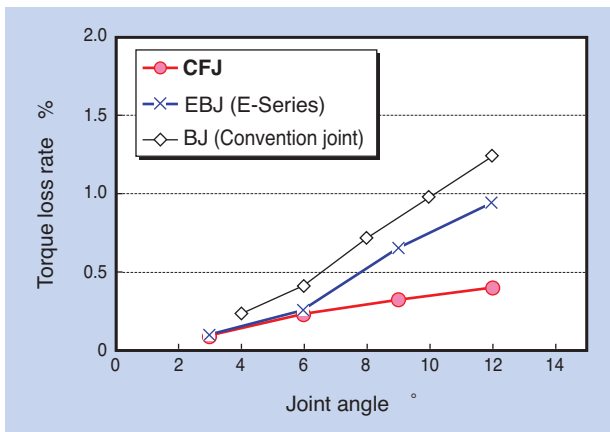


Fig. 9 Comparison of torque loss rate

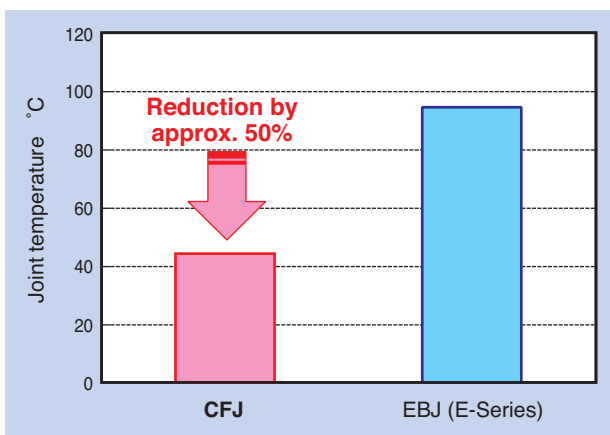


Fig. 10 Comparison of joint surface temperature

5.2 Increase of temperature

Fig. 10 shows a comparison of increase of temperature between CFJ and EBJ.

CFJ is able to reduce not only torque loss but also self-heating, which reduces the joint surface temperature by around 50% compared to EBJ. This allows expanded application of operating range in high rotational speeds.

6. Summary

We have developed the "CFJ" which is a next-generation high efficient fixed type CVJ that reduces torque loss rate by 50% compared to the current E-Series at the joint operating angle range of over 6 degrees. It achieved the highest level of efficiency and heating reduction in the industry by reducing significant internal friction loss using our unique design.

NTN would like to contribute to further global environmental protection by expanding this next-generation fixed type CVJ with its superior transmission efficiency in the global market in response to the ever-increasing demand for improved fuel economy.

References

- 1) Manabu HOSHINO, Masashi FUNAHASHI: Fixed Constant Velocity Joint with a Super High Operating Angle of 54 Degrees (TUJ), NTN TECHNICAL REVIEW No. 75 (2007), 16-19
- 2) Society of Automotive Engineers of Japan: Automotive Engineer's Handbook, Toshoshuppan, Tokyo (1979), 3-35.
- 3) Keisuke SONE, Kazuhiko HOZUMI: High Efficiency Compact Fixed Constant Velocity Universal Joints (EBJ), NTN TECHNICAL REVIEW No. 66 (1997), 28-31

Photo of author



Teruaki FUJIO
Drivetrain Engineering
Automotive Business HQ

Development of Low Torque Seal Ring for Automotive Transmission



Kouzou KAKEHI*
Takumi KONDOU*
Takuya ISHII**
Masato YOSHINO***

Further lower level of torque and oil leak is required of seal rings used in AT and CVT as fuel economy standards of cars is higher in the future. Therefore, NTN developed “Low Torque Seal Ring”, which is made of PEEK resin and equipped with specially-shaped lubrication grooves by injection molding, keeps low torque (60% reduction) and low wear properties in comparison with NTN conventional products and keep its oil leakage characteristic equal to conventional one. This article introduces the characteristic and performance of “Low Torque Seal Ring”.

1. Introduction

Automatic transmissions (AT) and continuously variable transmissions (CVT) use 4 to 10 resin seal rings of 15 to 60 mm outer diameter. As stricter fuel economy standards are expected to be introduced for vehicles, seal rings are required to have even lower torque and lower oil leakage characteristics.

In this article, NTN is introducing the “Low Torque Seal Ring” with high functionality by using specially-designed lubrication grooves to the seal rings made of polyether ether ketone (PEEK) resin ^{1), 2)}.

2. Roles and challenges of seal rings

2.1 Roles of seal rings

Seal rings are moving seals which seal oil in a sliding action. Seal rings are installed between relatively moving shafts and housings in the hydraulic circuit of automatic transmissions (AT) and CVTs, as shown in Fig. 1. They seal oil and maintain pressure within the hydraulic circuit while being pressed to both the housing and shaft by hydraulic pressure in a sliding motion.

The required performance for seal rings is low torque, low oil leakage and low friction. Low torque improves the transmission efficiency and saves

energy. Low oil leakage allows for high efficiency and smaller size of the oil pump, resulting in energy savings. In order to maintain low torque and low oil leakage long-term, and extend the life of the components, it is necessary to minimize wear of the seal rings and components on which the seal rings slide.

Seal ring materials are mainly polytetrafluoroethylene (PTFE) resin and PEEK resin. PTFE resin seal rings are made by machining compression molded material, while PEEK resin seal rings are made by injection molding. The seal rings made of PEEK resin with complex abutment geometry from injection molding exhibit lower oil leakage than the seal rings made of PTFE resin with simple and straight abutment geometry.

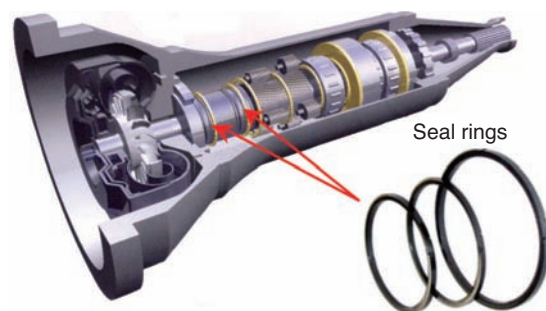


Fig. 1 Structure of automatic transmissions

*Engineering Dept, NTN Engineering Plastics Corp.

**Composite Material Engineering Dept, Composite Material Products Division

***Advanced Technology R&D Center

2.2 Challenges of seal rings

In general, the cross-section shape of a seal ring is either rectangular or trapezoidal. The respective operations are shown in Fig. 2.

The rectangular seal ring is pressed by hydraulic pressure to the inner surface of the housing and the side wall of the shaft groove. The contact area between the seal ring and the shaft groove side wall is smaller than the contact area between the seal ring and the housing inner surface. Therefore, when the housing or the shaft rotates, the seal ring side and the side wall of the shaft groove slide due to their smaller sliding resistance. Since the contact area with the shaft groove side wall is large, the leakage is small but the torque is high.

The trapezoidal seal ring also slides on the shaft groove side wall similar to the rectangular seal ring. But since there is a gap between the seal ring side and the shaft groove side wall, and hydraulic pressure is also applied from that side, the torque is reduced compared to the rectangular seal ring. However, the small contact area with the shaft groove side wall causes higher and unstable oil leakage. In addition, wear of the seal rings makes the contact area larger, resulting in gradually increased torque, closer to the value of the rectangular seal rings. Therefore, rectangular seal rings, which have more stable torque and oil leakage, are used more often.

In order to solve these issues, NTN has developed a seal ring that achieves both high sealing and low torque properties by providing a V-shape groove on the side of the seal ring (referred to hereafter as V-groove seal ring).

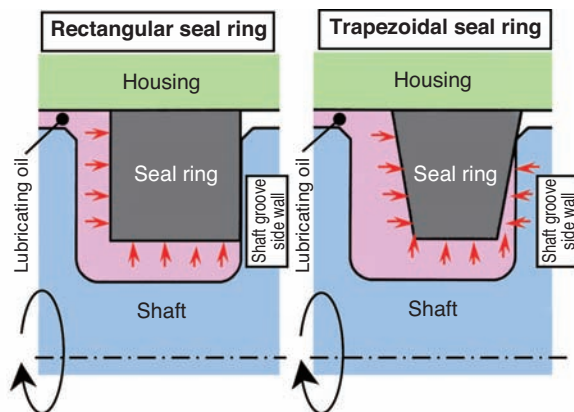


Fig. 2 Operating state of seal ring

3. Features of V-shape groove seal ring

Fig. 3 shows the structure of the V-groove seal ring. Providing the V-shape lubrication groove on the side wall of the rectangular seal ring makes the contact area with the shaft groove side wall smaller than the rectangular seal ring, and optimizing the V-shape lubrication groove geometry enables lubrication on the sliding surface, achieving low-torque and low-wear properties.

The material of this developed product is Bearee PK5301, which is based on PEEK resin with a special filler blended in.

Table 1 shows a comparison of the developed V-groove seal ring with the rectangular and trapezoidal seal rings. The V-groove seal ring has a good performance balance and the following advantages against the rectangular seal ring (NTN conventional product).

(Features)

- (1) 60% lower torque
- (2) 1/10 wear
- (3) Equivalent low oil leakage

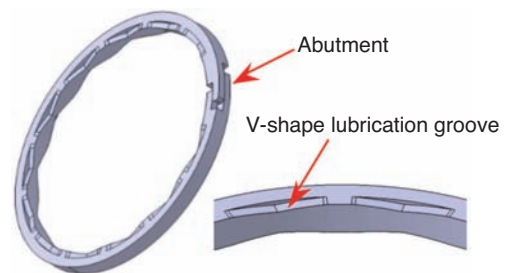


Fig. 3 Groove geometry of low torque seal ring

Table 1 Comparison of features various seal rings

Item	Rectangular seal ring	Trapezoidal seal ring	V-groove seal ring
Cross-section shape	Rectangular	Trapezoidal	Rectangular
Partial cross-section diagram			
Side surface lubrication groove	None	None	V-shape
Contact with shaft groove side wall	Full surface contact	Line contact	Full contact other than groove area
Torque	△	◎~△	○
Oil leakage	◎	△	◎
Wear properties	○	△	◎
Performance balance	○	△	◎

◎ : Excellent ○ : Good △ : Fair

4. Performance of V-groove seal ring

4.1 Test seal rings

NTN has tested three types of seal rings, as shown in **Table 2**, to verify the performance of the V-shape lubrication groove. Since the lubrication groove section of the V-groove seal ring does not make contact with the shaft groove side wall, the torque is lower than the rectangular seal rings, similar to the trapezoidal seal rings. In addition, the V-shape lubrication groove improves torque and anti-wear properties compared with the other lubrication groove geometries. Therefore, in order to verify the difference of the groove geometries, NTN also evaluated square-groove seal rings with square lubrication grooves with the same contact area to the shaft groove side wall as the V-groove seal ring.

Table 2 Test seal rings

Test seal ring	Geometry of side surface lubrication groove	
V-groove seal ring	V-shape	
Square-groove seal ring	Square-shape	
Rectangular seal ring	— (No groove)	

Seal ring size: OD 50 mm, Thickness: 1.6 mm, Width: 1.5 mm

4.2 Test machine and conditions

Fig. 4 shows an overview of the test machine which evaluates torque, oil leak and wear.

Pressure was applied while supplying oil between two seal rings mounted on the shaft grooves and rotating the housing. Torque and oil leakage were evaluated during this operation. **Table 3** shows the materials of the seal rings, housing and shaft.

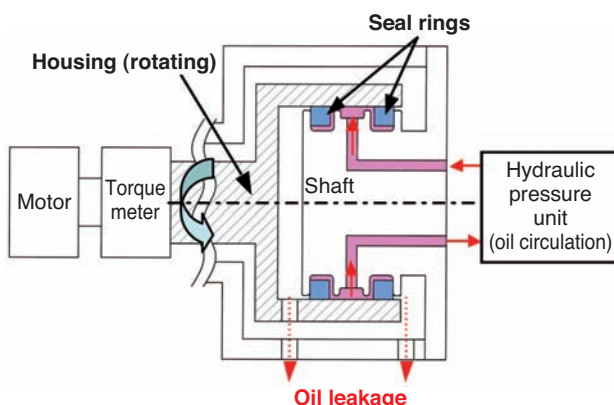


Fig. 4 Test machine

Table 3 Material of test pieces

Test piece	Material
Seal ring	PEEK resin (Bearee PK5301)
Housing	S45C
Shaft	S45C

4.3 Torque

4.3.1 Dependency on hydraulic pressure

Torque (for two seal rings) was evaluated under the varying hydraulic pressure test conditions shown in **Table 4**. **Fig. 5** and **6** show the relationship between hydraulic pressure and torque.

The torque of the V-groove seal rings was approximately 60 to 70% lower than that of the rectangular seal rings in any rotation speed and hydraulic pressure, and dependency on the hydraulic pressure was also relatively low. With V-groove seal rings, the higher the hydraulic pressure, the more oil enters onto the sliding surface from the lubrication groove. Therefore, the torque dependency on hydraulic pressure is considered to be smaller.

From the groove geometry standpoint, the V-groove seal rings showed about 20% lower torque than that of the square-groove seal rings.

Table 4 Test condition

Item	Description
Hydraulic pressure	0.5~2.0MPa
Rotation speed	4,000min ⁻¹ or 7,000min ⁻¹
Lubricating oil	ATF (temperature: 110°C)

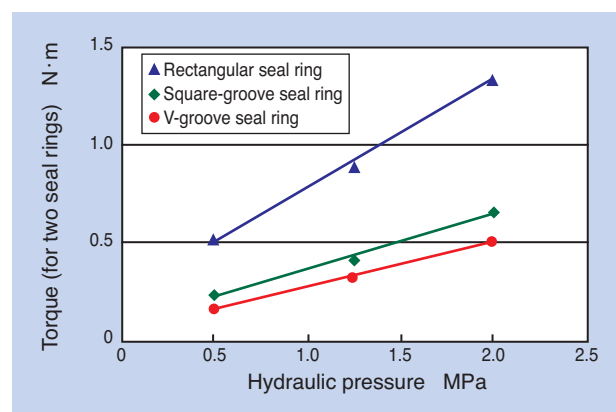


Fig. 5 Torque versus oil pressure (4,000min⁻¹)

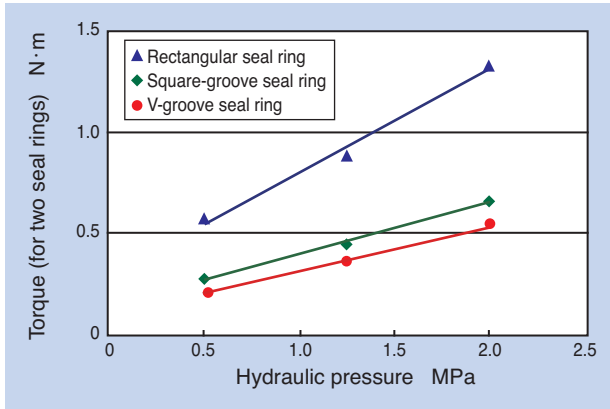


Fig. 6 Torque versus oil pressure (7,000min⁻¹)

4.3.2 Dependency on oil temperature

Torque (for two seal rings) was evaluated under the varying oil temperature test conditions shown in Table 5. Fig. 7 shows the relationship between oil temperature and torque. The torque of the V-groove seal rings is lower than that of the rectangular seal rings by 60% at any temperature. From the groove geometry standpoint, the V-groove seal rings showed about 20% lower torque than that of the square-groove seal rings.

Table 5 Test condition

Item	Description
Hydraulic pressure	2.0MPa
Rotation speed	4,000min ⁻¹
Lubricating oil	ATF (temperature: 30-150°C)

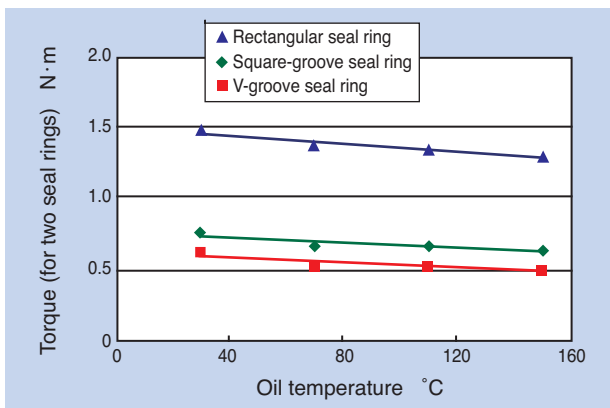


Fig. 7 Torque versus oil temperature

4.4 Oil leakage

V-groove seal rings and rectangular seal rings were evaluated for oil leakage under the varying temperature test conditions shown in Table 6. Fig. 8 shows the relationship between oil temperature and oil leakage. The decrease of lubricating oil viscosity along with the rise of temperature causes oil leakage to increase. The oil leakage of the V-groove seal rings was very small compared to that of the rectangular seal rings.

Table 6 Test condition

Item	Description
Hydraulic pressure	2.0MPa
Rotation speed	4,000min ⁻¹
Lubricating oil	ATF (temperature: 30-150°C)

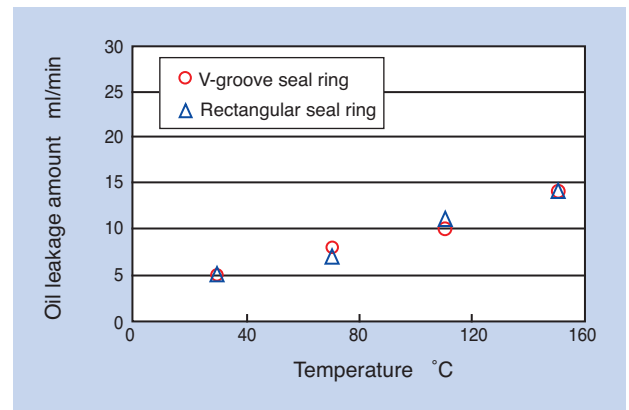


Fig. 8 Oil leakage versus oil temperature

4.5 Wear properties

Wear of seal rings was measured under the high pressure, high speed and high temperature test conditions shown in Table 7. Fig. 9 shows the wear of the side walls of the seal rings.

Wear on the low-torque V-groove and square-groove seal rings with lubrication grooves was smaller than that of the rectangular seal rings.

Also, the V-groove seal rings showed lower wear between two different groove geometries at 1/10 that of the rectangular seal rings.

The addition of a lubrication groove improves the lubrication of the sliding surface and reduces wear. It can be seen that the groove geometry for lower torque results in lower wear as well.

Table 7 Test condition

Item	Description
Hydraulic pressure	3.0MPa
Rotation speed	7,000min ⁻¹
Lubricating oil	ATF (temperature: 150°C)
Time	1h

Table 8 Analysis condition

Item	Description
Sliding area	Only on shaft groove side wall
Oil film thickness	5μm
Shaft rotation speed	4,000min ⁻¹
Hydraulic pressure	2MPa
Oil temperature	20°C

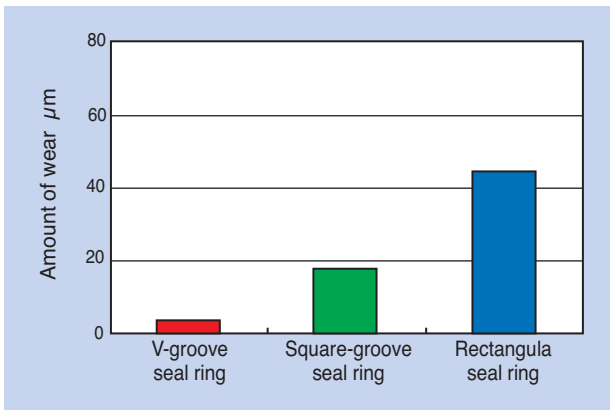


Fig. 9 Wear of test seal rings

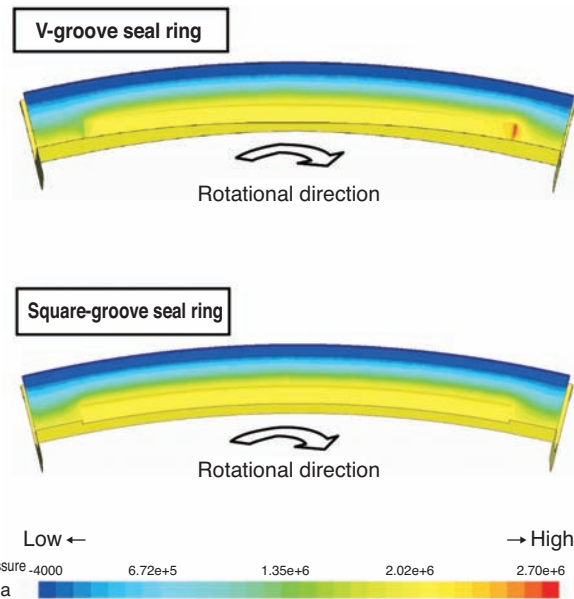


Fig. 10 Static pressure distributions of sliding width slide surfaces

4.6 Fluid analysis

The test confirmed that the developed V-shape groove of the V-groove seal rings was effective in reducing torque. This result is due to the reduced contact area with the shaft groove side wall and improved lubrication of the sliding surface by addition of the lubrication grooves. The torque difference due to groove geometry was assumed to be caused by different lubrication conditions. In order to prove this theory, NTN extracted and modeled the fluid pattern of one lubrication groove for the V-groove seal ring and square-groove seal ring and conducted a fluid analysis.

Table 8 shows the analysis condition and **Fig. 10** shows the analysis result. The ends of the V-shape groove of the V-groove seal ring show high pressure due to hydrodynamic effects. This force is in the opposite direction of the hydraulic pressure applied to the seal ring which pushes on the shaft groove side wall, contributing to the reduction of pressure on the contact surface. In addition, it facilitates oil supply from the ends of the lubrication groove to the sliding surface, which contributes to lower torque. On the other hand, high pressure similar to the V-shape groove is not shown at the ends of the square-groove seal ring. Thus the different lubrication groove geometries resulted in the experienced torque differences.

5. Summary

NTN has developed V-groove seal rings which reduced oil leakage and significantly improved the torque and wear properties of the rectangular seal rings. They are currently being evaluated by automotive and transmission manufacturers and NTN believes they will contribute to low fuel consumption.

NTN strives to continue with development of lower torque and longer life products by applying this lubrication groove design technology to bearings and other units used in fluid lubrication.

References

- 1) Yutaka HAYASHI, Jiro MATSUMOTO, Noboru UMEMOTO: Introduction of Engineering Plastic Seals, NTN TECHNICAL REVIEW No. 65 (1996) 54.
- 2) Yoshio OKI, Takumi HAYASHI, Takuya ISHII: Characteristics and Applications of Super Engineering Plastics, Journal of Japanese Society of Tribologists 49 (7), (2004) 31

Photo of authors



Kouzou KAKEHI
Engineering Dept.
NTN Engineering Plastics Corp.



Takumi KONDOU
Engineering Dept.
NTN Engineering Plastics Corp.



Takuya ISHII
Composite Material Engineering Dept.
Composite Material Products Division



Masato YOSHINO
Advanced Technology
R&D Center

The Introduction of Sintered New Products for Automobile

Tomonori YAMASHITA*
Tomokazu SONOZAKI**



The sintered machine part becomes high-strength, and the adoption of the automobile use increases recently. A sintered part had characteristic that it could produce the parts of a complicated shape with high productivity, but securing of strength of the part was difficult to have the porous compared to cast alloy. Therefore, NTN reviewed the material and process of forming and sintering at first, and developed that raises the strength of sintered

materials by doing it densely. In addition, NTN introduces about the sintered materials for the special environment as corrosion environment or keeping away lubricant.

1. Introduction

The use of sintered machine parts in vehicles has grown in recent years. Domestic production grew by 20% from approximately 70,000 tons in 1998 to 84,000 tons in 2012. Total weight of sintered parts in a vehicle also grew by 50% from approximately 6 kg in 1998 to approximately 9 kg in 2011¹⁾. In this article, we would like to introduce high-density and high-strength sintered machine parts which can be used in a variety of vehicle applications along with sintered bearings, which can be used in corrosive or poorly lubricated environments.

2. High-density/high-strength sintered materials

Sintered materials are used in automotive applications in engine and drivetrain components where high strength is required in addition to high reliability and quality are required. In this section, we will describe the development of high-density and high-strength sintered materials.

2.1 High-strength sintered materials by high-density process

Sintered compacts, which contain internal pores, have inferior mechanical properties compared to the materials made by the melting and forging cast process. Therefore, various methods for strengthening sintered materials by increasing density are being proposed.

Fig. 1 shows the relation between density and cost of

the representative methods.

Powder forging, shown in **Fig. 1**, is a method to increase the density of sintered compacts by hot forging with the intent of completely eliminating the internal pores. Copper infiltration is a method wherein the internal pores of sintered compacts are filled with melted copper. Warm compacting is a method to increase the density by heating the powder and mold and using a special lubricant. These conventional high-density methods listed require special processes which lead to higher costs.

Therefore, we aimed for obtaining high-density sintered compacts with a similar method as the ordinary sintering process of the past. This was done by optimizing manufacturing conditions, such as material composition, forming conditions, heat treatment, etc.

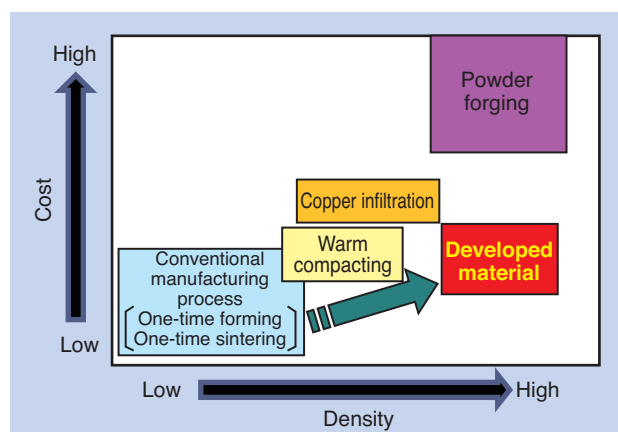


Fig. 1 Relationship between density and costs

*Engineering Dept. NTN Powder Metal Corporation

**Composite Material Engineering Dept, Composite Material Products Division

and high-density/high-strength sintered materials were developed.

2.2 Mechanical properties

Fig. 2 shows the relation between the density of various materials, including the developed material, and Young's modulus. The density of the developed product is 7.5 g/cm³. This achieves more than 95%, in true density ratio, of the density of iron, which is 7.85 g/cm³. Young's modulus is 180 - 190 GPa, which is equivalent to high carbon chromium bearing steel, SUJ2. Adding cold working further increases both density and Young's modulus.

Fig. 3 shows the radial crushing strength. Radial crushing strength is obtained by the following equation, applying compressive stress on the annular test piece, as shown in **Fig. 4**. The developed material showed a radial crushing strength of 2,000 MPa or more, compared to 1,300 MPa of the conventional high-density materials.

$$K = \frac{F(D-e)}{L \cdot e^2}$$

K : Radial crushing strength (MPa)
F : Maximum load when the test piece is destroyed (N)
L : Length of hollow circular cylinder (mm)
D : Outer diameter of hollow circular cylinder (mm)
e : Wall thickness of hollow circular cylinder (mm)

Fig. 5 shows the fatigue limit of the developed material obtained from the ring compression fatigue test. The ring compression fatigue strength is obtained from a test of finding the fatigue limit by repeating a load of stress ratio 0.1 (the ratio between the maximum and minimum compression load is 10:1) on the annular test piece, as shown in **Fig. 6**. The result of the ring compression fatigue test is, in general, experimentally known to be around 0.8 times the fatigue strength obtained by the ordinary bending fatigue test.

The fatigue limit of the developed material is 300 MPa, about twice the fatigue limit of the conventional high-density material of 150 MPa.

Therefore, the developed material can be used in areas with a high repetitive load, where the conventional sintered parts could not be used.

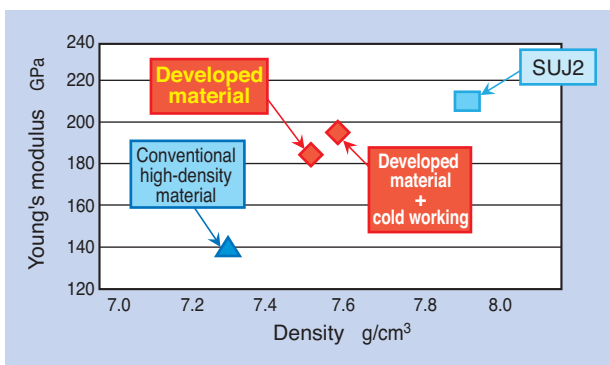


Fig. 2 Relationship between density and Young's modulus

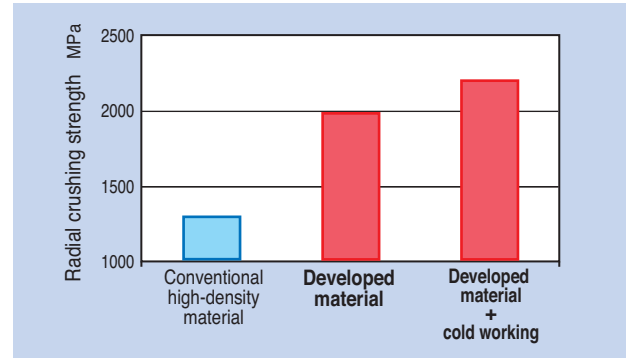


Fig. 3 Radial crushing strength

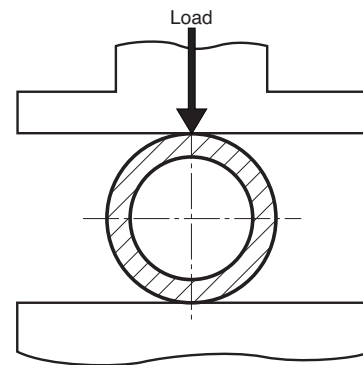


Fig. 4 Method for radial crushing strength test

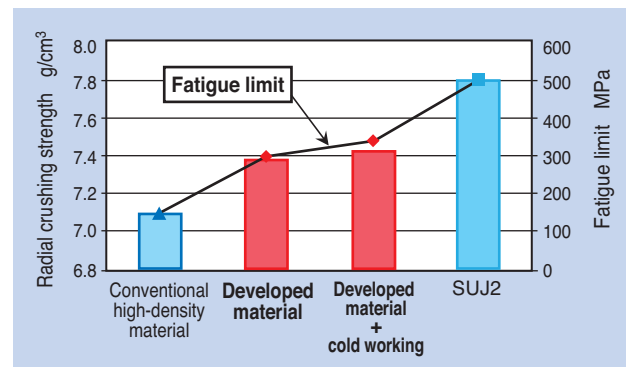


Fig. 5 Density and fatigue limit

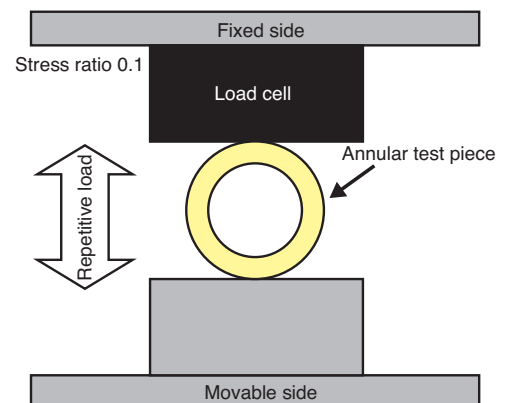


Fig. 6 Method for fatigue limit

3. Corrosion resistant sintered bearings

In general, bronze series sintered bearings are used for motor-based fuel pumps of automobiles. Corrosion by sulfur and organic acid contained in the fuel has recently been observed in the conventional bronze series sintered bearings due to the use of inferior quality fuel used mainly in developing countries. To cope with this issue, cupronickel-based sintered bearings with superior corrosion resistance are used. However, this material is very expensive as it contains nickel.

This led to the development of the less costly sintered bearings, adopting aluminum bronze as the material, which has equivalent or better corrosion resistance as the cupronickel material.

3.1 Features and challenges of aluminum bronze

Although aluminum bronze exhibits superior corrosion resistance, it was considered inadequate for the sintering process of powder metallurgy because of surface oxidation under high temperature. It also has a higher friction coefficient than the ordinary bronze series material.

To solve this issue, the material composition and manufacturing method were optimized, especially the sintering method to improve its properties. This achieved aluminum bronze with corrosion resistance equivalent to or better than that of the cupronickel material. In addition, friction and anti-wear properties were significantly improved by optimizing the blending of graphite.

3.2 Corrosion resistance

Table 1 shows the test results of corrosion resistance against organic acid and sulfur. Cupronickel material was also tested for comparison purposes.

<Test conditions>

- (1) Corrosion resistance test against organic acid
 - Test fluid: Organic acid with 2% concentration
 - Temperature: 50°C
 - Test time: 100 hours
- (2) Corrosion resistance test against sulfur
 - Test fluid: Gasoline with 300 ppm of sulfur
 - Temperature: 80°C
 - Test time: 300 hours

Test pieces were immersed in the test fluid at the set temperature and left for the predetermined time. The rate of weight change was calculated from the weight difference before and after the test.

Table 1 Result of corrosion resistance test

	Rate of weight change %	
	Developed material	Cupronickel material
(1) Corrosion resistance against organic acid	0.14	0.15
(2) Corrosion resistance against sulfur	0.10	0.40

The test results showed that the developed material was equivalent in corrosion resistance against organic acid and superior in corrosion resistance against sulfur.

3.3 Friction/wear properties

Table 2 shows the friction coefficient and specific wear amount.

<Test conditions>

- (1) Friction test
 - Load: 35N
 - Rotation speed: 3,160 min⁻¹
 - Test piece size: ID 5 × OD 10 × Width 7 mm
 - Opposite material: SUS304
 - Test time: 30 min.
- (2) Wear test
 - Load: 64N
 - Rotation speed: 3,000min⁻¹
 - Test piece size: ID 6 × OD 12 × Width 6 mm
 - Opposite material: SUS304
 - Test time: 500 hours

The friction coefficient of the developed material was equivalent to that of the cupronickel material. On the other hand, the specific wear amount of the developed material was about 1/10 that of the cupronickel material.

This shows that the developed material has a more superior anti-wear property than the cupronickel material, thus making it a suitable replacement for the latter.

Table 2 Friction coefficient and specific wear rate

	Developed material	Cupronickel material
Friction coefficient	0.14	0.14
Specific wear rate m ³ /(N · m)	3.2×10 ⁻¹³	30.0×10 ⁻¹³

4. Self-lubricating sintered bearings

Sintered oil retaining bearings for automobiles and office equipment may be used in environments with high temperatures or enclosed by a cover, etc. In this case, lubricant oil retained in the bearings may evaporate and contaminate the surroundings. The developed self-lubricating sintered bearings use special graphite as the solid lubricant and are applicable in high temperature environments where oil cannot be used.

Regular graphite is inferior to other kinds of metal powder in fluidity; however, increasing the additive amount causes inferior compactibility preventing formation of complex shapes and low green compact strength.

Therefore, the metal powder mixture was changed to adopt high-fluidity special graphite in an increased

amount. This achieved the development of self lubricating sintered bearings with excellent sliding and anti-wear properties even when lubricant oil is not used, while maintaining high productivity (Fig. 7).

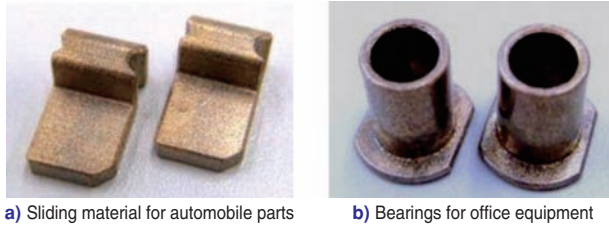


Fig. 7 Self-lubricating BEARPHITE

4.1 Structure and features of self lubricating materials

Special graphite with improved fluidity was used as the self lubricating material. The amount of graphite was also increased by 5 times the regular bronze material, which was done by optimizing the blend ratio of the material powder. Table 3 shows the chemical composition of the developed material and regular bronze series material.

Table 3 Chemical component of self-lubricating BEARPHITE

Material	Chemical composition %		
	Cu	Sn	C
Developed product	Remainder	7~11	4~17
Bronze Series	Remainder	7~11	1~12

4.2 Friction/wear properties

Table 4 shows the friction coefficient and specific wear amount without oil content.

Table 4 Friction coefficient and specific wear rate

	Developed material	Cupronickel material
Friction coefficient	0.2~0.3	0.45
Specific wear rate $m^3/(N \cdot m)$	0.8×10^{-14}	2.9×10^{-14}

<Test conditions>

(1) Friction test

- Load: 98N
- Rotation speed: 1,000min⁻¹
- Test piece size: ID 6 × OD 12 × Width 6 mm
- Shaft material: SUJ2
- Test time: 90min.

(2) Anti-wear test

- Load: 15N
- Rotation speed: 450min⁻¹
- Test piece size: ID 6 × OD 12 × Width 6 mm
- Opposite material: SUJ2
- Test time: 1 hour

The friction coefficient of the self lubricating bearings were approximately half that of the bronze series without oil content. The specific wear amount was also about 1/3, showing an excellent anti-wear property. This means they can be used in areas where an anti-wear property is required without oil content.

5. Summary

In this article, the newly developed high-density/high-strength sintered machine parts for automobiles and sintered bearings for special environments were introduced.

We will promote marketing of the developed products introduced in this article, along with continuing development of higher functionality.

[High-density/high-strength sintered material]

- Achieved true density ratio of 95% to iron and Young's modulus equivalent to SUJ2
- Approximately 1.5 times radial crushing strength and 2 times fatigue limit compared with the conventional high-density sintered materials

[Corrosion resistance sintered bearings]

- Equivalent or better corrosion resistance and friction coefficient and around 1/10 of specific wear amount of the cupronickel sintered bearings

[Self lubricating sintered bearings]

- Approximately 1/2 the friction coefficient and approximately 1/3 the specific wear amount compared to the bronze series sintered bearings without lubricant content

References

- 1) Sokeizai Center, Monthly Bulletin "Sokeizai" May 2013 Vol. 54, No. 5 Special Issue, Sokeizai Yearbook 2012

Photo of authors



Tomonori YAMASHITA
Engineering Dept.
NTN Powder Metal Corporation

Tomokazu SONOZAKI
Composite Material Engineering Dept.
Composite Material Products Division

Rolling Contact Fatigue Life of Highly-carbonitrided JIS-SUJ2

Daisuke SATO*
Chikara OHKI*



Carbonitriding for rolling bearings has been known to prolong rolling contact fatigue lives under both clean and debris contaminated lubrication conditions. However, a relationship between surface nitrogen concentrations and RCF lives has not yet been clarified. To this end, we prepared carbonitrided rolling bearings with various concentrations of

surface nitrogen. The kind of steel was JIS-SUJ2 (52100 and 100Cr6 equivalent). We conducted three types of RCF tests; (1) with Rockwell indentations on the inner ring raceways, (2) with oil containing hard steel particles, and (3) with clean oil. Test (1) emulates to evaluate RCF lives under debris contaminated conditions. Test (1) exhibited the following results; the average RCF life of 0.4 mass % surface nitrogen concentration was about 2 and 3 times longer than that of conventional carbonitrided and nitrogen free, respectively. Both tests (2) and (3) also demonstrated that an RCF life with 0.4 mass % surface nitrogen concentration was longer than that of the others. Hence, it has been proven conclusively that carbonitriding with high surface nitrogen concentrations brings about excellent bearing performances.

1. Introduction

The impact of the carbonitriding process to subsurface initiated flaking life¹⁾ of rolling bearings has been known for a long time by the study of Kurabe, et al. It was also recently confirmed, by Dommarco, et al. about the longevity effect by an increased amount of retained austenite^{2), 3)}. For rolling bearings used in the transmission, hub and reducer of automobiles, service life in contaminated lubrication (hereafter, surface initiated flaking life) is critical. It is known that the carbonitriding process with an increased amount of retained austenite is effective under this condition, as well^{4), 5)}. On the other hand, a life test of SUJ2 material with strict control of surface nitrogen concentration has only been conducted by Ohki, for the surface initiated flaking life⁶⁾ and no other data has been reported, yet.

In this report, we are introducing various evaluation results of SUJ2 material with strict control of surface nitrogen concentration. We have evaluated surface initiated flaking life, lubrication life of clean oil and indentation resistance, which are critical properties for the rolling bearings.

2. Surface initiated flaking life test

2.1 Bearing life test under artificially-applied indentation

A bearing life test with artificial indentations (hereafter, artificial indentation life test) is conducted by forming artificial indentations on the raceway of the inner ring of the bearings, in advance, with clean lubrication and is an effective method to appropriately determine the surface initiated flaking life⁶⁾.

2.1.1 Types and materials of bearings

We used deep-groove rolling bearings (bearing number: 6206, $d = 30$ mm, $D = 62$ mm, $B = 16$ mm, $Z = 9$) as test pieces. **Table 1** shows the chemical composition of JIS SUJ2, the material of the raceway ring. The carbonitriding process of the inner ring was conducted while monitoring partial pressure of CO and CO₂, as well as undecomposed NH₃ with an infrared analyzer.

Since the outer ring with no indentations will always have longer life than the inner ring, the carbonitriding process was not applied, but only ordinary quenching and tempering. The heating temperature was set to 850°C for both and the tempering was conducted at a

*Advanced Technology R&D Center

temperature of 180°C for two hours.

After randomly selecting one test piece each from among the pieces of ordinary quenching and carbonitriding process, the carbon and nitrogen concentration distribution at the center of the bottom of the raceway of the inner ring was measured using the line analysis of the electron probe micro analyzer (EPMA). Fig. 1 shows the results. Based on the nitrogen concentration distribution, material was removed from the surface of the inner ring raceway to achieve the target surface nitrogen concentration level. The radial clearance of the test bearings was set to be identical by adjusting the outer ring groove diameter.

Table 2 shows the measurement results for retained austenite by X-ray diffraction. On the table, “0.4 mass % N” and “0.1 mass % N” mean the test pieces with the surface nitrogen concentration of 0.4 mass % and 0.1 mass %, respectively, after machining the test pieces.

The order of the test pieces with a high retained austenite amount was the same as the order of test pieces with a high concentration of nitrogen.

Fig. 2 shows the cross-sectional hardness distribution of the test pieces after heat treatment. There was no significant variation in the cross-sectional hardness within the range of the heat treatment conditions in this test. From the above, we concluded that the key differences among these test pieces are surface nitrogen concentration and the retained austenite amount.

2.1.2 Test method

The subject of the test is the artificial indentations formed at the center of the bottom of the inner ring raceway. These indentations were formed by pressing a Rockwell hardness testing penetrator made of conical diamond with a force of 196N. A total of 30 indentations were equally spaced 12° apart per inner ring.

Table 1 Chemical compositions of JIS-SUJ2 used (mass%)

C	Si	Mn	P	S	Ni	Cr	Mo	Cu	Al	Ti (ppm)	O (ppm)
0.99	0.24	0.40	0.012	0.006	0.06	1.36	0.03	0.10	0.011	0.24	0.04

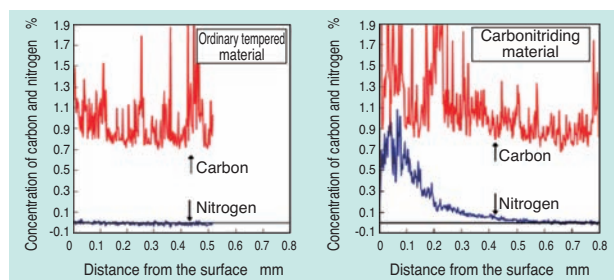


Fig. 1 Carbon and Nitrogen concentration distribution profiles after heat treatment

The size of the indentations was about 200 μm in diameter and 15 μm in depth.

Fig. 3 shows the schematic drawing of the life tester. This structure allows the application of a radial load evenly onto two test bearings. Table 3 shows the test conditions. An oscillation monitor was used for detecting flaking. The oscillation acceleration of normal operation was 1.5 m/s². Therefore, it was determined flaking had occurred when it reached 6 m/s², four times the normal operation, and the test was terminated.

Table 2 Retained austenite measured by X-ray diffraction

Material	Retained austenite amount at 0.05 mm deep from scraped surface (%)
0.4mass%N	29.6
0.1mass%N	20.1
Ordinary tempered material	9.0

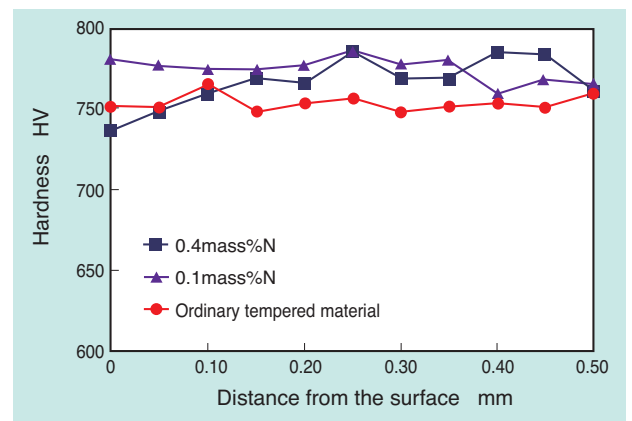


Fig. 2 Hardness distribution profiles

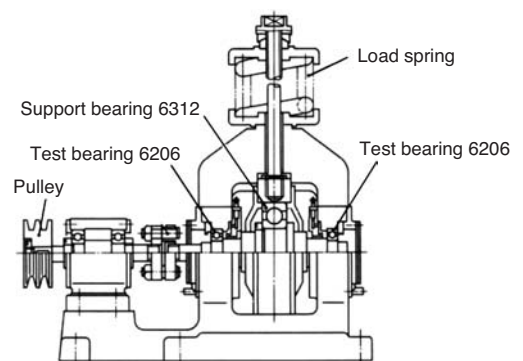


Fig. 3 Schematic drawing of rolling contact fatigue life tester for ball bearing

Table 3 Test conditions of artificial indentation life test

Radial load kN	6.86
Radial internal space μm	20
Contact pressure P _{max} GPa	3.1
Rotational speed of inner ring min ⁻¹	3,000
Lubricant oil	Turbine oil (VG56)
Calculated life h	127.6

2.1.3 Test results

The life in this test was obtained assuming that it followed the two-parameter Weibull distribution function of the Lundberg-Palmgren theory ⁷⁾. Fig. 4 shows the Weibull distribution of the artificial indentation life test and Table 4 shows the test results. In terms of L_{50} life, the SUJ2 ordinary quenching material showed 69.0 h, the 0.1 mass% N material showed 121.3 h and the 0.4 mass% N material showed 223.7 h. This indicates that the higher the surface nitrogen concentration, the longer the life, both for L_{10} and L_{50} .

This test corresponds to the follow-up test of the previous report ⁶⁾. Similar to the previous report, it was verified that the surface initiated flaking life could be extended with high nitrogen concentration.

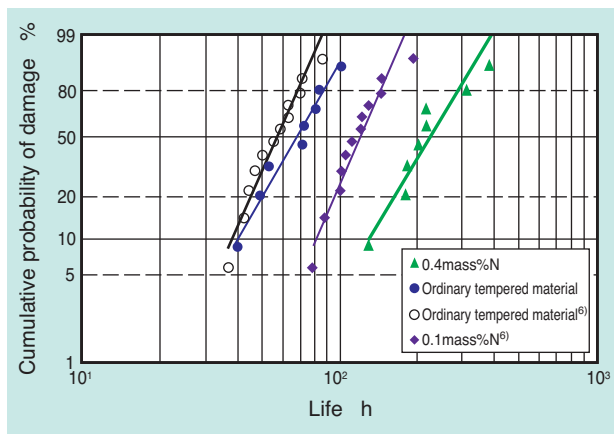


Fig. 4 Weibull distributions of artificial indentation life test

Table 4 Results of artificial indentation life test

Material	Number of test pieces	L_{10} life	L_{50} life	Weibull slope
0.4mass%N	8	119.9	223.7	3.5
0.1mass%N ⁶⁾	12	81.7	121.3	4.8
Ordinary tempered material	12	40.6	69.0	3.6

2.2 Contaminated lubrication life test

The artificial indentation test mentioned above verified that the surface initiated flaking life of SUJ2 material with high surface nitrogen concentration could be extended. In order to verify if the same trend can be obtained even in actual contaminated lubricant, we conducted a contaminated lubrication life test, which is the conventional test method of the surface initiated flaking life. In addition, we also compared performance with the conventional SCr420 carbonitriding material.

2.2.1 Types and materials of bearings

We used tapered roller bearings (bearing number: 30206, $d = 30$ mm, $D = 62$ mm, $T = 17.25$ mm, $Z = 17$) as test pieces. The surface nitrogen concentration of the raceway and rolling elements of the 0.4 mass % N test piece after the machining process was all 0.4 mass %. Off-the-shelf product was used as the SCr420 carbonitriding test piece.

2.2.2 Test method

Fig. 5 shows the schematic drawing of the life tester. This structure allows the application of a radial and axial load evenly onto two test bearings. Table 5 shows the test conditions. The test was conducted by applying a predetermined load on the test bearings, injecting approximately 30 ml of contaminated oil into the housing and rotating the inner ring of the bearings at 2000 rpm. The detection method of flaking was the same as the artificial indentation life test in 2.1.2.

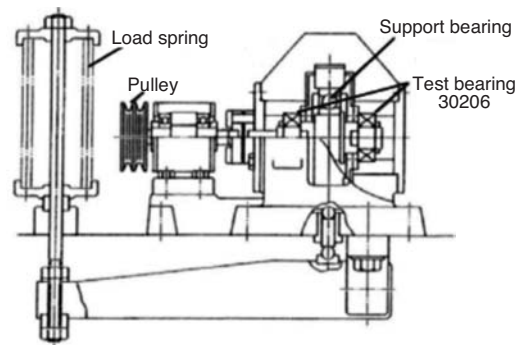


Fig. 5 Schematic drawing of rolling contact fatigue life tester for tapered roller bearing

Table 5 The conditions of life test under contaminated lubrication

Load kN	F_r	17.64
	F_a	1.5
Contact pressure P_{max} GPa		2.5
Rotational speed of inner ring min^{-1}		2,000
Lubricant		Turbine oil (VG56) Oil supply, approx. 30 ml
Amount of contamination		1.0 g/L
Type of contamination		Gas-atomized powder equivalent to KHA30 Size: 108 - 180 μm Hardness: similar to HV800
Calculated life h		168.8

2.2.3 Test results

Fig. 6 shows the Weibull distribution of the test results. Table 6 shows the test results. In terms of L_{50} life, the conventional SCr420 carbonitriding material showed 37.5h, SUJ2 ordinary quenching material showed 70.3 h and the 0.4 mass % N material showed 149.1 h. Similar to the artificial indentation life test, it was revealed that life could be extended by applying the carbonitriding process to the inner/outer rings and rolling elements. It is noted that the bearings with a surface nitrogen concentration of 0.4 mass % had a comparable service life in contaminated lubricant to that of the calculated life of the SUJ2 ordinary tempered material in clean lubrication.

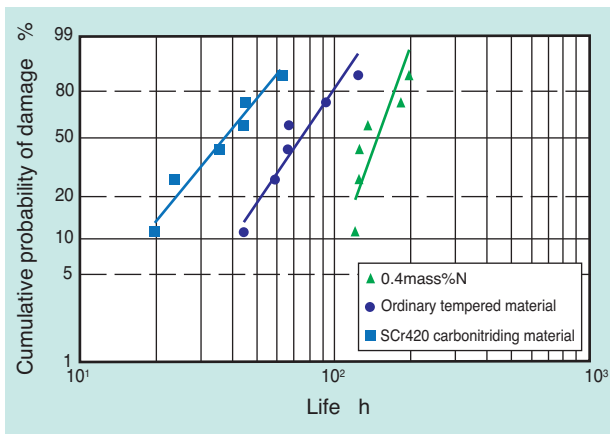


Fig. 6 Weibull distributions of life test under contaminated lubrication

Table 6 Results of life test under contaminated lubrication

Material	Number of test pieces	L_{10} life	L_{50} life	Weibull slope
0.4mass%N	6	107.7	149.1	5.8
Ordinary tempered material	6	44.0	70.3	4.0
SCr420 carbonitriding material	6	17.7	37.5	2.5

Note) The ordinary tempered material comes from a separate lot

3. Life test in clean lubrication

From the test result mentioned above, it was revealed that the indensurface initiated flaking life can be extended by increasing the surface nitrogen concentration. However, it is necessary to verify longevity in clean lubrication as the bearings are mostly used in the clean lubrication environment without contamination.

3.1 Types and materials of bearings

The same test bearings as in Section 2.2 were used.

3.2 Test method

The tester in Fig. 5 was used. Table 7 shows the test conditions of the life test in clean lubrication. The test was conducted applying a predetermined load on the test bearings, supplying oil in the housing and rotating the inner ring at 2000 rpm.

3.3 Test results

The result of 7 test pieces of 0.4 mass% N showed no flaking after 7300 hours. Fig. 7 shows the Weibull distribution. Arrows indicate suspension.

The relation between the suspended time and L_n life is indicated in Eq. (1) ⁸⁾.

$$L_n = T \left\{ \frac{\ln(1-0.01C)}{N \ln(1-0.01n)} \right\}^e \dots\dots\dots (1)$$

Setting the target life to L_{10} and confidence level to 90%, substituting termination time T of 7300h, the number of test pieces N of 7, $n=10$, Weibull slope e of $9/8$ ⁹⁾, which is a typical value for rolling bearings, to the formula (1), we obtained L_{10} life is 2600 h or more with 90% reliability. This is 15 times longer than the calculated life under clean lubrication, and is considered to be sufficient.

Table 7 The conditions of life test under clean lubrication

Load kN	F_r	17.64
	F_a	1.5
Contact pressure P_{max} GPa		2.5
Rotational speed of inner ring min^{-1}		2,000
Lubricant		Turbine oil (VG56)
Calculated life h		168.8

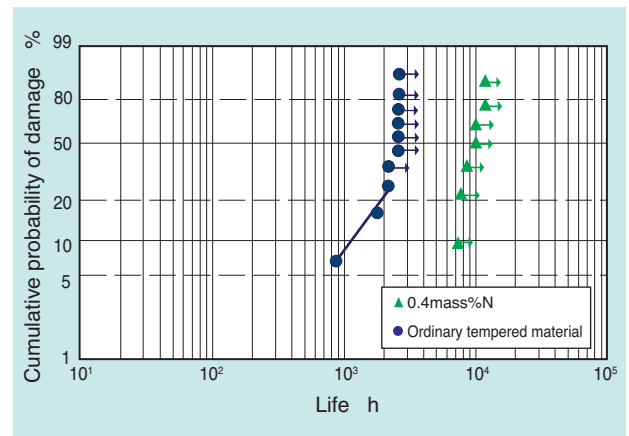


Fig. 7 Weibull distributions of life test under clean oil

4. Indentation formation test

All the results so far revealed that the surface initiated flaking life and clean lubrication life can be extended by increasing the surface nitrogen concentration. Next, we conducted an indentation formulation test, which is to evaluate the depth of indentation formed by an impression of a ceramic ball onto the test piece at a certain pressure in order to evaluate the static-load-carrying capacity.

The size of indentation in this test is very small with a depth typically 1 μm or less, unlike the artificial impressions mentioned earlier, formed with stress equivalent to yield stress.

4.1 Shape of test piece and test method

Fig. 8 shows the shape of the test piece. The indentation is formed by pressing a silicon nitride ceramic ball of 9.525 mm in diameter onto the mirror-finished test piece surface. The depth of the indentation was measured with a three-dimensional surface shape measuring device.

4.2 Test results

Fig. 9 shows the relation between the maximum contact pressure and the depth of the indentation of each test piece. In this test, tempering temperature was also changed in addition to the surface nitrogen concentration.

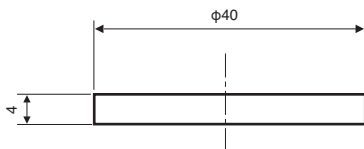


Fig. 8 Shape of test piece with indentation

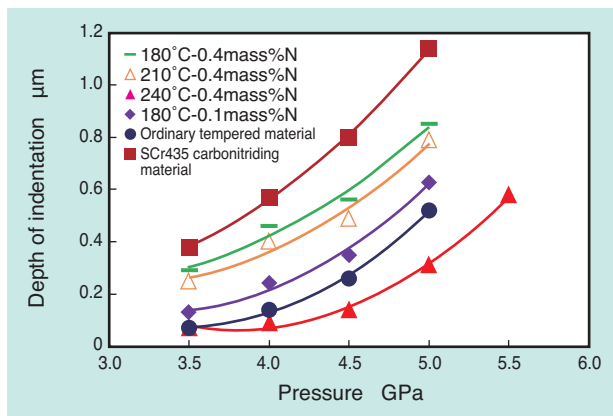


Fig. 9 Relation between maximum contact pressure and depth of indentation

In the figure, for example, “240°C-0.4 mass % N” means that the tempering temperature is 240°C and the surface nitrogen concentration after finishing work is 0.4 mass %. The depth of indentation for 180°C 0.4 mass % N is less than SCr435 carbonitriding material. This is presumed to indicate an increase in the static load-carrying capacity.

The depth of indentation tends to be less when the tempering temperature is high and more when the surface nitrogen concentration is high. In general, the indentation becomes deeper when nitrided; however, we have discovered that if tempered at 240°C after nitriding, the depth of indentation becomes less than the ordinary SUJ2 quenching material.

5. Consideration

5.1 Life test

This study revealed that the surface initiated flaking life and the clean lubrication life can be extended by applying a high nitrogen concentration on SUJ2. In this section, we consider the main factors that contributed to the extension of surface initiated flaking life of the 0.4 mass % N materials. The increased amount of retained austenite and solid solution strengthening of nitrogen can be considered as the factors. In order to confirm the impact of these factors to the life of the bearings, we conducted an artificial indentation life test with the high nitrogen concentration 240°C 0.4 mass % N material with the equivalent amount of retained austenite as the ordinary SUJ2 quenching material, and the ordinary quenching 240°C tempering material with 1/2 or less of retained austenite as the ordinary SUJ2 quenching material.

L_{10} life of the 240°C 0.4 mass % N material was 47.4 hours and L_{50} life was 87.7 hours, which are equivalent or slightly longer than the ordinary SUJ2 quenching material. L_{10} life of the ordinary quenching 240°C tempering material was 17.5 hours and L_{50} life was 46.0 hours, which are shorter than the ordinary SUJ2 quenching material. From these results, it is considered that the retained austenite amount, as well as the solid solution strengthening of nitrogen affect the surface initiated flaking life.

5.2 Prediction of the depth of indentation

Bearings may withstand instantaneous excessive load if the material is resistant to indentation, even when a heavy load is applied. Therefore, we explored design guidelines for bearing material that withstand heavy load by understanding the relation between the material properties and the depth of indentation.

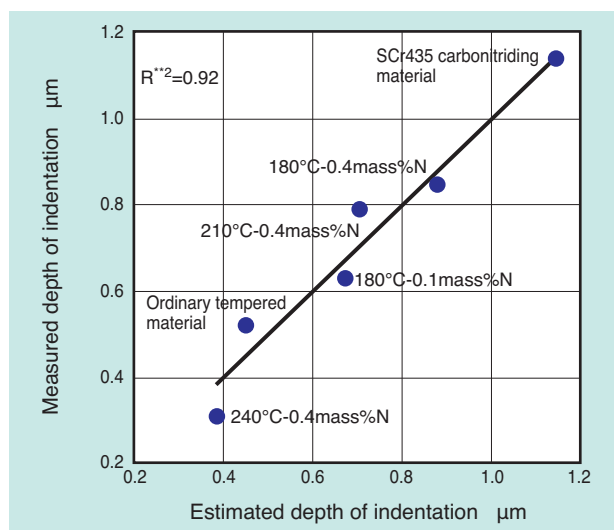
A silicon nitride ceramic ball of 9.525 mm in

Table 8 Depth and material properties of various test pieces

Material	Depth of indentation (actual measurement)	Retained austenite (vol%)	Average crystal grain diameter (μm)	Surface nitrogen concentration (mass%)	Depth of indentation (estimate)
SCr435 carbonitriding material	1.14	29.6	27.2	0.1	1.15
Ordinary tempered material	0.52	9.0	14.1	0.0	0.45
180°C-0.1mass%N	0.63	20.1	12.7	0.1	0.67
180°C-0.4mass%N	0.85	29.6	12.3	0.4	0.88
210°C-0.4mass%N	0.79	21.9	12.3	0.4	0.71
240°C-0.4mass%N	0.31	7.6	12.3	0.4	0.39

diameter was pressed to the test pieces made of SUJ2 ordinary quenching material, SUJ2 carbonitriding material and SCr435 carbonitriding material with the load of $P_{\text{max}}=5$ GPa and the depth of the indentations were measured. **Table 8** shows the depth of the indentations and properties of various materials. Based on these results, we conducted multiple regression analysis with the depth of indentation as the dependent variable and the retained austenite amount, average crystal grain diameter and surface nitrogen concentration as the independent variables. Since the surface nitrogen concentration shows very little influence to the depth of indentation, it was excluded from the independent variables for multiple regression analysis. Equation (2) is the estimation equation for the depth of indentation calculated from the multiple regression analysis and **Fig. 10** shows the relation between the actually measured value and the estimated value of the depth of indentation.

$$\begin{aligned} \text{Depth of indentation } (\mu\text{m}) \\ = -0.005 + 0.022 \times \text{retained austenite amount (vol\%)} \\ + 0.018 \times \text{average crystal grain diameter } (\mu\text{m}) \dots \dots (2) \end{aligned}$$

**Fig. 10** Measured and estimated values of depth of indentation

The coefficient of determination doubly adjusted for the degrees of freedom R^{**2} in the estimation equation is 0.92, and it was clarified that the retained austenite amount and the average crystal grain diameter contribute to the depth of indentation. The more the retained austenite amount and the larger the average crystal grain size, the larger the indentation. Therefore, material with refined crystal grains and a reduced retained austenite amount is considered to be suitable for the bearings with excessive load.

6. Summary

In this paper, we introduced results of various life tests with SUJ2 of high surface nitrogen concentration.

- 1) We conducted life tests with artificial indentations on the inner ring raceway of rolling bearings 6206 for evaluation of surface initiated flaking life. In terms of L_{50} life, the SUJ2 with high nitrogen concentration showed approximately 3.2 times longer life than the SUJ2 ordinary quenching material and approximately 1.8 times longer life than the SUJ2 conventional nitriding material.
- 2) We conducted a life test of the tapered roller bearings 30206 with high nitrogen concentration at the inner/outer rings and rolling elements, in contaminated (with hard foreign objects) lubrication. In terms of L_{50} life, the SUJ2 with high nitrogen concentration showed approx. 2.1 times longer life than the SUJ2 ordinary quenching material and approx. 1.4 times longer life than the SCr435 carbonitriding material
- 3) As a result of the clean lubrication test of the SUJ2 high nitrogen concentration material in the tapered roller bearings 30206, none of the test pieces experienced flaking over 7300 h, which, according to the statistical calculation, indicates more than 15 times the calculated life with 90% reliability.
- 4) Regarding impact loads on the rolling bearings, we evaluated the likelihood of indentation by the contact between the rolling elements and rotating

rings. The result showed that the SUJ2 material with high nitrogen concentration is less likely to be indented compared to the SCr435 carbonitriding material, which is the current long-life material. Increasing tempering temperature of the SUJ2 material with high nitrogen concentration further improves this effect.

References

- 1) A. P. Voskamp : MICROSTRUCTURAL CHANGES DURING ROLLING CONTACT FATIGUE ,CHAPTER 3 (1996) 15.
- 2) Hyojiro Kurabe, Toru Araki: Tetsu to Hagane, vol. 53 (1967) 1305.
- 3) R. C. Dommarco, K. J. Kozaczek, P. C. Bstias, G. T. Hahn, C. A. Rubin: Wear, 257 (2004) 1081.
- 4) Kikuo Maeda: Industrial Heating, vol. 38 (2001) 2.
- 5) C.Ohki : SAE Technical Paper Series (2004) 2004-01-0634.
- 6) Chikara Ohki: Tetsu to Hagane, vol. 95 (2009) 695.
- 7) Shigeo Shimizu: Kikaikei no tameno shinraisei sekkei nyumon, Surikogakusha, Tokyo, (2006) 34.
- 8) Reliability Engineering Association of Japan: Reliability Handbook (1997) 209.
- 9) G. Lundberg, A. Palmgren : IVA Handlinger,(1952) 210.

Photo of authors



Daisuke SATO
Advanced Technology
R&D Center



Chikara OHKI
Advanced Technology
R&D Center

Effect of Naturally Derived Antioxidants as Surface Treatment

Yosuke TAGUCHI*
Eriko ITAHASHI*
Hidenobu MIKAMI*



Surface treatment is one of the techniques of improving the tribology characteristic and corrosion resistance. For example, dry processings such as DLC and wet processings such as plating and black oxide have been used to machine parts. However, since some wet processings contain an environmental pollutant in waste fluid, an environment-friendly surface treatment

is desired. In this paper, we introduce improvement of friction characteristic and bearing endurance by a surface treatment which used "natural derived antioxidants" as processing agent.

1. Introduction

Recently, many fields require efforts to reduce environmental impact. Surface treatments, such as plating and chemical treatment, have been traditionally used for superior tribology characteristics and corrosion resistance. However, these types of surface treatments may discharge regulated substances in the waste water.

Therefore, research and focus is on environmentally friendly surface treatments using plant-derived, natural antioxidants. As an example tannic acid, which is contained in persimmon, etc. is known to produce a thin film coating on steel surfaces ^{1), 2), 3)}. However, tribological characteristics of this type of surface treatment have hardly been evaluated.

In this report, the impact of surface treatment is evaluated, using chlorogenic acid, the plant-derived natural antioxidant contained in coffee beans, etc. in relation to various bearing performance characteristics such as friction and high temperature. In addition, the surface of the chlorogenic acid film was analyzed and the chemical structure and composition are investigated.

2. Natural antioxidant

Natural antioxidant is a collective term for the compounds (polyphenol) containing multiple phenolic hydroxyl (hydroxyl bound with aromatic rings such as a benzene ring and a naphthalene ring) in the molecule, and botanical component such as carotenoids with C₄₀H₅₆, in the basic structure. Natural antioxidants are abundant in green and yellow vegetables. Fig. 1 shows the classification of natural antioxidants. Curcumine, quercetin, isoflavone, chlorogenic acid, carotene and astaxanthin are well known to be effective as antioxidants when introduced into human bodies ⁴⁾.

In this article, chlorogenic acid was chosen as a treatment agent which is both soluble in water and exhibits relatively fast reaction with steel. Chlorogenic acid is a compound contained in coffee beans (5-10%) and has a structure made by dehydration condensation of quinic acid and coffee acid, a structural formula of which is shown in Table 1.

*Advanced Technology R&D Center

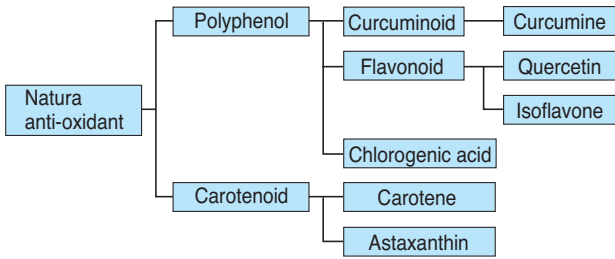


Fig. 1 Classification of naturally derived antioxidants

Table 1 Structural formula of surface treatment

Name	Structural formula
Chlorogenic acid	
Quinic acid	
Coffee acid	

3. Treatment method

Fig. 2 shows the chlorogenic acid treatment schematic. The SUJ2 plate and steel strip used for deep groove ball bearing rings and cages were cleaned with alkali and acid, immersed in the 0.5 wt % solution of chlorogenic acid, and stirred under room temperature for a predetermined time.

Fig. 3 shows the appearance of the SUJ2 plate after the chlorogenic acid treatment.

The color of the SUJ2 plate becomes darker the longer the treatment time, indicating that a film on the steel surface is produced.

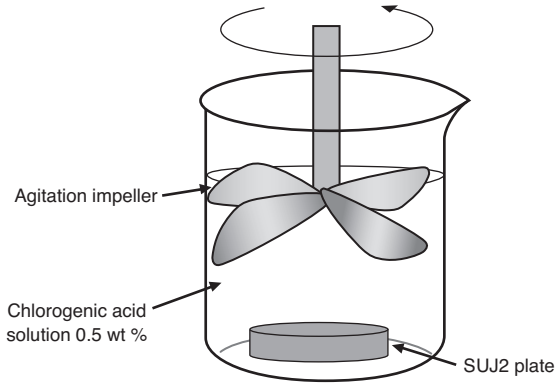


Fig. 2 Schematic view of chlorogenic acid treatment

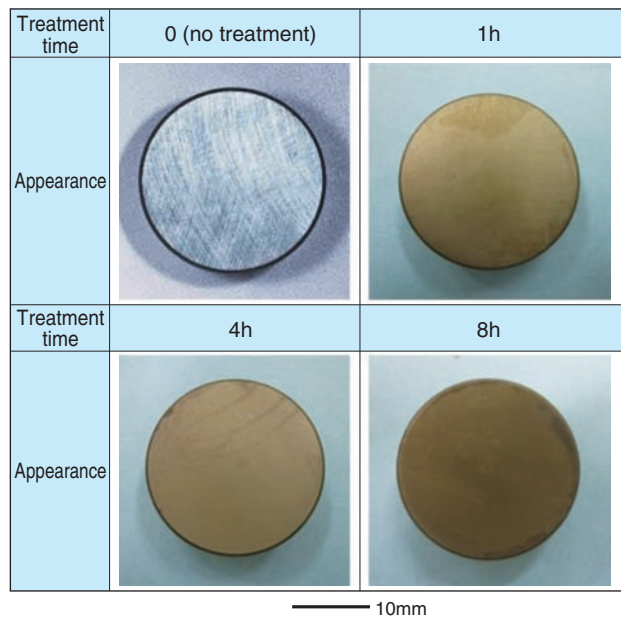


Fig. 3 Chlorogenic acid treated SUJ2 plate

4. Evaluation of various performance properties

Friction characteristics, high temperature durability of greased bearings and corrosion resistance of the SUJ2 material treated with chlorogenic acid were evaluated.

4.1 Friction property

Friction coefficient of SUJ2 plates with no treatment and with 1, 4 and 8 hours of chlorogenic acid treatment and 11/16 inch SUJ2 steel ball with no treatment was measured using a ball-on-disk type linear wear friction tester. **Fig. 4** shows the schematic overview of the test and **Table 2** shows the test conditions.

Li soap/ester grease was used as the lubricant.

Fig. 5 shows the results of the friction coefficient measurement. At the beginning of the test the friction coefficient of the chlorogenic acid treated plate was the same as that of the plate without treatment; however, it started decreasing soon thereafter with a final value 0.02 lower than the plate with no treatment. It is also noted that the chlorogenic acid treated plate showed a lower friction coefficient than the plate with no treatment regardless of the treatment time.

The results showed no difference in wear amount between the untreated sample and that with the chlorogenic acid treatment.

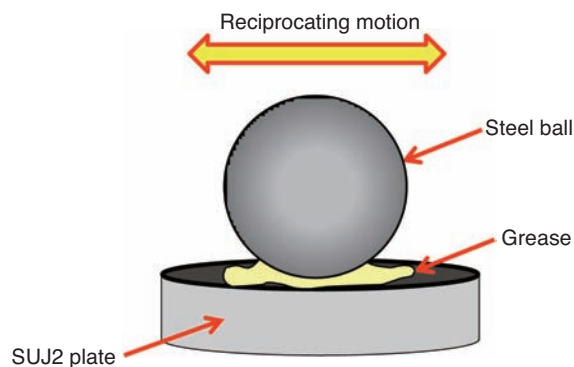


Fig. 4 Principal part schematic view of reciprocation test

Table 2 Reciprocation test condition

Plate test piece	SUJ2 ($\phi 24, t=8$)
Plate surface roughness Ra	0.02 ~ 0.05
Opposite material	11/16 inch SUJ2 steel ball
Grease	Li soap/ester grease
Frequency	10 Hz
Temperature	40 °C
Amplitude	1.2 mm
Load	15 N
Maximum contact pressure	0.8 GPa
Test time	30 min

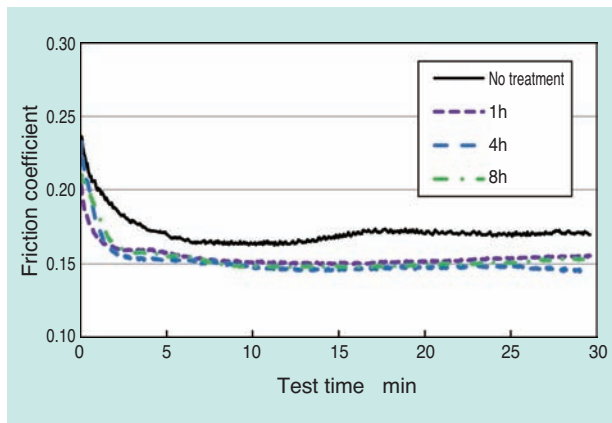


Fig. 5 Chronological change of friction coefficient

4.2 High temperature durability of greased bearings

Using a tester complying with ASTM D 3336, greased deep groove ball bearings incorporating steel cages treated with chlorogenic acid were evaluated for durability.

Steel cages with no treatment, 1-hour treatment and 4-hour treatment with chlorogenic acid were incorporated into the 6204 ZZ bearings (ID 20 mm x OD 47 mm x Width 17 mm) with a dimension stabilization process. Fig. 6 shows the overview of the test equipment and Table 3 shows the test conditions.

The test was conducted three times for each treated cage and average lives of $n=3$ were evaluated.

Fig. 7 shows an appearance of steel cage treated with chlorogenic acid and Table 4 shows scanning electron microscope (SEM) photos and arithmetic average roughness (Ra) of the chlorogenic acid treated cage surface. As shown, the roughness of the cage surface increased as the treatment time increased.

Fig. 8 shows the results of the high temperature durability test. The bearing using the 1-hour cage treatment did not show any increase in life relative to the standard part. The bearing using the cage treated for 4 hours showed more than twice the life of the bearing with no cage treatment.

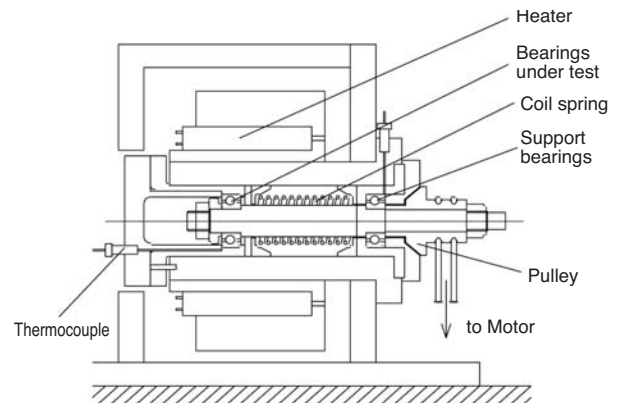


Fig. 6 High temperature bearing durability tester

Table 3 High temperature bearing durability test condition

Bearings	Deep groove ball bearings 6204ZZ ID 20 mm x OD 47 mm x Width 17 mm
Sealed grease	Li soap/ester grease
Amount of sealed grease	0.71 g
Temperature of bearings	150 °C
Rotational speed	10,000 min ⁻¹
Radial load	67N
Axial load	67N



Fig. 7 Cage after 4 hours of chlorogenic acid treatment

Table 4 SEM images of steel retainer surfaces

Treatment time, h	Ra, μm	SEM images
0 (no treatment)	0.15	
1	0.15	
4	0.26	

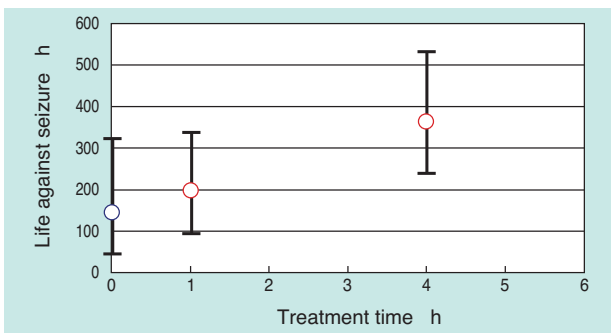


Fig. 8 High temperature bearing durability test result

4.3 Corrosion resistance

Corrosion resistance was tested under high humidity conditions compliant to JIS K 2246. Fig. 9 shows the schematic overview of the test and Table 5 shows the test conditions. SPCC material of $80 \times 60 \times 1.2$ mm of size, treated with chlorogenic acid for 4 hours was used as the test sample. For comparison, test pieces with no treatment and blackening process on the steel surface were also used. These test pieces were hung under the test stand in a dry condition without oil or grease such as rust-preventive oil, and exposed to the temperature of 49°C and relative humidity of 95% or more. The test pieces were examined for rust every 24 hours.

Table 6 shows the results of the corrosion resistance test under high humidity conditions. The test piece with no treatment produced rust within the first 24 hours. After one month, little rust was observed on the test piece treated with chlorogenic acid; however, after 2 months rust appeared. The test piece with blackening treatment did not produce rust even after 3 months. It was found that, although inferior to the blackening process, the chlorogenic acid film is effective against corrosion.

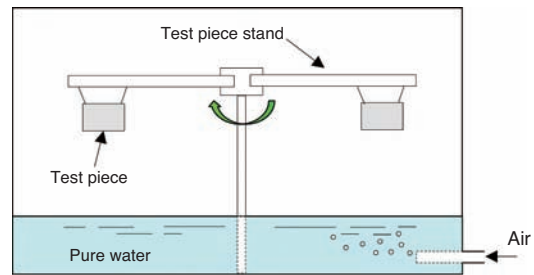


Fig. 9 Schematic view of high humidity corrosion test

Table 5 High humidity corrosion test condition

Item	Test condition
(1) Rotation speed of test piece stand	0.33mm^{-1}
(2) Temperature of test piece position	$49 \pm 1^\circ\text{C}$
(3) Relative humidity	95% or more
(4) Air flow	Three times of the tank capacity/h
(5) Temperature of water tank	Adjusted to conform to the conditions (2) and (3)
(6) Water	Pure water

Table 6 High humidity corrosion test result

Test time	Surface treatment		
	No treatment	Blackening	Chlorogenic acid treatment
24h	×	○	○
1 month	×	○	○
2 months	×	○	△
3 months	×	○	×

○ : Not rusted △ : Partially rusted × : Fully rusted

5. Surface analysis

The chlorogenic acid film exhibited friction reduction effect, extended life against grease seizure and corrosion resistance. In order to find the reasons for these effects, surface analysis of the film on the treated SUJ2 plate was performed.

5.1 XPS analysis

The chlorogenic acid treated surface was examined for the chemical composition and structure using X-ray photoelectron spectroscopy (XPS).

5.1.1 Qualitative analysis (survey analysis)

Fig. 10 shows the chemical composition of the surface of the SUJ2 plate treated for 4 hours. C, O and Fe were detected on the film surface.

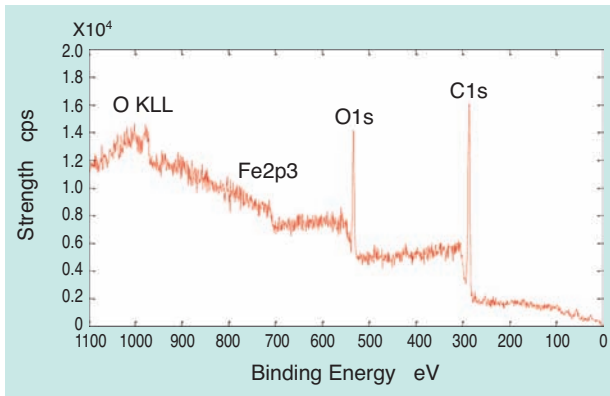


Fig. 10 XPS spectrum of film surface

5.1.2 Depth and composition analysis

Fig. 11 to **13** show the narrow spectra of C, O and Fe on the surface of the 4-hour treated SUJ2 plate. The sputter-etching times indicated in the figures are 0, 5, 10 and 15 min. and the etching speed is equivalent to the SiO₂ standard test piece's 30 nm/min.

The C1s spectrum showed a change of peak positions; C-O and C-C bonding were most prevalent on the upper most surface which transitioned to C-Fe bonding as the depth increased (**Fig. 11**). The O1s and Fe2p3 spectra revealed that Fe on the upper most surface was Fe₂O₃, and that while the depth increased, C-Fe and Fe also increased (**Fig. 12, 13**).

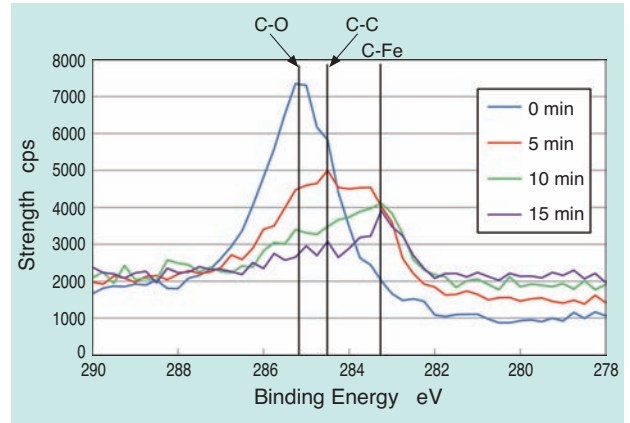


Fig. 11 C1s spectrum of chlorogenic acid film

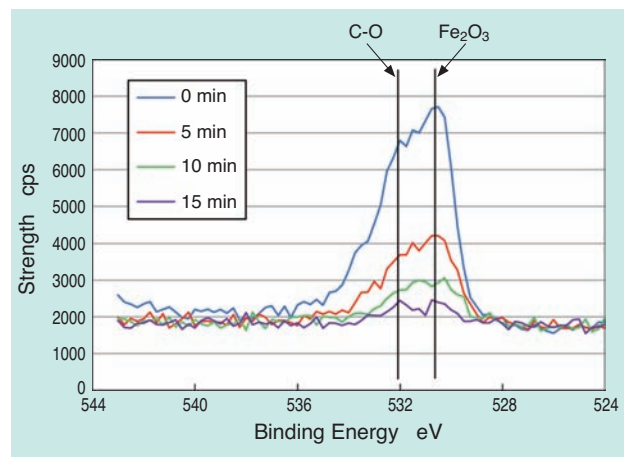


Fig. 12 O1s spectrum of chlorogenic acid film

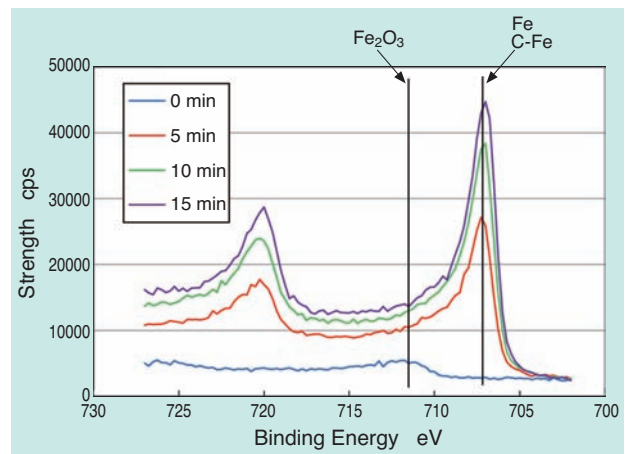


Fig. 13 Fe2p3 spectrum of chlorogenic acid film

Fig. 14 shows the composition ratio on the surface of the SUJ2 plate treated for 4 hours. C was most prevalent on the upper most surface while little Fe was observed. As the depth increased, the ratio of C decreased while Fe increased.

Fig. 15 shows C concentration is dependent on the treatment times. C was only detected on the upper most surface of the plates with no treatment and 1 hour of treatment; however, C was detected even after about 25-30 minutes of sputtering on the plates treated for 4 or more hours. After about 25-30 minutes of sputtering with this XPS equipment, the etching depth is about 0.7-0.9 μm .

The XPS analysis revealed that the chlorogenic acid film consists of C, O and Fe and is about 0.7-0.9 μm thick. The uppermost layer consists of a C-rich compound including C-O and C-C, as well as a small amount of Fe_2O_3 . As the depth increases, C and O decrease and Fe increases. Fe_2O_3 found on the surface layer decreases and compound with C-Fe bonding increases.

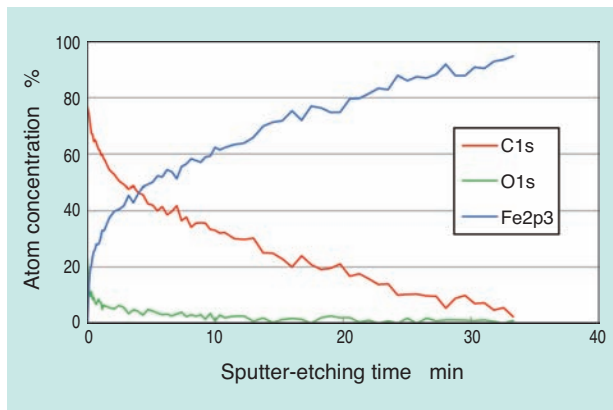


Fig. 14 Compositional ratio of a chlorogenic acid film

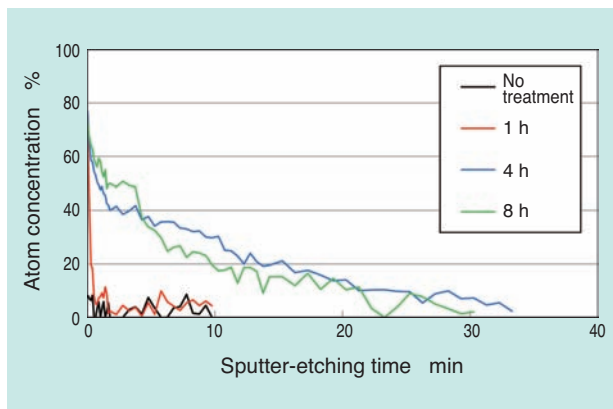


Fig. 15 Effect of chlorogenic acid treatment time

5.2 TOF-SIMS analysis

As the XPS analysis results show that the surface layer of the chlorogenic acid film is an organic substance including C-O and C-C bonding, TOF-SIMS (time of flight secondary ion mass spectrometer) analysis was conducted.

Fig. 16 shows the chlorogenic acid agent mass spectrum.

From the main peak ($m/z=353$), chlorogenic acid ions ($\text{C}_{16}\text{H}_{17}\text{O}_9^-$) were detected.

Fig. 17 shows the mass spectrum of the SUJ2 plate treated for four hours with chlorogenic acid. Chlorogenic acid ions ($\text{C}_{16}\text{H}_{17}\text{O}_9^-$) equivalent to $m/z=353$ were not detected from **Fig. 17 (a)**. However, as shown in **Fig. 17 (b)** and **(c)**, fragment ions similar to quinic acid ($\text{C}_7\text{H}_9\text{O}_4\text{Fe}^-$) and coffee acid ($\text{C}_9\text{H}_7\text{O}_5\text{Fe}^-$) were detected.

Therefore, the upper surface of chlorogenic acid film is partly formed by quinic acid and coffee acid which are decomposed from chlorogenic acid.

While finding the mechanism of reduced friction remains, it is assumed that the low friction is the result of the "conformability effect" of the formation of C-rich soft film including quinic acid and coffee acid which are decomposed after the chlorogenic acid treatment.

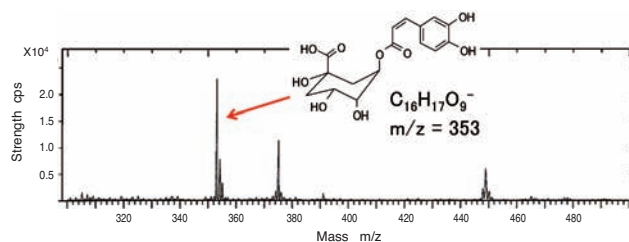


Fig. 16 Mass spectrum of a chlorogenic acid agent

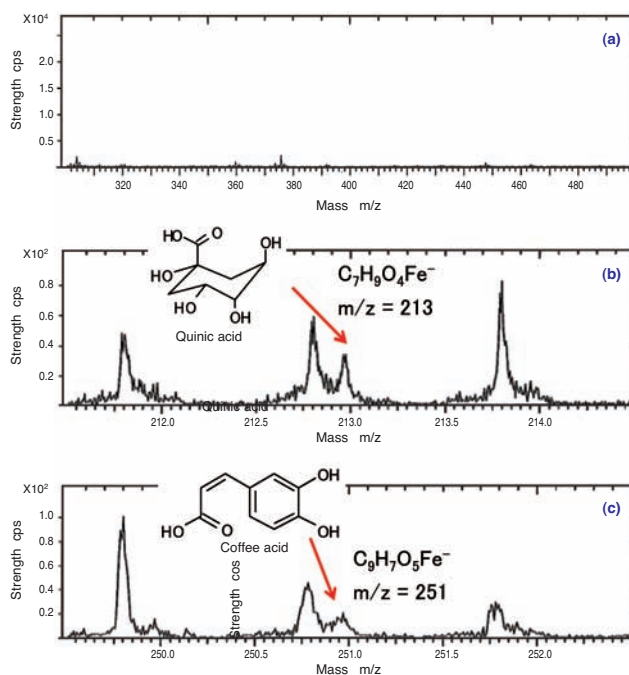


Fig. 17 Mass spectra of chlorogenic acid treated SUJ2 plate

6. Summary

It was found that by applying chlorogenic acid as the surface treatment, the frictional properties, greased bearing life and corrosion resistance are improved.

After four hours, the thickness of the chlorogenic acid film on the treated SUJ2 plate will become uniform. It was also found that the upper most surface of the film is organic and the compound of C-Fe increases as the depth increases. In addition, the presence of decomposed substances of chlorogenic acid such as quinic acid and coffee acid was found on the film surface.

In addition to the characteristics introduced in this article, the chlorogenic acid treatment is expected to be used as a high functionality treatment that saves energy and extends life. The waste water after treatment only includes chlorogenic acid, thus is environmentally friendly.

The mechanism of various characteristics that chlorogenic acid brings will be investigated in order to reduce environmental impact by applying this surface treatment for various applications.

References

- 1) Yoshiaki SHIBATA, Takayuki SHIROMOTO, Makoto YUASA, Isao SEKINE, Toshinobu IMAHAMA, Toshiharu WAKE: Corrosion Inhibition of Mild Steel by Gallic Acid in Neutral Solution, Journal of the Surface Finishing Society of Japan, 44, 4 (1993) 347
- 2) Masayoshi KATO, Takakazu KURODA, Daisuke YAMAMOTO: Kinzoku Hyomen Kogyo Zensho 13, Metal corrosion resistance technology (Maki Shoten, 1969)
- 3) Japan Society of Corrosion Engineering: Handbook of Corrosion Technologies (Boshoku Gijutsu Benran) (Nikkan Kogyo Shimbun, Ltd., 1986)
- 4) Hoyoku NISHINO, "Development of Free Radical Theory and Food Products for Ageing Prevention", CMC Technical Library, pp. 14-21 (1999)

Photo of authors (titles are at the time of development)



Yosuke TAGUCHI
Advanced Technology
R&D Center



Eriko ITAHASHI
Advanced Technology
R&D Center



Hidenobu MIKAMI
Advanced Technology
R&D Center

Grease Leakage Prevention for Double-Row Angular Ball Bearings

Mitsuo KAWAMURA*
Norihide SATO*
Tomoya SAKAGUCHI*
Mariko IZUMI**



Grease leakage from sealed bearings filled with grease makes bearing lives shortened and the peripheral parts polluted. The grease leakage generally occurs between relatively rotating inner seal grooves and seal lips. Hence, the authors had developed shape modified ribbon cages which suppress the grease transfer to the seal grooves and improved grease leakage prevention performance of ball bearings.

By adapting the approach of grease leakage prevention for ribbon cages to snap cages, grease leakage prevention performance of double-row angular ball bearings was examined. These experimental results revealed that the bearings with the modified snap cages have excellent grease leakage prevention performance. In addition, structure analyses of the cage were conducted and the modified snap cage was confirmed to be strong enough in practical use.

1. Introduction

Grease leakage from sealed and greased bearings may cause shorter overall bearing life and contaminate the surroundings. Countermeasures such as increased force of seal lip on the inner ring seal groove¹⁾ and modification of seal lip shape²⁾ have been adopted; however, these changes cause an increase in rotational torque and higher costs.

Reducing the initial grease amount is also effective for reducing grease leakage; however, because this approach shortens grease lubrication life, it is normal practice to seal as much grease as possible within the extent that the leakage does not occur³⁾.

Since the grease of bearings leaks from between the inner ring seal groove and seal lip, we devised a ribbon cage with a special shape capable of controlling the grease around the inner ring seal groove. We confirmed its effectiveness in reducing grease leakage^{4), 5)}.

Applications with outer ring rotation which frequently start and stop are the most susceptible to grease leakage^{4), 5)}. A typical application example is the use of double-row angular contact ball bearings in automobile electric auxiliary machines. When grease leaking from the bearings contacts the belt of the auxiliary machine, the belt can slip and cannot sufficiently drive the electric auxiliary machine. Because of this grease leakage must be controlled by the bearings.

The above double-row ball bearing is equipped with two snap cages inserted from either side of the bearing due to the structural limitation of the bearing with two rows of raceway grooves.

In this report, we attempted to reduce the grease leakage of double-row ball bearings by applying the grease leakage prevention technology that established with ribbon cages to snap cages.

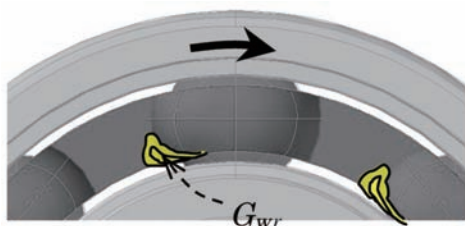
*Advanced Technology R&D Center

**CAE Dept., Automotive Business HQ

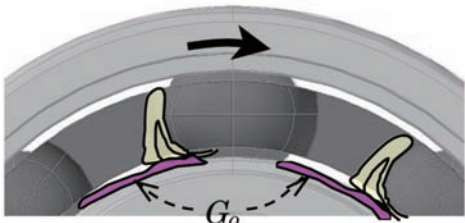
2. Grease leakage prevention technology for ribbon cages^{4), 5)}

Since grease leakage of bearings occurs between the inner seal groove and seal lip, it is necessary that grease attach on the inner ring seal groove. With outer ring rotation (the condition most susceptible to grease leakage), the movement of grease from the rolling elements to the inner ring seal groove has been observed to be as follows (Fig. 1):

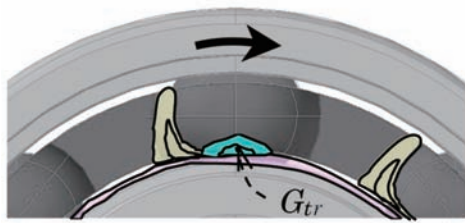
- I) The grease attached to the rolling elements is wiped off by the inner side edge of the cage pocket and attaches to the edge of the pocket as G_{wr} in Fig. 1 a).
- II) When the amount of grease G_{wr} at the edge of the pocket increases, some grease attaches to the outer surface of the inner ring as shown by G_o in Fig. 1 b).



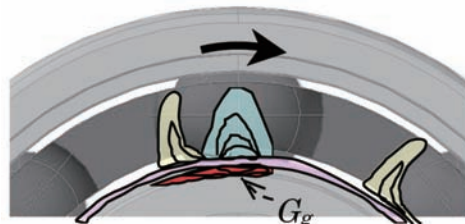
a) Wiping step



b) Grease transfer step to outer surface of inner ring



c) Grease transfer step to pocket center area



d) Grease shift step to inner seal groove

Fig. 1 Grease migration from ball surface to inner ring seal groove

- III) When the grease G_o on the outer surface of the inner ring increases, some grease attaches to the facing inner surface of the cage.

However, this location is the center of the pocket, most expanded on the axial direction, resulting in the grease attachment G_{tr} shown in Fig. 1 c).

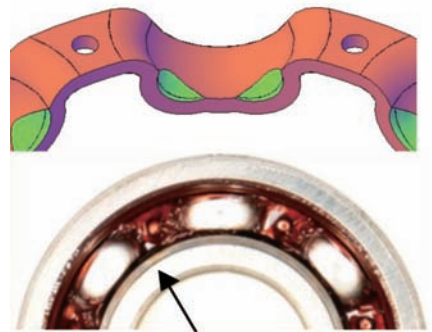
- IV) When the grease G_{tr} increases, a part of the grease is pushed up to the inner ring seal groove and is attached as shown by G_g in Fig. 1 d). When this continues, the grease is attached to the entire circumference of the inner ring seal groove.

Fig. 2 shows the standard ribbon cage and the ribbon cage with grease leakage prevention capability developed previously. It also shows how the grease is attached when the outer rings of the bearings equipped with these cages are rotated. Fig. 2 a) shows a standard ribbon cage with which a lot of grease attaches to the inner seal groove when the outer ring rotates. Fig. 2 b) shows a ribbon cage with grease leakage prevention capability where two areas of the inner surface of the pocket are recessed. With this design, grease does not attach to the inner ring seal groove, even when the outer ring rotates. We also verified that the grease leakage from the bearings is significantly reduced when operated with the seal.



Grease on inner ring seal groove

a) Conventional ribbon cage



No grease on inner ring seal groove

b) Cage of recessed pocket at diagonal positions

Fig. 2 Shape of cages and location of grease of ball bearings after outer ring rotation

3. Grease behavior with snap cages

With double-row angular contact ball bearings, the closed side of the snap cage is always oriented to face of the outboard side of the bearings, as shown in Fig. 3. Therefore, it is assumed that the grease leakage can be prevented if the grease migration from the closed side of the snap cage to the seal groove is controlled.

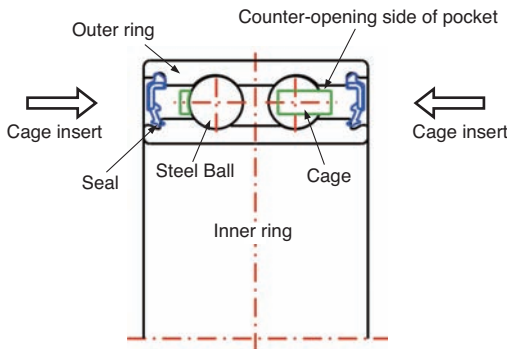


Fig. 3 Cross section view of double-row angular bearings

We examined the grease behavior of the closed side of snap cages in 6203 size deep groove ball bearings. For enhanced visibility of grease location, the grease was colored red and the cage was colored white. The grease thickener used was urea-based with worked penetration of 280. After sealing 0.5 g of grease on the raceway, the outer ring was rotated clockwise at an ultra-low speed under 7.8 N of axial pressure.

Fig. 4 shows the grease behavior at the outer ring rotational angles of 0, 180, 360, 720, 1080 and 1800 degrees. In Fig. 4 b) and c), grease is observed between the cage and the raceway ring, indicating that the grease attached to the rolling element was wiped off by the cage at the very beginning of the rotation. In Fig. 4 d), grease is observed at the edge of the closed side of the snap cage. In Fig. 4 e), grease is attached at the boundary between the outer surface of the inner ring and the seal groove and in Fig. 4 f), this grease is increased, starting to attach to the seal groove.

The attachment of grease to the seal groove mentioned above is assumed to be triggered by the attachment of grease on the edge of the closed side of the cage shown in Fig. 4 d). Therefore, the grease behavior was examined using computational fluid dynamics (CFD) analysis in order to verify the behavior of grease attachment on the edge of the closed side of the cage.

In the CFD analysis, fluid with rheological properties of grease and air were placed in the space inside the

bearings. For calculating the grease interface position, the volume of fluid method, which calculates interface of mixed-phase fluids, was used. Since the bearings have periodicity and symmetry, the domain for this unsteady analysis was focused on one pocket only. The fluids were assumed to be incompressible and move with laminar flow. For simplicity, the temperature and density of fluid was set constant and a small space was necessary between the balls and raceway due to constraints in the calculation method.

Fig. 5 shows an example of the analysis on the migration of attached grease as it relates to the rotation of the bearings. The red and yellow colors both indicate the grease inside the bearings; yellow indicating the grease attached on the seal surface.

The analysis result in Fig. 5 also indicates a similar trend as Fig. 4 d). This analysis also verifies that the grease attached to the balls was wiped off by the edge of the cage pocket, accumulated on the inner surface of the cage, and after increasing over time, migrated to the edge on the closed side of the cage.

From the results of the above observation and analysis, the migration path of the grease to the inner

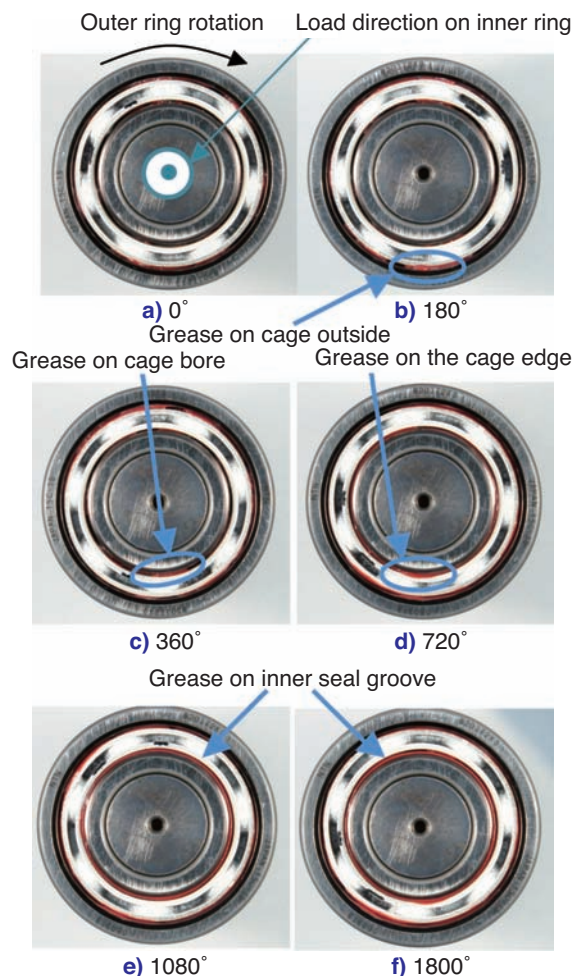


Fig. 4 Grease behavior in a deep groove ball bearing on the counter-opening side of the cage pocket

seal groove on closed side of the bearing cage was estimated as in Fig. 6.

- I) Part of the grease attached to the rolling elements is wiped off by the inner surface of the cage and accumulates as the grease G_{ws} shown in Fig. 6 a).
- II) The grease G_{ws} wiped off by the inner surface of the cage increases and attaches to the outer surface of the inner ring (grease G_o) as shown in Fig. 6 b).

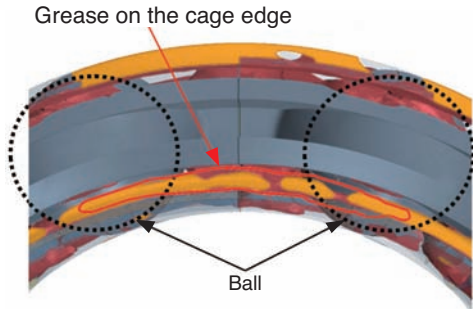


Fig. 5 Result of numerical simulation of grease behavior in deep groove ball bearings

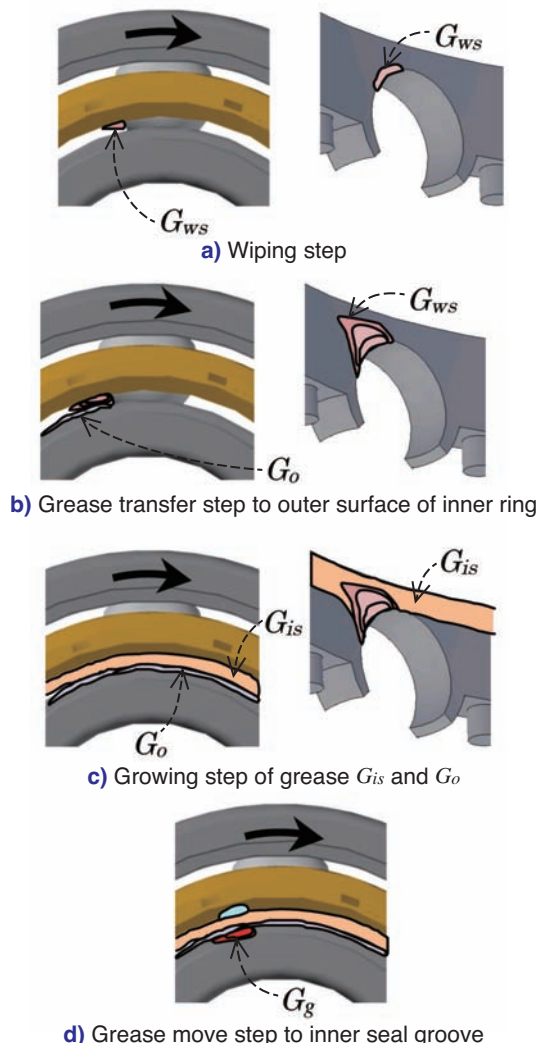


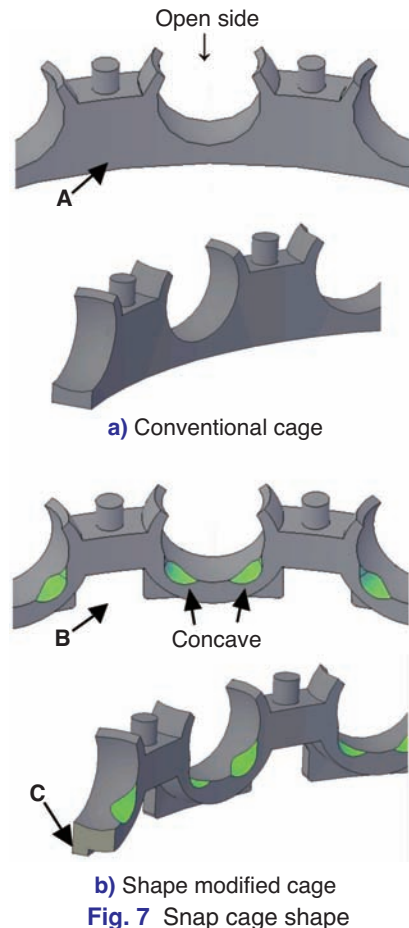
Fig. 6 Migration path of grease from ball surface to inner seal groove in ball bearings with snap cages

- III) The above processes I) and II) repeat along with the rotation, and the grease attaches to the entire circumference of the inner surface of the cage and outer surface of the inner ring as the grease G_{is} and G_o in Fig. 6 c).
- IV) Furthermore, by the increase of the grease G_{ws} and the grease pushed out to the axial direction between the raceway and balls, the grease G_{is} and G_o are pushed out and attach to the seal groove as the grease G_g shown in Fig. 6 d). Since the cage and the inner ring rotate relatively, the grease G_g spreads out on the entire circumference.

When the axial load was applied on the opposite direction, there was no significant change in the grease behavior; attachment of grease was observed on the seal groove of the inner ring.

4. Snap cage with grease leakage prevention capability

Compared to the standard snap cage shown in Fig. 7 a), we devised a cage with a modified shape (hereafter, “shape modified cage”) as shown in Fig. 7 b), based on the estimation of the grease migration path presented in the previous Section and the result of Section 2. We provided recessed areas, similar to



b) Shape modified cage
Fig. 7 Snap cage shape

the ribbon cage, on the inner surface of the pocket of the shape modified cage. The intention is to reduce the wipe-off effect on the inner surface of the cage. Since the grease tends to accumulate on part A of Fig. 7, it was removed as shown in part B of Fig. 7 b). Rigidity is not affected by the amount of material removed. In order to ensure the strength of the cage, an annular reinforcement was added at the bottom of the pocket where the cross sectional area is the smallest, as shown in part C of Fig. 7 b). The strength of the cage is reviewed in Section 7.

The cylinder-shape protrusions in the axial direction between the pockets are provided for a manufacturing reason, when the bearings are assembled.

5. Evaluation method for grease leakage prevention capability

In order to evaluate performance of the designed cage, we verified the effect on the grease behavior and the prevention capability against grease leakage from the bearings.

5.1 Grease behavioral test

In order to confirm the change of the grease behavior due to the shape modification of the cage, we operated the double-row angular ball bearings under the conditions listed in Table 1 and observed how the grease attached on the inner ring seal groove.

Table 1 Conditions for confirming shape modified cage effect

Bearing type	Double-row angular bearing
Bearing size, mm	$\phi 35 \times \phi 50 \times 20$
Outer ring rotation speed, min^{-1}	1,800
Rotating time, s	10
Axial load, N	39.2

It was necessary to observe the difference in the grease behavior from the counter-opening side of the cage pocket; therefore, grease was injected from the opening side of the pocket before the operation.

To realize this, the raceway was cut in the middle of axial direction and used as the single-row angular ball bearings.

5.2 Grease leakage test

In order to quantitatively evaluate the grease leakage prevention capability in the bearings, we verified the leakage amount depending on various greased amounts. Table 2 shows the test conditions. The grease used in this test is the same as that used in Section 3.

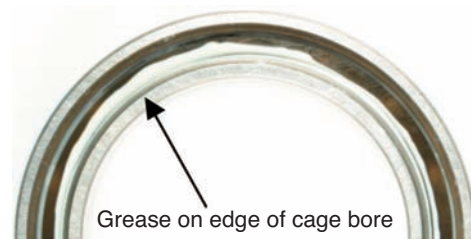
Table 2 Conditions of grease leakage test

Bearing type	Double-row angular bearing with contact rubber seals
Bearing size, mm	$\phi 35 \times \phi 50 \times 20$
Outer ring rotation speed, min^{-1}	13,500
Axial load, N	1,470
Temperature	R.T.
Test time, h	2

6. Evaluation result of grease leakage prevention property and consideration

6.1 Grease behavioral test result

Fig. 8 shows how the grease behaved after the rotation of the outer ring in the grease behavioral test. A lot of grease was observed on the closed side of the standard cage in Fig. 8 a). This is considered to be due to the large amount of the grease G_{ws} in Fig. 6, which was wiped off by the inner surface of the cage. Fig. 8 b) shows the test result when the shape modified cage was incorporated. Only a little amount of grease was attached on the inner surface of the cage, and no grease was found on the closed side of the cage pocket, outer surface of the inner ring, or seal groove.



a) Double-row angular bearing with conventional cage



b) Double-row angular bearing with shape modified cage

Fig. 8 Location of grease after outer ring rotation

6.2 Grease leakage test result

Fig. 9 shows the relationship between the grease ratio and the reduction of mass from the grease leakage test. The solid (filled-in) plots in the figure indicate the bearings which grease leakage was visually observed after the test. The grease ratio is the ratio of grease volume to the space capacity where grease can remain static even when the balls and the

cage rotate in the bearings. When this ratio exceeds 100%, grease is constantly stirred and likely to leak.

Fig. 9 reveals that the standard cage allows grease leakage at 65% or more, while the shape modified cage retained grease up until 90% of the grease ratio.

The minimum mass reduction amount that the grease leakage could be visually detected was about 0.07 g. The limit of grease ratio that does not allow grease leakage of 0.07 g or more is 65% for the standard cage and 90% for the shape modified cage.

This example shows that the limit of the greased amount could be increased by 25% by employing the shape modified cage. *

From the results mentioned above, it is evident that the shape modified cage improves the grease leakage prevention property, as well as increases the amount of grease in the bearings without allowing leakage.

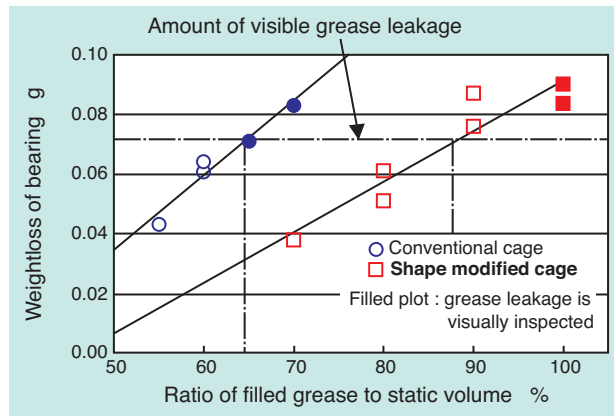


Fig. 9 Result of grease leakage test

* The space for grease to remain static is smaller for the shape modified cage compared to the standard cage because of the larger cross-sectional area at the bottom of the pocket. However, the difference of this static space volume is only 2%, the negligible level in Fig. 9.

7. Examination of cage strength

It was assumed that the magnitude of stress and displacement during operation would change due to the difference of shape between the shape modified cage and the standard cage. Therefore, we examined the strength of the cage by completing a static structure analysis using a finite element method.

The protruded edges of the pocket of the snap cage are pushed outward when the bearings rotate at high speed. This creates concern that the protruded edge and the outer ring will contact, as well as a resulting increase of contact load between the ball and the pocket. Additionally, when the bearings become misaligned, the orbital speed of the balls varies (hereafter, “orbital

speed variation of balls”) and a relatively large force is applied onto the cage^{6), 7)} by balls.

Therefore, we examined the strength of the cages against centrifugal force and orbital speed variation of balls.

7.1 Strength of cage against centrifugal force

Fig. 10 shows distribution of maximum principal stress due to centrifugal force on the standard and shape modified cages. While the maximum principal stress on the standard cage was shown at the inner

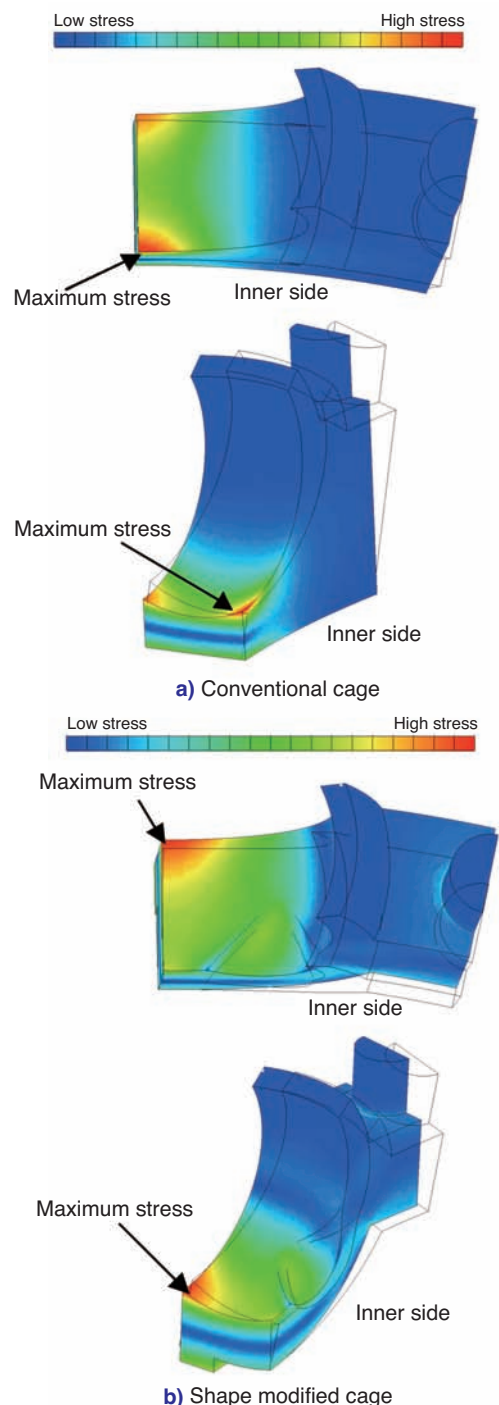


Fig. 10 Maximum principal stress of cages due to centrifugal force

surface side of the bottom of the pocket, the maximum principal stress on the shape modified cage was shown at the outer surface side. This change of the maximum principal stress point location is due to the change of the deformability of the entire cage by the addition of two recessed areas on the inner surface and removal of some material between pockets.

Fig. 11 shows the summary of main principal stress on these cages. The maximum principal stress on the shape modified cage decreased to one half compared to the standard cage. This is due to the increase of the cross-sectional area at the bottom of the pocket, in addition to the change of balance in deformability, mentioned above.

Fig. 11 also shows the maximum deformation, which reveals that the maximum deformation of the shape modified cage decreased to one half compared to the standard cage.

Since deformation of the protruded edges on the outer surface, where the maximum deformation occurs, is affected by the strength of the bottom of the pocket, we consider that the reinforcement of part C of Fig. 7 greatly contributed to this change.

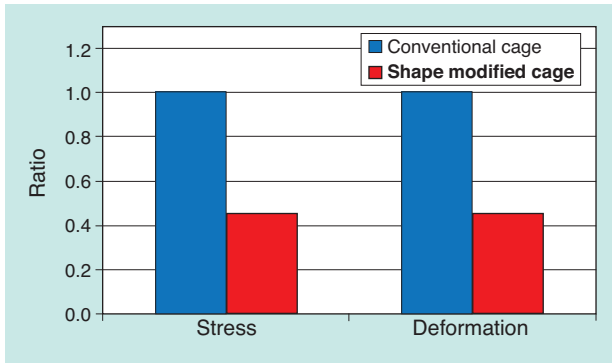


Fig. 11 Ratio of maximum stress and deformation of cages due to centrifugal force

7.2 Strength of cage against orbital speed variation of balls

Fig. 12 a) shows the operational behavior of the ball and the cage when the orbital speed of the balls varies. The balls with higher orbital speed and lower orbital speed make contact with the pocket surface, respectively, creating a strain state between both pockets. In order to analyze the stress on the cage, we applied periodically symmetrical boundary conditions on the cross sections and forced displacement equivalent to the contact load from the balls to the end pocket surfaces in the half circumference of the cage.

Fig. 13 shows distribution of the maximum principal stress generated in the cage due to the orbital speed

variation of balls. The cut section on the left is the constrained surface and the load from the ball is applied to the right side of the central pocket. As shown in Fig. 13, this force due to the orbital speed variation of the balls created the maximum principal stress at the bottom of the pocket for both cages. However, the maximum principal stress points are each different; the standard cage showed the

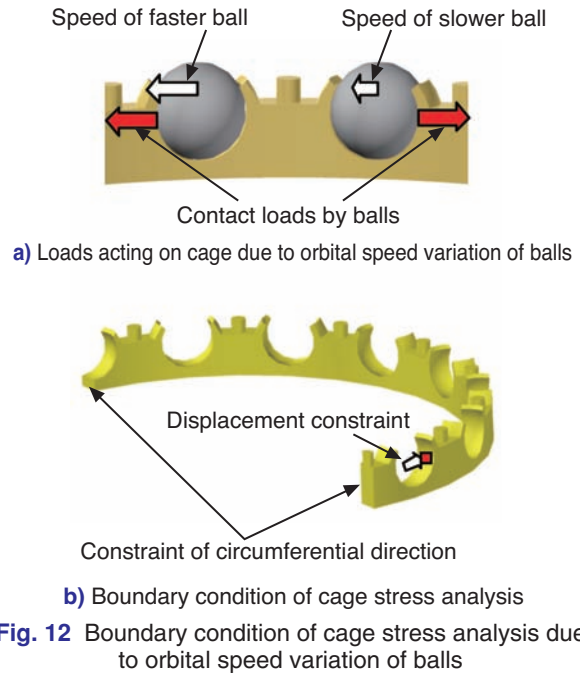


Fig. 12 Boundary condition of cage stress analysis due to orbital speed variation of balls

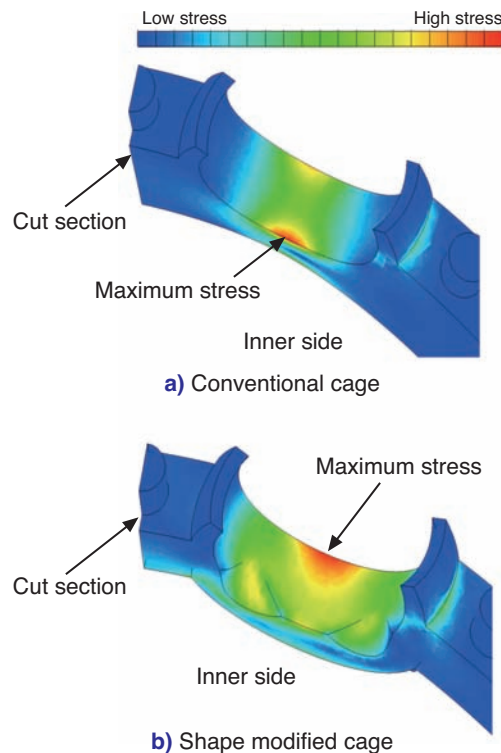


Fig. 13 Maximum principal stress of cage due to orbital speed variation of balls

maximum stress at the inner surface while the shaped modified cage showed it at the outer surface. This is due to the change in the balance of deformability. When operating bearings with large moment load, cages may break at the bottom of the pockets and the maximum principal stress was found at the same area as these breaking points.

Fig. 14 shows the ratio of the maximum principal stress. It reveals that the maximum principal stress of the shape modified cage decreased by 28% compared to the standard cage.

From these analyses, the stress generated in the shape modified cage is lower than that in the standard cage, even when centrifugal force under high rotation or force from the balls due to orbital speed variation is applied. The shape modified cage possesses sufficient unit strength in practical applications.

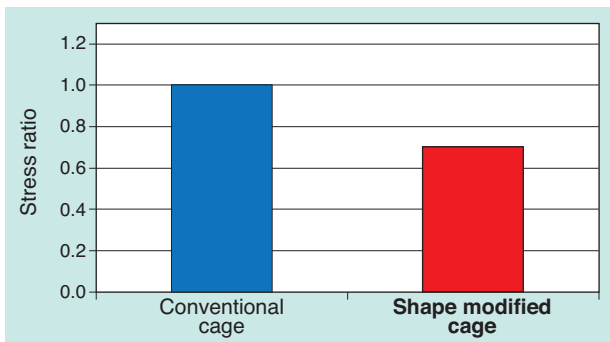


Fig. 14 Ratio of maximum principal stress of cage due to orbital speed variation of balls

8. Summary

We applied the cage design method developed for ribbon cages to the snap cages for double-row ball bearings and evaluated grease leakage prevention properties. Additionally, we analyzed the stress on the cage due to centrifugal force from high speed rotation and due to orbital speed variation of the balls caused by misaligned bearings using the finite element analysis techniques. Both the strength of the shape modified cage and the standard cage were analyzed

with this technique. The following are the results:

- 1) The observation of grease behavior revealed that the shape modified cage can reduce the grease amount attached to the inner surface of the cage and as a result, reduce the grease migration into the inner ring seal groove of double-row ball bearings.
- 2) The double-row ball bearings with the shape modified cages did not produce grease leakage even when the grease ratio over static space volume of bearings was 90%. On the other hand, the standard cage produced leakage with 65% of the grease ratio over static space volume.
- 3) The maximum principal stress generated on the shape modified cage due to centrifugal force decreased to one half that of the standard cage. The deformation of the protruded edge from the stress also decreased to half. The maximum principal stress of the shape modified cage produced by the orbital speed variation of the balls was 28% lower than that of the standard cage. Because of this, we believe that the shape modified cages have sufficient strength for practical applications.

References

- 1) Nozaki, Okasaka, Kubota, Akabe: Trends in Automotive Instrument and Auxiliary Bearing Technology, NTN TECHNICAL REVIEW No. 65, (1996), 65
- 2) NTN Ball Bearings/Shield and Seal Types, Catalog: CAT. No. 3015-III/J, (2000), 3
- 3) Tomobe, Uematsu: Grease Amount in Shield Bearings, Journal of Japan Society of Lubrication Engineers, 19, 4, 261, 1974
- 4) Sato, Sakaguchi: Improvement of Grease Leakage Prevention for Ball Bearings Due to Geometrical Change of Ribbon Cages, NTN TECHNICAL REVIEW, 78, 98, 2010.
- 5) Sato, Sakaguchi: Reduction of Grease Leakage Prevention for Ball Bearings Due to Geometrical Change of Cages, Tribologist, 57, 4, 281, 2012.
- 6) Kakuta: The Forces Acting on the Retainer of Ball Bearings under Radial or Thrust Load, Transactions of the Japan Society of Mechanical Engineers (Part 3), 32, 1161, 1966.
- 7) Kakuta: The Forces Acting on the Retainers of Ball Bearings under Moment Load or Misalignment, Transactions of the Japan Society of Mechanical Engineers (Part 3), 32, 1176, 1966.

Photo of authors



Mitsuo KAWAMURA
Advanced Technology
R&D Center



Norihide SATO
Advanced Technology
R&D Center



Tomoya SAKAGUCHI
Advanced Technology
R&D Center



Mariko IZUMI
CAE Dept.
Automotive Business HQ

A Creep Mechanism of Rolling Bearings

Tsuyoshi NIWA*



The mechanism of creep phenomena, in which a bearing ring gradually moves circumferentially to the stationary shaft or housing mating with the ring, has not been clarified yet. The author found a “surface traveling-wave creep” mechanism based on a numerical analysis and theoretical consideration. The creep is featured by movement in the same direction as the bearing rotation. In addition to the creep mechanism, this paper proposes a design requirement to prevent the creep.

1. Introduction

1.1 Creep in the opposite direction of rotation

Soda ¹⁾ describes two mechanisms regarding the creep phenomenon of the bearing ring in the opposite direction of rotation.

One of them is relatively well known and is caused by clearance between the ring and the housing or shaft, as shown in Fig. 1. Namely, when the rotational load acts on the bearings, the ring rotates on the fitting surface of the housing based on the change of the load direction. If the clearance between the fitting surface and ring is c , the ring delays by πc per rotation of the bearing, causing creep in the opposite direction from the rotation of the bearing.

The other one is caused by elastic deformation and slippage of the ring when there is no clearance. While Imai ²⁾ also proved presence of this mechanism

experimentally, Soda, by pointing out an example of a canister with a rubber band around it, as shown in Fig. 2, explained that creep occurs “because a small slippage between the rubber band and the tea canister at a certain point below the load accumulates moving forward as the canister rolls on.” At the beginning, the rubber band deforms by the load of the tea canister and stretches out in the circumferential direction. This deformation is symmetrical and the slippage is also identical between the right and left sides, therefore creep, which is a movement to one direction, should not occur. However, when the tea canister rolls, the deformation caused by the previous slippage still remains, causing asymmetry. Creep is then produced as the slippage to one direction increases. The rubber band creeps to the opposite direction from the rolling direction of the canister.

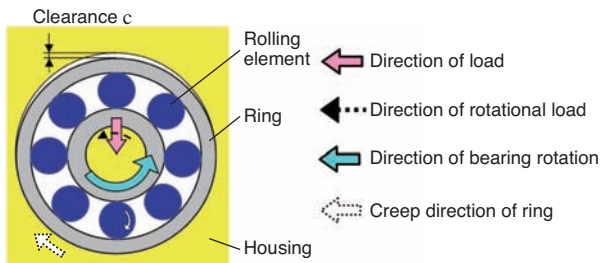


Fig. 1 Creep by clearance

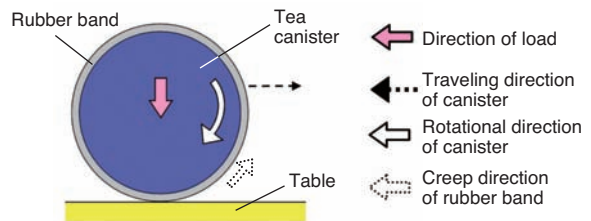


Fig. 2 Creep by rubber band slippage

*CAE Dept., Automotive Business HQ

1.2 Creep in the same direction as rotation

On the other hand, actual bearings often creep in the same direction as rotation. This phenomenon can be explained by indicating the mechanism for the ring to creep in the same direction as the traveling direction of the rolling elements.

Ten et. al.³⁾ explains that “We consider that force to rotate the outer ring on the circumference was produced from the strain that occurred every time the rolling elements traversed, which pushed the outer ring forward, little by little, generating creep.” Fig. 3 shows the schematic diagram.

This mechanism, explaining that creep comes from the accumulated strain moving forward on the circumference, matches with the explanation of Soda and can be considered to reflect the actual phenomenon. However, while Sakajiri et al.⁴⁾ pointed out some interesting remarks on the wavy deformation of the outer ring surface, the explanation of Ten et al. does not give mention to this finding and therefore, does not give a clear picture of the phenomenon.

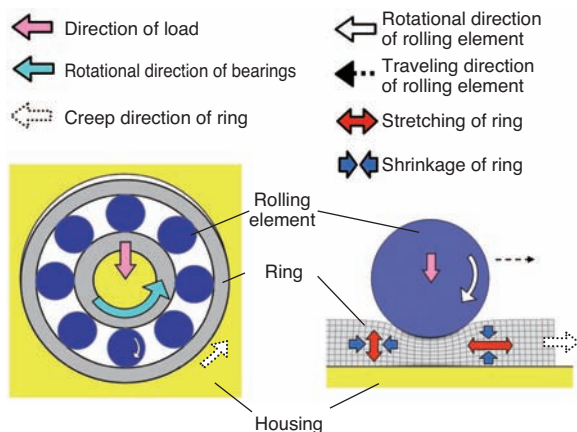


Fig. 3 Creep by strain

1.3 Proposal from our study

In this study, we provided a hypothesis that the traveling wave is produced on the ring surface and this traveling wave moves the ring and produces creep. Using an FE analysis, creep can be produced relatively easily. However, there is currently no literature pointing out that creep is a transfer phenomenon by traveling waves. This may be caused by the fact that this phenomenon is unique and the explanation of the behavior itself is difficult. Therefore, we will start explaining this mechanism using familiar devices. Then, we will also discuss conditions to restrict creep from the principles of generating traveling waves.

2. Mechanism of traveling wave type creep

2.1 Transfer of ultrasonic motor

We look at the operation of an ultrasonic motor. In a disk-type ultrasonic motor, traveling waves are excited by piezoelectric elements on the surface of an elastic body. This produces an elliptic motion on the rotor in the opposite direction of the traveling waves on the surface of the elastic body⁵⁾.

Fig. 4 shows the transfer mechanism of the ultrasonic motor. The rotor, pressed on the elastic body, moves in the opposite direction from the traveling waves by the elliptic motion of the surface.

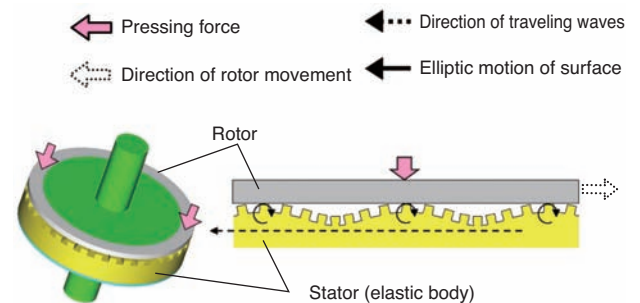


Fig. 4 Mechanism of ultrasonic motor

2.2 Self-transfer of ring due to the traveling waves

According to Sakajiri et al.⁴⁾ the traveling waves in bearings are produced when the load from the rolling elements acts on the ring surface and the fitting surface immediately below that point is pushed out. This causes the surface to become wavy up to several microns depending on the load. When the bearings rotate, the rolling elements also move, with which these surface waves become traveling waves.

In the ultrasonic motor application, the traveling waves produced at the stator move the rotor. With the bearing ring creep, as shown in Fig. 5, traveling waves are produced to the ring itself which cause the it to creep. In terms of the direction of creep, the ring acts on the housing in the opposite direction of the

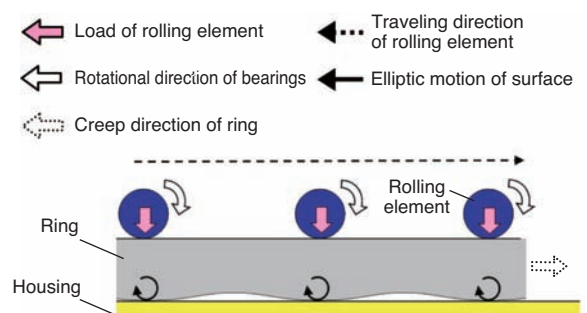


Fig. 5 Traveling-wave creep of bearing ring

traveling direction of the rolling elements. However since the housing is fixed, the ring is pushed back resulting in traveling in the same direction as the rolling elements, that is, rotating in the same direction as the rotation of the bearing.

The traveling waves produced on the ring surface behave like peristaltic motion in the circumferential and radial directions throughout the loaded area. The rotational movement opposite to the traveling waves at the fitting surface immediately below the rolling elements is characteristic of this.

In this study, this transfer phenomenon of the ring by this mechanism is called "traveling wave type creep."

3. Conditions to restrict the traveling wave type creep

Ten et al. ³⁾ pointed out that increasing the number of rolling elements for load distribution and using thicker ring are effective for reducing the local strain. However, conditions to fundamentally restrict creep are not indicated. In the following sections, we will discuss the design requirements necessary for restricting the traveling waves.

3.1 Behavior of a point within a body

As shown in Fig. 6, it is considered that a point located at a relatively shallow area of a body moves in a loop when load from traveling rolling elements is applied on the surface of the body. When a rolling element passes immediately above (1), the point is pressed down and when the point is between two rolling elements (3), it moves up closer to the surface. In between those positions (2) and (4), it moves to the opposite sides of the rolling elements. This micro behavior is repeated.

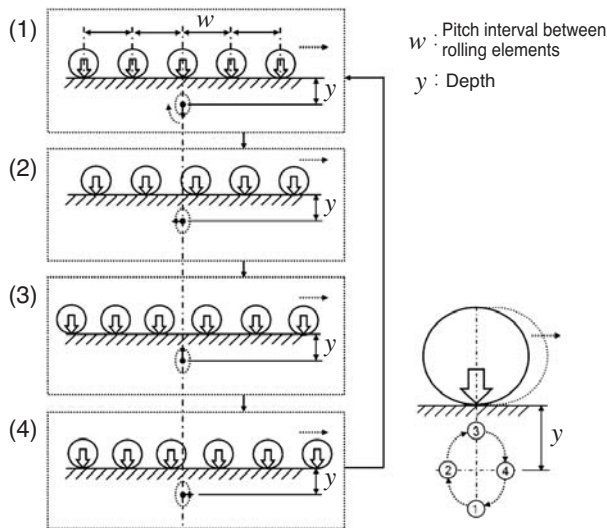


Fig. 6 Behavior of internal point under loading

3.2 Evaluation by Bussinesq equation

We examined the behavior of the point in the body using the Bussinesq's displacement equation ⁶⁾ which assumes plane strain.

Fig. 7 shows the analysis model. Following the model of Imai ²⁾, we simplified the model assuming that the load of the rolling elements q_i is distributed following the sinusoidal function. The displacement produced to the point at the depth y in the middle of the loaded area affected by the i th load is described by Equations (1) and (2). Fig. 8 shows the Lissajous figure indicating the locus of the point in the body which is displaced by the load of 5 traveling rolling elements.

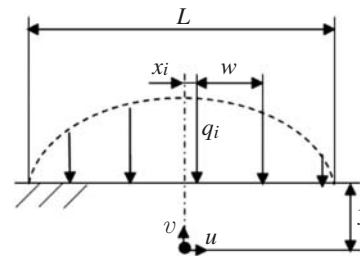


Fig. 7 Analytical model

$$u_i = \frac{q_i}{2\pi G} \left\{ \frac{x_i y}{x_i^2 + y^2} - (1 - 2\nu) \tan^{-1} \left(\frac{x_i}{y} \right) \right\} \dots\dots (1)$$

$$v_i = \frac{q_i}{2\pi G} \left\{ \frac{x_i^2}{x_i^2 + y^2} + 2(1 - \nu) \log \left(\frac{\sqrt{x_i^2 + y^2}}{B} \right) \right\} \dots\dots (2)$$

- L : Length of load zone
- q_i : Load of rolling element i
- x_i : Position of rolling element i
- u, v : Displacement
- G : Shear modulus
- ν : Poisson's ratio
- B : Integral Constant
- w : Pitch between rolling elements

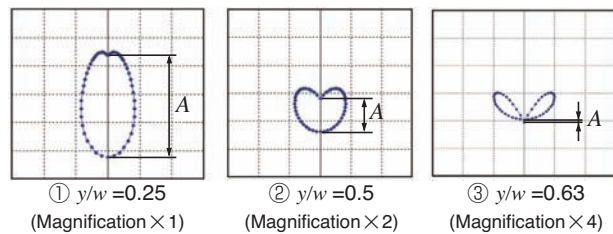


Fig. 8 Locus of internal point

From Equations (1) and (2), if the ratio of the pitch w and the depth y is constant, that is, if the conditions are homologous, the shape and size of the loop in the Lissajous figure become the same. For convenience, B of Equation (1) was set to 1, however, it does not affect the shape and size of the loop.

In this study, we considered that the movement of the elliptic motion in Fig. 6 and 8 is the source of the creep movement by traveling waves and evaluated the amplitude A of Fig. 8, as the index of the elliptic motion.

3.3 Condition to restrict the traveling wave

Fig. 9 shows the examined result of the behavior of amplitude A in Fig. 8. While the amplitude A is proportional to the sum of the rolling element load $\sum q_i$, it converges under the conditions of the ratio of depth y / pitch interval $w > 0.6$.

The ring, housing and shaft are in contact, therefore, the above discussion that assumes continuous body does not generally apply. However, if we consider the depth y as the thickness of the ring t , under the condition of Equation 3 below,

$$\text{Thickness of ring } t / \text{pitch interval of rolling elements } w > 0.6 \quad \dots\dots\dots (3)$$

the traveling waves, which is the main driving force of the transfer phenomenon, converge. Therefore, creep should be restricted and is depicted in Fig. 10.

From the above, we consider that the conditions for producing traveling wave type creep are in the ratio of the thickness of the ring and pitch interval rather than the load and size of the bearing components.

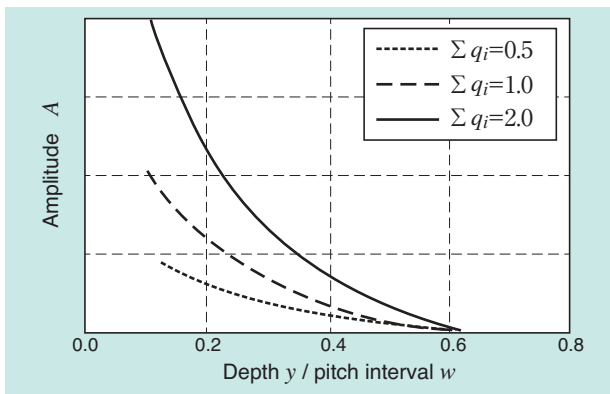


Fig. 6 Amplitude of locus

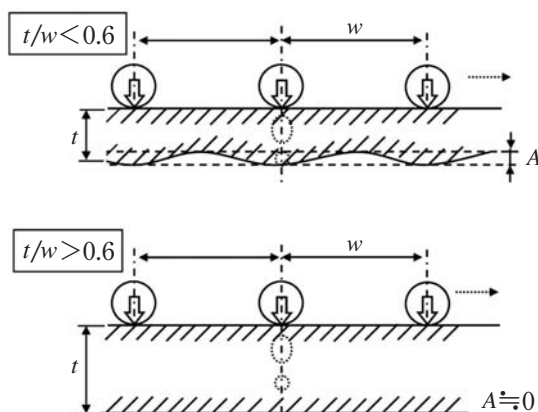


Fig. 10 Thickness of bearing ring and traveling-wave

4. Summary

- (1) We have clarified the phenomenon where the ring creeps in the same direction as the bearing rotation and presented a mechanism called "traveling wave type creep".
- (2) We have presented the mechanism to restrict the traveling wave type creep under the condition of the thickness of ring / pitch interval of rolling elements > 0.6 .

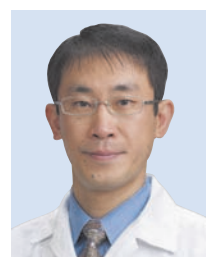
In addition, as further complex contact behavior on the fitting surface due to traveling waves is being clarified⁷⁾, we are planning to study it in details.

This article has been edited based on the original manuscript for the Proceedings of Tribology Conference⁸⁾. We thank the Japanese Society of Tribologists, who gave us the permission for publishing it.

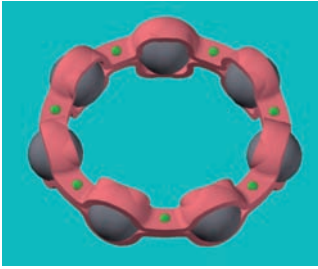
References

- 1) Soda: Bearings, Iwanami Shoten (1964), 196.
- 2) Imai: Lubrication, 4 (1959) 307.
- 3) Ten, Sakajiri, Takemura, Yukawa: NSK Technical Journal No. 680 (2006) 13.
- 4) Sakajiri, Takemura: Proceeding of Japan Tribology Conference (2003-5) 103.
- 5) Kanazawa, Tsukimoto, Maeno, Miyake: Tribologist, 38, 2 (1993) 21.
- 6) For example, Nakahara: Zairyo Rikigaku - Gekan, Yokendo (1966) 122.
- 7) Niwa: Proceedings of Japan Tribology Conference (2012-9) 141.
- 8) Niwa: Proceedings of Japan Tribology Conference (2012-5) 253.

Photo of authors



Tsuyoshi NIWA
CAE Dept.
Automotive Business HQ



“The Japanese Society of Tribologists 2012” Technology Award

Prevention of Grease Leakage from Ball Bearings Due to Cage Shape Improvement

Norihide SATO, Mitsuo KAWAMURA, Tomoya SAKAGUCHI

1. Introduction

Grease leakage in contact seal type, greased deep groove ball bearings occurs from between the inner seal groove and the seal lip which rotate relative to each other. Therefore, we considered that the grease leakage could be controlled by controlling the attachment of grease to these components. With the development of a cage with a new geometry that could control the attachment of grease to the inner ring seal groove, we succeeded in improving the grease leakage prevention properties 1), 2), 3).

This technology received the “2012 Japanese Society of Tribologists Technology Award”, which is given to excellent new technologies in tribology. In this article, an overview of this technology is introduced.

2. Behavior of grease attachment to inner ring seal groove

When the outer ring or inner ring of ball bearings rotate at low speed, grease attached to the balls is wiped off by the cage and attaches to part ① of Fig. 1. Then the grease migrates to the outer surface of the inner ring ②, in the middle of pocket ③, and inner ring groove ④.

With this technology, we developed a cage with geometry shown in Fig. 2, which can control the grease migration path mentioned above.

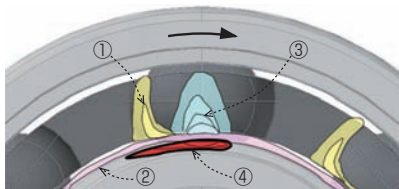


Fig. 1 Path of grease transfer to inner seal groove

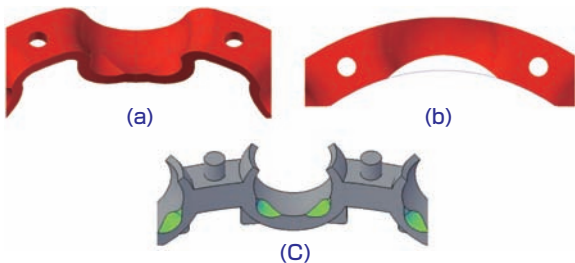


Fig. 2 Shape of developed cages

3. Evaluation result of grease leakage prevention property

As shown in Table 1, the bearings incorporating the ribbon cages of the geometry in Fig. 2 (a) and (b) significantly reduced a frequency of the grease leakage compared to the standard ribbon cages.

Furthermore, evaluation of the grease leakage with different

Table 1 Results of grease leakage test from sealed ball bearings

Cage shape	Leakages/Total
Base cage	6/15
Press cage of diagonally recessed pocket inner surfaces (Fig.2 (a))	1/15
Press cage of narrow pocket width (Fig.2 (b))	0/15

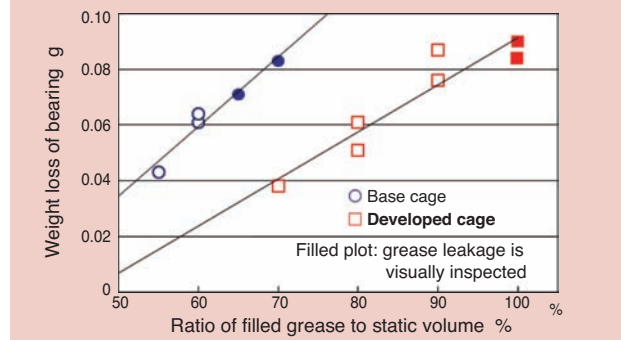


Fig. 3 Grease leakage characteristics of bearings with developed snap cage

grease amount using bearings that incorporated the snap cages shown in Fig. 2 (c) demonstrated superior grease leakage prevention property compared to the standard snap cages, as shown in Fig. 3.

4. Summary

By using bearings with this technology, it is possible to extend bearing life by increasing grease amount while reducing grease leakage. By extending life, bearings may be downsized, leading to reduced rotational torque and lighter weight. While this technology is currently adopted in automotive electrical and auxiliary equipment, we expect to expand the application to various machines and contribute to improved energy saving.

References

- Sato, Sakaguchi: Improvement of Grease Leakage Prevention for Ball Bearings Due to Geometrical Change of Ribbon Cages, NTN TECHNICAL REVIEW, 78 (2010) 91.
- Sato, Sakaguchi: Reduction of Grease Leakage Prevention for Ball Bearings Due to Geometrical Change of Cages, Tribologist, 57, 4 (2012), 281.
- Kawamura, Sato, Sakaguchi: Improvement of Grease Leakage Prevention for Double-Row Angular Ball Bearings, Proceedings of Tribology Conference, Fukui, 2010-9, (2009) 283.

Photo of authors



Norihide SATO, Mitsuo KAWAMURA, Tomoya SAKAGUCHI
Advanced Technology R&D Center



EMM2012 Mechatronics Award Grand Prix

Intelligent In-wheel Motor System

Herve LENON*, Eiichi ASANO**, Tomomi GOTOU***, Kaori TOMODA***

1. Introduction

At the “European Mechatronics Meeting (EMM) 2012” held in the Haute-Savoie Department of Eastern France from June 6 to 7, 2012, NTN’s Intelligent In-Wheel Motor System won the Grand Prix of Mechatronics Award.

EMM2012 is an international meeting in the field of mechatronics organized by Thésame, a public industrial support organization based in the Haute-Savoie Department. The meeting attracted approximately 300 participants from 20 companies both inside and outside of France, featuring exhibits and conferences of mechatronics technologies related to environmental conservation such as natural energy, EV/HEV, etc.

2. Overview of presentation

NTN participated in the meeting together with our European subsidiary NTN-SNR, which is headquartered in France, and appealed the technical alliance of Japan and France with the aim of acquiring EV-related business in the European market.

At the booth, we presented a dynamic demonstration of “In-Wheel Motor System for Electrical Commuters” and various sensor technologies.

In the special exhibit area, we exhibited a two-seater electric commuter with the “In-Wheel Motor System” installed on rear wheels and a concept car “Q’mo” with the “Four-Wheel Independent Drive/Steering System” installed. We also demonstrated “lateral move” and “pivot turn” in the demo



run of “Q’mo”, which are the unique attributes of the in-wheel motor drive, drawing the attention of many visitors.

At the international conference concurrently held, we gave a technical presentation called “Optimization of energy efficiency of EVs by applying in-wheel motor and by-wire system” to raise the presence of EV system products.

The meeting gives awards to excellent products every year and NTN’s intelligent in-wheel motor system won the highest honor of Grand Prix among the six nominated companies.

This in-wheel motor system was highly praised for the integration of innovative mechatronics technologies for controlling rotation of wheels, motor, reducer, inverter, brake and related sensors, and was unanimously elected by the judges.

3. Summary

We will promote early adoption of EV system products by presenting and supporting the latest EV technologies of the NTN group in the European market where EVs are becoming popular.



*NTN-SNR ROULEMENTS Reserch & Innovation Mechatronics

**Business Promotion Dept. EV Module Business HQ

***Drive System Engineering Dept. EV Module Business HQ



Automechanika 2012 Innovation Award

In-wheel Motor System

Herve LENON*, Eiichi ASANO**

1. Introduction

The In-Wheel Motor System developed by NTN won the Innovation Award in the parts division at "Automechanika 2012", the world's largest exhibition for the automotive aftermarket that was held in Frankfurt, Germany from September 11 to 16, 2012.

Automechanika is the world's largest exhibition for the automotive aftermarket and held every other year.

In 2012, it attracted more than 4,500 companies from 74 countries and approximately 150,000 people participated from all over the world.

2. Overview of presentation

NTN's European subsidiary, NTN-SNR exhibited at Automechanika 2012 with the theme "Innovation and R&D." It presented a large range of aftermarket products such as wheel bearings with sensors, engine timing belts, boots for auxiliary equipment, auto tensioner, water pump kit, etc., as well as the concept cars "Q'mo" and "Two-seater Electric Commuter" equipped with an in-wheel motor system.

The most outstanding technologies at the show were awarded for each division and NTN's In-Wheel Motor System won the Innovation Award in the part division.

With 13 European automobile related companies entering the award category, the In-Wheel Motor System was highly praised as being the world's lightest and most compact design consisting of the hub bearing, motor, and reducer stored within the wheel, and also for its outstanding functionality as a vehicle stability control system that provides independent control of the left and right wheels based on sensor information.

The show and the award presentation ceremony were introduced by TV, magazines, and the internet, which helped to raise the presence of the NTN group in the automotive aftermarket and EV market.

3. Summary

In-wheel motors are gaining a lot of attention as the driving system for the next generation electric vehicles with the expectation for improved safety and vehicle stability as well as reduction of greenhouse gas. We strive to expand our activities globally for the early adoption of the next generation EVs, including in the European market where EVs are increasingly gaining ground.



NTN-SNR representatives receiving the award
Ulrici, Vice President, Automotive Business HQ (2nd from left)
Gauthier, Sales Manager, Automotive Repair (Center)
Malavasi, Vice President, Automotive Repair/Logistics (2nd from right)

*NTN-SNR ROULEMENTS Reserch & Innovation Mechatronics

**Business Promotion Dept. EV Module Business HQ

The Japan Society for Precision Engineering, Spring Meeting, 2003, Best Presentation Award

Parallel Link High Speed Angle Control Equipment

Hiroshi ISOBE, Yukihiro NISHIO, Keisuke SONE, Hiroyuki YAMADA, Yoshio FUJIKAWA

1. Overview

NTN developed Parallel Link High Speed Angle Control Equipment (hereafter, high speed angle control equipment)^{1), 2), 3)} applying a special parallel link mechanism with rotational 2-degrees-of-freedom, and deployed this equipment to a grease dispensing mechanism. The key features of this equipment are high speed operation and wide range of motion.

The presentation⁴⁾ on this equipment given at the Spring Meeting, 2003 of The Japan Society for Precision Engineering received the “Best Presentation Award” for young researchers, which is selected from the perspective of the originality of the research, presentation content, Q&A, etc. In this article, an overview of this presentation is introduced.

2. About high speed angle control equipment

Fig. 1 shows the high speed angle control equipment developed for grease dispensing. This equipment determines the attitude of parallel link mechanism with 4 joints and 3 links represented by the bend angle θ and angle of traverse ϕ in Fig. 2. The attitude is uniquely determined if two among three base-side arm rotational angles β_n ($n=1,2,3$) are determined. The relational expression is shown in Eq. 1.

$$\begin{cases} \cos(\theta/2)\sin\beta_1 - \sin(\theta/2)\sin(\phi + \delta_1)\cos\beta_1 + \sin(\gamma/2)=0 \\ \cos(\theta/2)\sin\beta_2 - \sin(\theta/2)\sin(\phi + \delta_2)\cos\beta_2 + \sin(\gamma/2)=0 \\ \cos(\theta/2)\sin\beta_3 - \sin(\theta/2)\sin(\phi + \delta_3)\cos\beta_3 + \sin(\gamma/2)=0 \end{cases} \dots\dots\dots(1)$$

We have improved the repeat positioning accuracy²⁾ up to $\pm 0.03\text{mm}$ or less, by controlling all 3 links by motors and allowing slight interference of 3 base-side arms for canceling the backlash of the drive mechanism.

3. Application to grease dispensing mechanism

An example of the grease application equipment configuration using this equipment is shown in Fig. 3.

In this configuration, it moves the work in the XY plane, as well as controls the attitude of the jet dispenser (a model to discharge grease at a distance by controlling high pressure air with electromagnetic valve). With this configuration, grease can be applied from various directions with different angles, to areas previously not reachable from the top or vertical side of a column-like object. We have also achieved high speed application of approx. 0.1 s/point.

References

- 1) Keisuke Sone, Hiroshi Isobe, Koji Yamada: High Angle Active Link Equipment, NTN TECHNICAL REVIEW No. 71, 70-73, 2003
- 2) Hiroshi Isobe, Yukihiro Nishio: Parallel Link High Speed Angle Control Equipment (PHACE), NTN TECHNICAL REVIEW, No. 80, 42-47, 2012
- 3) Hiroshi Isobe: Parallel Link High Speed Angle Control Equipment – Basic Configuration and Application for Grease Dispensing, Machine and Tool, February Issue, 83-87, 2013
- 4) Hiroshi Isobe, Yukihiro Nishio, Keisuke Sone, Hiroyuki Yamada, Yoshio Fujikawa: Parallel Link High Speed Angle Control Equipment, Proceedings of the Japan Society for Precision Engineering Spring Meeting in 2013, 809-810, 2013

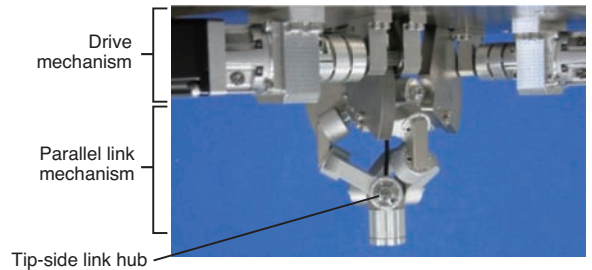


Fig.1 Parallel link high speed angle control equipment

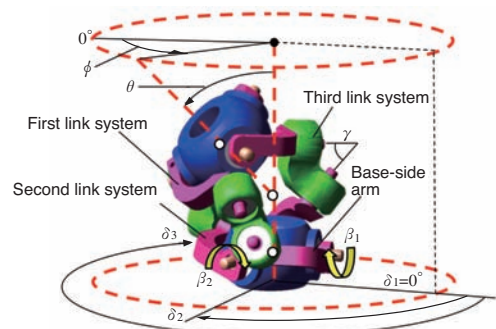


Fig.2 Parallel link mechanism

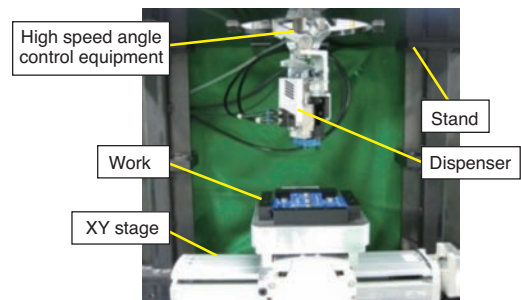


Fig.3 System configuration example of grease dispensing

Photo of author (representative)

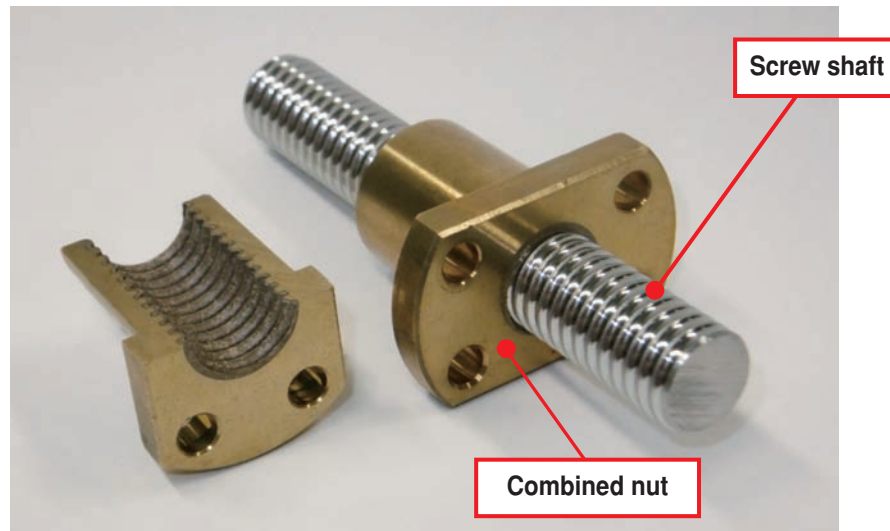


Hiroshi ISOBE

New Product Development
R&D Center

Plastic Sliding Nut and Screw with High Load Capacity

An industry first! A sliding nut and screw that integrates brass and plastic for superior **durability and wear resistance!**



Features

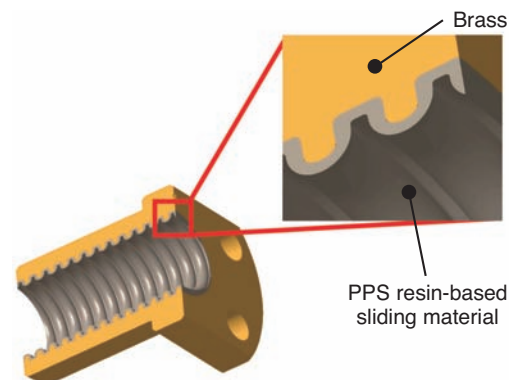
By the hybrid structure of metal and resin,

- [1] **Load resistance:**
Twice compared to that of conventional products
- [2] **Durability:**
Three times compared to that of conventional products
- [3] **Capable of being used without lubrication:**
Low noise, low heat generation

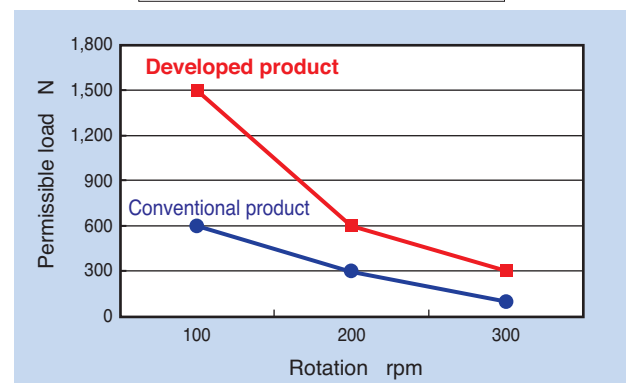
Applications

- **Clean environment**
(medical equipment/food processing equipment, etc.)

Structure



Test condition
Stroke: 180 mm
Wear after 2000 times: ≤ 0.1 mm



Multi Layer BEARPHITE

The world's first!

A double molding method to cast two dissimilar materials into a single object!!
 Oil-impregnated sintered bearings with **high strength and outstanding wear resistance.**



Features

A double molding method is used to cast two dissimilar materials into a single object to achieve both high strength and outstanding wear resistance.

[1] Radial crushing strength

Oil content: 17 vol% or more

[2] Variation in inner and outer diameter dimensional precision:

50 μm or less

Applications

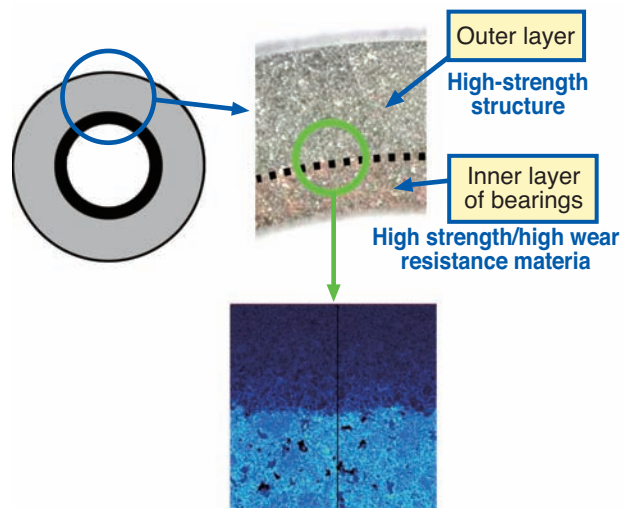
- Bearings used for joints of construction machines, etc.



○ part: applicable

Structure

- High wear resistance material is used on the inner layer of the bearings and high strength structural material is used on the outer layer:
 ⇒ achieves bearing performance and moldability
- Simultaneous molding and sintering of two dissimilar materials:
 ⇒ Strong bonding due to the interface diffusion during sintering



Sintering of solid/liquid layers

Hybrid BEARPHITE HP

An industry first! Hybrid BEARPHITE that **can be used in high PV ranges 10 times that of conventional products.**



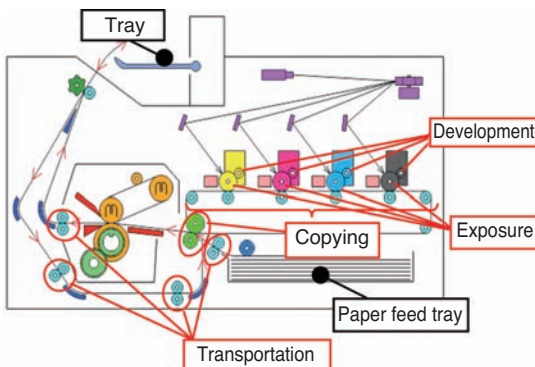
Features

By adopting ultrahigh molecular weight resin:

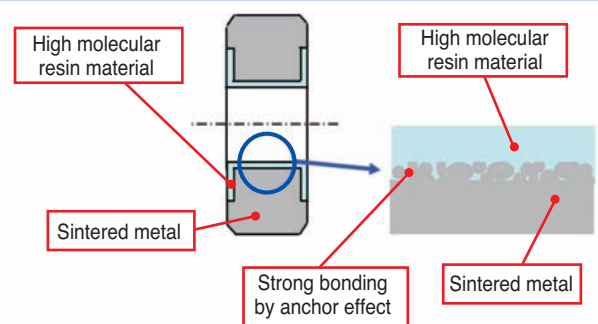
- [1] **Bearings are usable in high PV ranges**
10 times or more than that of conventional products
- [2] **Can be molded with the same dimensions as rolling bearings:**
Directly replaceable
- [3] **Low friction, high level of rotational precision, compatible with flexible shafts:**
High performance and can be used with aluminum or resin shafts

Applications

- Office equipment, photocopiers, bearings for LBP, etc.



Structure



Bearing size: $\phi 8 \times \phi 16 \times 5$
Shaft material: Bearing steel
Test temperature: Room temperature

